

Doctoral Dissertation

博士論文

Effects of Replicated N-body Simulation Boxes in Simulating Weak Lensing Observables

弱重力レンズ統計量の模擬データ生成における
有限体積のN体シミュレーションの影響の研究

A Dissertation Submitted for the Degree of Doctor of Philosophy

December 2024

令和6年12月博士（理学）申請

Department of Physics, Graduate School of Science,

The University of Tokyo

東京大学大学院理学系研究科
物理学専攻

Akira Tokiwa

常盤 晟

Contents

1	Introduction	1
1.1	Historical Overview	1
1.2	Astronomical Surveys and Observations	2
1.3	Constraint from Weak Lensing	4
1.4	Higher-Order Statistics in Weak Lensing	5
1.5	Aim of this Thesis	7
1.6	Structure of the Thesis	9
2	Foundational Concepts in Modern Cosmology	10
2.1	Einstein Field Equations	10
2.1.1	The Stress-Energy Tensor for a Perfect Fluid	11
2.1.2	Equations of State for Different Cosmic Components	11
2.2	FLRW Metric and the Friedmann Equations	13
2.2.1	The FLRW Metric	13
2.2.2	Derivation of the Friedmann Equations	13
2.2.3	Critical Density, Density Parameters, and H ₀	14
2.2.4	Evolution of Density Parameters with Scale Factor	14
2.3	Redshift and Cosmological Distances	15
2.3.1	Luminosity Distance	16
2.3.2	Angular Diameter Distance	17
2.4	Initial Conditions and the Primordial Universe	17
2.4.1	Primordial Fluctuations and the Power Spectrum	17
2.4.2	Baryon Acoustic Oscillations (BAOs)	20
2.5	Growth of Matter Density Fluctuations	20
2.6	The Spherical Collapse Model	22
2.7	Dark Matter Halos	24
2.7.1	The Halo Mass Function: Press-Schechter	24
2.7.2	Halo Bias	25
2.7.3	Halo Density Profiles: NFW and Einasto Models	26

3 Theoretical Foundations of Weak Gravitational Lensing	27
3.1 Introduction to Weak Gravitational Lensing	27
3.1.1 Derivation of the Lens Equation	27
3.1.2 The Jacobian (Lensing) Matrix \mathcal{A}	29
3.2 Convergence Field	31
3.2.1 Definition of Convergence in Real and Fourier Space	31
3.2.2 Convergence from Density Contrast	31
3.3 Shear Field	32
3.3.1 Definition of Shear	32
3.3.2 E-mode and B-mode Decomposition	32
3.4 Lensing Estimation	33
3.4.1 Galaxy Ellipticity and Reduced Shear	33
3.4.2 From Shear to Convergence	34
4 Statistical Measures and Non-Gaussian Signatures in Weak Lensing	36
4.1 Two-point Correlation Function	36
4.1.1 Overdensities and the Definition of the 2PCF	36
4.1.2 2PCF for Biased Tracers	36
4.2 Convergence Power Spectrum	36
4.2.1 Derivation of the Convergence Power Spectrum	37
4.2.2 Halofit Model	39
4.3 Convergence Bispectrum	39
4.3.1 BiHalofit Model	40
4.4 Probability Density Functions	41
4.4.1 Smoothing and Normalization Procedures	41
4.4.2 Practical Estimation of the Convergence PDF	42
4.4.3 hmpdf Model	42
4.5 Peak and Minimum Counts	42
4.6 Minkowski Functionals	44
4.6.1 Definition of Minkowski Functionals	44
4.6.2 Analytical Expressions in Gaussian Random Fields	45
5 Estimation of Covariance Matrix for Weak Lensing Statistics	46
5.1 The Role of the Covariance Matrix in Parameter Inference	47
5.1.1 Likelihood Functions and the Gaussian Approximation	47
5.1.2 Fisher Information and Parameter Constraints	47
5.2 Covariance of the Matter Power Spectrum	48

5.2.1	Shot Noise and Super-Sample Covariance	49
5.3	Covariance of the Angular Convergence Power Spectrum	50
5.4	Covariance of Higher-Order Weak Lensing Statistics	51
6	Numerical Simulations for Large Scale Structure and Weak Lensing	53
6.1	Introduction to Numerical Simulations in Cosmology	53
6.1.1	Dark Matter-Only vs. Hydrodynamical Simulations	53
6.1.2	Historical Evolution and Growth in Particle Number	54
6.2	Initial Condition Generation	54
6.2.1	Initial Density Field	54
6.2.2	Initial Displacement Field	55
6.2.3	Initial Velocities	56
6.3	N-Body Simulation Methods	56
6.3.1	Direct Summation	56
6.3.2	Particle-Mesh (PM) Method	57
6.3.3	Particle-Particle Particle-Mesh (P3M) Method	58
6.3.4	Tree-Particle-Mesh (Tree-PM) Method	58
6.4	Computational Tools and Optimization Techniques	59
6.4.1	Fast Fourier Transforms (FFT)	59
6.4.2	Mass Assignment Schemes	59
6.4.3	Parallelization Techniques	60
6.4.4	Adaptive Mesh Refinement (AMR)	61
6.4.5	Tree Construction	61
6.5	Advanced Codes and Methods: FASTPM	62
6.5.1	Modified Kick and Drift Factors	63
6.5.2	Algorithm Steps	64
6.6	Generating Weak Lensing Maps from Simulations	65
6.6.1	Conventional Ray-Tracing Algorithm	65
6.6.2	Born-approximated Ray-tracing	67
7	Simulation-Based Methodology for Assessing Higher-Order Weak Lensing Covariance	69
7.1	Constructing the BIGBOX and TILED Datasets	69
7.2	Producing Weak Lensing Convergence Maps at Multiple Redshifts	71
7.3	Incorporating Galaxy Shape Noise into Convergence Maps	72
7.4	Patch Selection and Projection	73
7.5	Applying Gaussian Kernels to Convergence Fields	76
7.6	Extracting Weak Lensing Statistics from Convergence Maps	78

7.6.1	Angular Power Spectrum	78
7.6.2	Bispectrum	78
7.6.3	PDF	79
7.6.4	Peak/Minima Counts	79
7.6.5	Minkowski Functionals	79
7.7	Comparing Covariances from BIGBOX and TILED	80
8	Comparative Analysis of Statistical Measures and Covariance Structures in BIGBOX and TILED	82
8.1	Comparison of Mean and Variance for Statistical Measures	82
8.2	Analysis of Covariance and Correlation Matrices	85
8.3	Effects of Noise on Statistical Measures	91
8.4	Influence of Smoothing Scale	94
8.5	Systematic Effects: Box Replication Artifact	97
9	Conclusions	102

List of Figures

1.1	Forecasted constraints on Ω_m and σ_8 from the Euclid mission using ten different higher-order statistics	7
2.1	Angular Power Spectrum (TT) of CMB Anisotropy	18
2.2	Linear Matter Power Spectrum by CLASS	19
3.1	Schematic representation of the lensing geometry	29
3.2	Illustration of Gravitational Lensing	30
4.1	Concept of Peaks/Minima Identification	43
4.2	Excursion sets of different thresholds	44
6.1	Evolution of the number of particles used in N -body simulations	55
6.2	Illustration of three mass assignment schemes	60
6.3	Illustration of adaptive mesh refinement	61
6.4	Illustration of an Octree decomposition	62
6.5	Parameter bias induced by the Born approximation	67

7.1	Spatial and redshift setup for the BIGBOX and TILED simulations	71
7.2	Illustration of a 5×5 patch at $z = 1.5$	72
7.3	Normalized lensing efficiency for multiple source redshifts	73
7.4	Convergence maps from the BIGBOX and TILED simulations	74
7.5	Visualization of the Fibonacci grid	74
7.6	Extraction of a patch from the full-sky convergence map using a Fibonacci grid . . .	76
7.7	Gaussian smoothing on a noisy convergence map for multiple smoothing scales . .	77
7.8	Average standard deviation of noiseless convergence maps	77
7.9	Average $\sigma_1 = \sqrt{\kappa_x^2 + \kappa_y^2}$ of the noiseless convergence maps	80
8.1	Comparison of Mean and Variance for $C_{\ell}^{\kappa\kappa}$ and Bispectrum	83
8.2	Comparison of Mean and Variance for Non-Correlation Statistics	84
8.3	Average BIGBOX/TILED Ratios of Covariance and Correlation Matrices	85
8.4	Covariance Matrices of Statistical Measures in BIGBOX Simulations	86
8.5	Covariance Matrices of Statistical Measures in TILED Simulations	87
8.6	Correlation Matrices of Statistical Measures in BIGBOX and TILED Simulations .	88
8.7	Ratios of Covariance Matrices between BIGBOX and TILED Simulations	89
8.8	Ratios of Correlation Matrices between BIGBOX and TILED Simulations	90
8.9	Average BIGBOX/TILED Ratio of Covariance for Multiple Noise Levels	92
8.10	BIGBOX/TILED Ratio of Covariance for Multiple Noise Levels	92
8.11	Average BIGBOX/TILED Ratio of Correlation for Multiple Noise Levels	93
8.12	BIGBOX/TILED Ratio of Correlation for Multiple Noise Levels	93
8.13	Average BIGBOX/TILED Ratio of Covariance for Multiple Smoothing Scales . .	95
8.14	BIGBOX/TILED Ratio of Covariance for Multiple Smoothing Scales	95
8.15	Average BIGBOX/TILED Ratio of Correlation for Multiple Smoothing Scales . .	96
8.16	BIGBOX/TILED Ratio of Correlation for Multiple Smoothing Scales	96
8.17	BIGBOX/TILED Ratios of the mean and variance of statistical measures for the RIPS and the RMPs	98
8.18	Average BIGBOX / TILED ratios of covariance matrices for the RIPS and the RMPs	99
8.19	Average BIGBOX / TILED ratios of correlation matrices for the RIPS and the RMPs	99
8.20	Covariance Ratios for RIP	100
8.21	Correlation Ratios for RIP	101

List of Tables

1.1	Comparison of Key Galaxy Surveys for Weak Lensing	3
6.1	Comparison of N -body simulation methods	57
7.1	Cosmological parameters used in the N-body simulations.	70
7.2	Summary of the statistical measures employed in this study, including their respective value ranges and the computational subroutines used for analysis.	78

Chapter 1

Introduction

Contents

1.1	Historical Overview	1
1.2	Astronomical Surveys and Observations	2
1.3	Constraint from Weak Lensing	4
1.4	Higher-Order Statistics in Weak Lensing	5
1.5	Aim of this Thesis	7
1.6	Structure of the Thesis	9

1.1 Historical Overview

Over the past century, cosmological observations have profoundly reshaped our understanding of the universe. From observations of [Hubble \(1925\)](#) measuring the distances to spiral nebulae, including the Andromeda Galaxy, it showed that these ‘nebulae’ were actually galaxies outside the Milky Way. Later in [Hubble \(1929\)](#), it was shown that galaxies are receding from us at velocities proportional to their distances, leading to the formulation of Hubble’s Law, and the revolutionary concept of an expanding universe. Years later, the discovery of the cosmic microwave background (CMB) radiation by [Penzias & Wilson \(1965\)](#) provided compelling evidence for the Big Bang theory, suggesting that the universe originated from a hot and dense state approximately 13.8 billion years ago. Subsequent satellite missions like the Cosmic Background Explorer (COBE; [Smoot et al. 1992](#)) and the Wilkinson Microwave Anisotropy Probe (WMAP; [Bennett et al. 2003](#)) measured the CMB with unprecedented precision finding anisotropies of $\sim 10^{-6}$ K. In the 1970s, Rubin and Ford analyzed galaxy rotation curves and found that galaxies rotate at speeds that cannot be accounted for by the visible matter alone ([Rubin & Ford, 1970](#); [Rubin et al., 1980](#)). This discrepancy provided strong evidence for the existence of dark matter, a mysterious form of matter that does not emit, absorb, or reflect light. Dark matter is now understood to constitute about 26% of the universe’s mass-energy content, while Baryon, making

up our visible world, constitutes only 5 %. The late 1990s witnessed the surprising discovery that the expansion of the universe is accelerating, based on observations of distant Type Ia supernovae by the Supernova Cosmology Project and the High-Z Supernova Search Team ([Riess et al., 1998](#); [Perlmutter et al., 1999](#)). This acceleration implies the existence of dark energy, an enigmatic force that permeates all of space and makes up approximately 68% of the universe’s total mass-energy budget. In 2015, the Laser Interferometer Gravitational-Wave Observatory (LIGO) made the first direct detection of gravitational waves providing direct evidence for the existence of gravitational waves, confirming a key prediction of General Relativity, opened a new window for observing cosmic events ([Abbott et al., 2016](#)). As observational technologies continue to advance, ongoing and future discoveries promise to further refine our understanding of the universe, addressing the remaining mysteries of dark matter, dark energy, and the fundamental forces shaping the universe.

From a theoretical standpoint, the cornerstone of modern cosmology is Einstein’s General Theory of Relativity, formulated in 1915 ([Einstein, 1915](#)). General Relativity provides the fundamental framework for explaining gravitational phenomena on cosmic scales, including the dynamics of the universe’s expansion, black holes, and gravitational lensing effects. Building upon Einstein’s equations, [Friedmann \(1922\)](#) and [Lemaître \(1931\)](#) independently derived solutions that describe a homogeneous and isotropic universe. These solutions led to the concept of an expanding or contracting universe and forms the mathematical foundation for the standard cosmological model. In the late 1940s, [Gamow \(1948\)](#), along with his collaborators [Alpher & Herman \(1948\)](#), proposed the Big Bang nucleosynthesis theory, which explains the formation of light elements like hydrogen and helium in the early universe. [Peebles \(1968\)](#), [Zeldovich & Sunyaev \(1969\)](#) further developed the theory of the recombination era, when the universe cooled enough for electrons and protons to combine into neutral hydrogen, allowing photons to travel freely, creating the CMB radiation. Subsequently, the theory of Baryonic Acoustic Oscillations (BAO) was introduced by [Sunyaev & Zeldovich \(1970\)](#), and independently by [Peebles & Yu \(1970\)](#), which describes the imprint of primordial sound waves in the distribution of galaxies and the CMB. To address the Big-Bang’s challenges, the concept of cosmic inflation was introduced by [Guth \(1981\)](#), [Linde \(1982\)](#), and others. Together, these theories contribute to a comprehensive picture of the universe’s origin, composition, and evolution.

1.2 Astronomical Surveys and Observations

Astronomical surveys are extensive observational projects designed to map large regions of the sky with high depth and precision, producing critical datasets for fundamental questions in astrophysics and cosmology. They aim to test the standard cosmological model (Λ CDM) by providing precise measurements that can confirm or challenge it, addressing issues like the Hubble tension—a discrepancy in expansion rate measurements from early ([Planck Collaboration et al., 2016](#)) and late ([Riess](#)

(et al., 2019) observations—and inconsistencies in parameters such as S_8 . Surveys also study the formation and evolution of cosmic structures by mapping millions of galaxies and dark matter distributions using techniques like cosmic shear and galaxy-galaxy lensing(Mandelbaum et al., 2013; Abbott et al., 2022).

These surveys employ different methodologies:

Imaging surveys capture wide-field images across multiple wavelengths to map cosmic structures and analyze galaxy populations (e.g., HSC (Aihara et al., 2018), SDSS (Kollmeier et al., 2019), DES (Abbott et al., 2018), LSST (Ivezić et al., 2019)), while spectroscopic surveys collect spectral data revealing redshifts, compositions, and kinematics essential for studying galaxy dynamics and the universe’s expansion (e.g., PFS (Tamura et al., 2016), BOSS (Dawson et al., 2013), DESI (DESI Collaboration et al., 2016), KiDS with spectroscopic extensions (de Jong et al., 2013)).

They can be ground-based, utilizing Earth-based telescopes but limited by atmospheric effects (e.g., HSC, DES, KiDS), or space-based, operating above Earth’s atmosphere for higher clarity and sensitivity, especially in inaccessible wavelengths (e.g., HST (Freedman et al., 2001), the upcoming Nancy Grace Roman Space Telescope(Spergel et al., 2015), and the Euclid mission(Refregier et al., 2010)).

Surveys are also classified into Stage-III and Stage-IV based on technological sophistication and scale (Albrecht et al., 2006). Stage-III surveys (e.g., DES, KiDS, HSC) represent the current generation aiming to refine cosmological parameters and deepen understanding of dark energy and dark matter. Stage-IV surveys (e.g., Rubin Observatory (Ivezić et al., 2019), DESI, the upcoming Roman Space Telescope) are the next generation characterized by scale and precision, aiming for high-precision cosmological measurements and deeper exploration of dark energy and dark matter.

Several significant galaxy surveys have been designed to measure weak lensing signals with high precision. Table 1.1 provides a comprehensive overview of four pivotal surveys focusing on their observational capabilities.

Table 1.1: Comparison of Key Galaxy Surveys for Weak Lensing

Survey	Area (deg ²)	Approx. Galaxy Density (arcmin ⁻²)	Median Redshift
DES/KiDS	~5,000	7	0.4
HSC Wide	~1,400	15	0.7
LSST	~18,000	30	1.0
Roman/Euclid	~2,000	50	1.5

The Dark Energy Survey (DES; The Dark Energy Survey Collaboration 2005; Abbott et al. 2018, 2021) utilized the 570-megapixel Dark Energy Camera (DECam; Flaugher et al. 2015) mounted on the 4-m Blanco Telescope at the Cerro Tololo Inter-American Observatory (CTIO) in Chile. Over the course of its operation, DES observed more than 300 million galaxies across approximately 5,000 deg² of the southern sky in five optical bands (g , r , i , z , Y). It achieved an effective galaxy

density of about $\sim 6 \text{ arcmin}^{-2}$ and provided photometric redshift estimates up to $z \sim 1.2$. The data collected by DES has made significant contributions to cosmology and astrophysics, including precise measurements of cosmic shear (Amon et al., 2022) and galaxy clustering (Abbott et al., 2022).

The Hyper Suprime-Cam Subaru Strategic Program (HSC-SSP; Aihara et al. 2018) comprises three layers: Wide, Deep, and UltraDeep, conducted with the 8.2-m Subaru Telescope equipped with the 870-megapixel Subaru Hyper Suprime-Cam (HSC; Miyazaki et al. 2018). The Wide layer covers approximately 1,400 deg 2 , yielding galaxy densities of around $\sim 15 \text{ arcmin}^{-2}$. Photometric redshifts extend up to $z \sim 2$. The superior imaging quality of HSC enhances the accuracy of weak lensing measurements and contributes to tighter cosmological constraints (Hikage et al., 2019). Currently, HSC is preparing its final data release (Y6) ending STAGE-III surveys.

The future Legacy Survey of Space and Time (LSST; LSST Science Collaboration et al. 2009; Ivezić et al. 2019) is conducted at the Vera C. Rubin Observatory. Over a 10-year period, LSST will survey approximately 18,000 deg 2 of the sky. It is expected to detect around 20 billion galaxies, corresponding to galaxy densities exceeding $\sim 30 \text{ arcmin}^{-2}$, with redshift measurements up to $z \sim 3$. LSST's vast dataset will substantially improve the statistical precision of weak lensing analyses and further refine cosmological models (LSST Dark Energy Science Collaboration, 2012).

Finally, the *Nancy Grace Roman Space Telescope* (Roman; Spergel et al. 2015) will conduct wide-field near-infrared imaging and spectroscopy from space scheduled for launch in the mid-2020s. Covering approximately 2,000 deg 2 . The expected galaxy densities exceed $\sim 50 \text{ arcmin}^{-2}$, facilitated by its space-based observations. The mission aims to provide spectroscopic redshifts higher than $z \sim 3$, significantly enhancing the precision of weak lensing measurements.

1.3 Constraint from Weak Lensing

While Λ CDM has been successful in explaining a wide range of cosmological observations, several tensions have emerged between different datasets. statistically significant discrepancy of about 4 to 5σ between the value of the Hubble constant (H_0) inferred from the Planck CMB measurements (Di Valentino et al., 2021) and the late-time measurements of local universe cosmic distance ladder measurements (Riess et al., 2022). In addition to the Hubble tension, discrepancies have been observed in the measurements of the parameter $S_8 \equiv \sigma_8 \sqrt{\Omega_m/0.3}$, where σ_8 represents the root-mean-square amplitude fluctuation of matter density measured in spheres of $8 h^{-1} \text{ Mpc}$, and Ω_m is the present-day matter density parameter. Several large-scale structure (LSS) experiments have reported 2 to 3σ lower values of S_8 compared to those inferred from Planck CMB data (Hikage et al., 2019; Asgari et al., 2021; García-García et al., 2021).

Some of the strongest constraints on S_8 from LSS observations come from the study of cosmic shear, which is the weak gravitational lensing of distant galaxies by the intervening LSS along the

line of sight. These small, coherent distortions in the shapes of background galaxies are sensitive to both the amplitude of matter density fluctuations (σ_8) and the growth of these fluctuations over cosmic time (Bartelmann & Schneider, 2001; Bartelmann, 2010; Kilbinger, 2015). While there is a degeneracy between Ω_m and σ_8 in cosmic shear analyses, the product S_8 is tightly constrained (Kilbinger, 2015; Mandelbaum, 2018). Assuming a flat Λ CDM cosmological model and utilizing cosmic shear catalogs, recent analyses from major surveys have measured the cosmological parameter S_8 : DES year 3 analysis reports $S_8 = 0.759^{+0.025}_{-0.023}$ (Amon et al., 2022; Secco et al., 2022) using two-point correlation functions (2PCFs) and $S_8 = 0.793^{+0.038}_{-0.025}$ (Doux et al., 2022) using power spectra (C_ℓ s). The KiDS-1000 analysis reports $S_8 = 0.759^{+0.024}_{-0.021}$ (Asgari et al., 2021) using 2PCFs and $S_8 = 0.754^{+0.027}_{-0.029}$ (Loureiro et al., 2022) using C_ℓ s. The HSC year 3 analysis measure $S_8 = 0.769^{+0.031}_{-0.034}$ (Li et al., 2023) using 2PCFs and $S_8 = 0.776^{+0.032}_{-0.033}$ (Dalal et al., 2023) using C_ℓ s.

As demonstrated in recent analyses, fully and robustly quantifying the cosmological constraints from cosmic shear necessitates accurate estimation and mitigation of various systematic sources and astrophysical effects, which are natural phenomena influencing observations (Dalal et al., 2023). Imperfect modeling of the Point Spread Function (PSF), which characterizes the telescope's response to point sources, can introduce systematic errors in galaxy shape measurements (Zhang et al., 2023b). Additionally, uncertainties in the redshift distribution, referring to errors in determining the distances to galaxies, can bias estimates of cosmological parameters (Zhang et al., 2023a). Shear calibration biases, which are systematic errors in measuring the distortion of galaxy shapes, encompass several specific issues: galaxy model bias resulting from incorrect models of galaxy shapes (Bernstein, 2010), noise bias introduced by measurement noise (Refregier et al., 2012), selection bias arising from the preferential selection of certain types of galaxies (Kaiser, 2000), and detection bias caused by errors in the detection process (Sheldon et al., 2020). These biases significantly impact the measured cosmic shear signal and are typically calibrated using image simulations (Mandelbaum et al., 2018b). Furthermore, baryonic feedback processes, which involve interactions from supernovae and active galactic nuclei (Mead et al., 2016; Chisari et al., 2018), and intrinsic alignments, referring to the non-random orientations of galaxies due to local gravitational fields (Joachimi et al., 2015; Kirk et al., 2015; Kiessling et al., 2015), must be carefully controlled to avoid biased cosmological inferences.

1.4 Higher-Order Statistics in Weak Lensing

Traditionally, the power spectrum has been the primary statistical measure used to quantify the distribution of matter density fluctuations in the universe (Hikage et al., 2019; Dalal et al., 2023). However, the weak lensing field is inherently non-Gaussian due to the nonlinear evolution of structures under gravity, leading to features resulting from gravitational collapse, mergers, and other astrophysical processes. The power spectrum, being a two-point statistic, captures only the Gaussian aspects of the

field and thus cannot fully characterize these non-Gaussian features.

To fully leverage the information contained in the weak lensing field, it is essential to employ higher-order statistics that are sensitive to the non-Gaussianities. Various higher-order statistics have been studied in the past, such as: higher-order moments (Petri et al., 2015; Gatti et al., 2020), Minkowski functionals (Marques et al., 2019; Grewal et al., 2022; Armijo et al., 2024), probability distribution function (Boyle et al., 2021; Thiele et al., 2023; Uhlemann et al., 2023), Peak and Minima Counts (Martinet et al., 2018; Marques et al., 2024), three-point statistics (Takada & Jain, 2004; Fu et al., 2014), and deep learning (Fluri et al., 2018, 2022). Employing these higher-order statistics enhances the cosmological constraining power of weak lensing analyses, potentially alleviating tensions in parameter estimates and providing deeper insights into the underlying physics.

Figure 1.1 (Euclid Collaboration et al., 2023) shows the forecasted constraints on the cosmological parameters Ω_m and σ_8 from the Euclid mission using ten different higher-order statistics. It is demonstrated that by combining any of these statistics with the standard two-point statistics, The constraints on Ω_m and σ_8 improve by a factor of 2 to 3 for individual parameters and by a factor of 4.5 for their combination. This highlights the potential of higher-order statistics to probe non-Gaussian features in the weak lensing field and enhance the precision of cosmological parameter estimates.

However, accurately estimating cosmological constraints from these higher-order statistics necessitates precise knowledge of the model uncertainties measured from the covariance matrices. The covariance matrix quantifies the uncertainties and correlations between different statistical measures and is crucial for techniques like Fisher forecasting and likelihood analyses that predict parameter constraints (Tegmark, 1997). To estimate these covariance matrices, we apply the same statistical measurements to a large ensemble of mock datasets that mimic real observations, accounting for the survey’s specific characteristics, such as cosmic variance (Seljak, 2009), shot noise (Wu et al., 2019) and super-sample covariance (SSC; Takada & Hu 2013). SSC arises from the correlation between observed modes and modes whose wavelengths are larger than the survey size. For instance, if the observed region is embedded in a large-scale super-survey overdensity, the structures within the survey have evolved faster compared to a region embedded in the cosmic mean density. For weak lensing surveys, these mock datasets are generated through ray-tracing simulations of light propagation through the universe, using light cones constructed from cosmological N-body simulations (Shirasaki et al., 2019; Euclid Collaboration et al., 2024).

One common approach is to stack multiple multi-resolution simulation boxes to generate non-repeating lightcones that cover a wide range of redshifts (Fosalba et al., 2015b; Crocce et al., 2015; Takahashi et al., 2017; DeRose et al., 2019). While this method successfully captures the evolution of structures over cosmic time, it can struggle with achieving high redshift resolution and requires significant computational resources. Alternatively, repeating a single simulation box multiple times along the line of sight to construct the lightcone retains high redshift resolution and is computationally

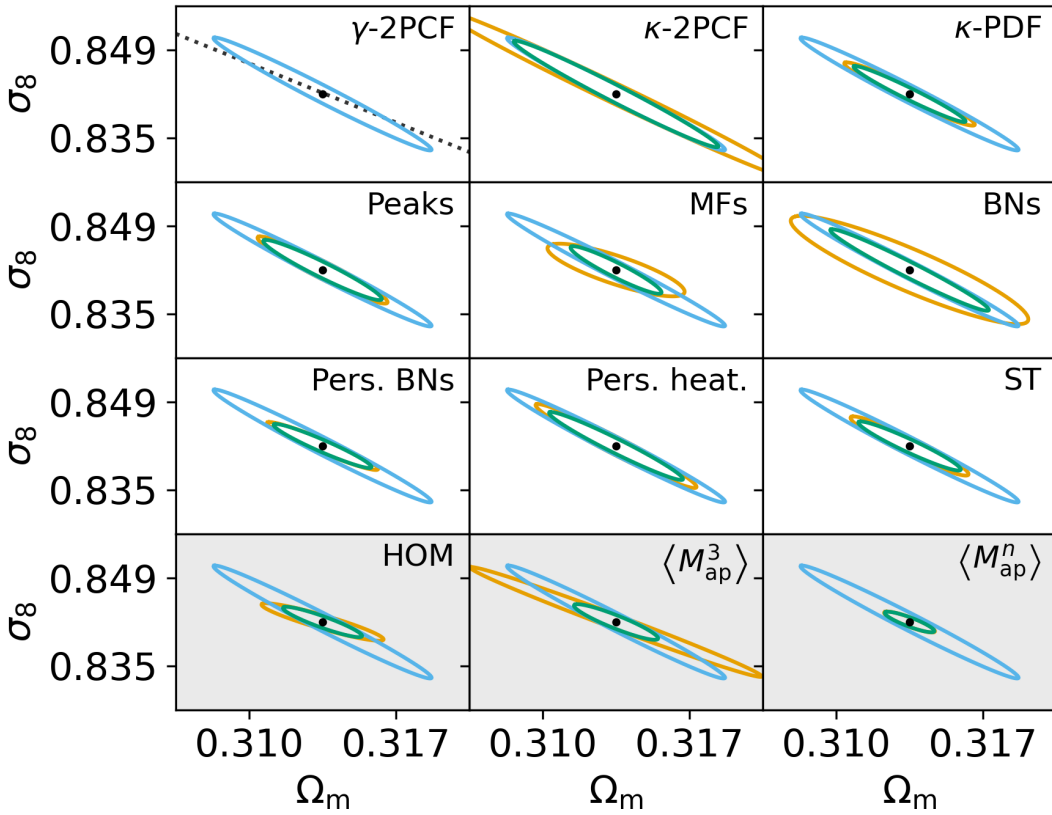


Figure 1.1: Forecasted constraints on Ω_m and σ_8 from the Euclid mission using ten different higher-order statistics. The figure demonstrates the potential improvements in parameter constraints achievable by incorporating higher-order statistics along with two-point statistics in weak lensing analyses. Figure adapted from [Euclid Collaboration et al. \(2023\)](#)

efficient ([Sehgal et al., 2010](#); [Liu et al., 2018](#); [Stein et al., 2020](#); [Omori, 2024](#)). However, this repetitive box method introduces artefacts like box replication effects ([Chen & Yu, 2024](#)). These effects can lead to underestimation of the variance on large scales and biases in the mean values of statistical measures, potentially impacting the estimation of cosmological parameters ([Zürcher et al., 2021](#)).

1.5 Aim of this Thesis

The overarching goal of this thesis is to enhance the precision and reliability of cosmological constraints derived from higher-order weak lensing statistics by addressing key challenges in the estimation of their covariance matrices. Specifically, we focus on the impact of super-sample covariance (SSC) and box replication effects in simulations used for weak lensing analyses.

While super-sample covariance has been extensively studied and is well-understood for the power spectrum ([Takada & Hu, 2013](#); [Barreira & Schmidt, 2017](#); [Barreira et al., 2018](#)), its influence on higher-order statistics remains largely unexplored. Existing theoretical predictions for covariances that include SSC effects ([Linke et al., 2023](#); [Uhlemann et al., 2023](#)) have not yet been thoroughly

tested for these higher-order statistic ([Euclid Collaboration et al., 2023](#)). Moreover, while the impact of SSC has been studied in three-dimensional (3D) box simulations ([Bayer et al., 2023](#)), its effects in two-dimensional (2D) weak lensing simulations have not been systematically examined.

Our first aim is to fill this gap by investigating how SSC affects higher-order weak lensing statistics and their covariance matrices. To achieve this, we conduct two sets of simulations:

BigBox Simulations — Large-volume simulations that naturally include super-survey modes, capturing the SSC effects inherent in the Universe’s large-scale structure.

Tiled Simulations — Simulations that replicate smaller boxes to cover the desired light cone, which will suppress super-survey modes and thus underestimate SSC.

By comparing the results from these two simulation strategies, we assess the extent to which SSC impacts the estimation of cosmological parameters using higher-order statistics. We examine how the covariance matrices are affected by varying smoothing scales and shape noise levels, which are crucial properties in weak lensing analyses. This comprehensive study allows us to determine the reliability of cosmological parameter estimations and to identify the conditions under which SSC effects become significant.

The second aim of this thesis is to investigate the impact of box replication effects in weak lensing simulations. As introduced earlier, the box replication is a common technique used to extend the effective simulation volume by periodically replicating a single simulation box along different axes. While this method is computationally efficient and retains high redshift resolution, it introduces artificial periodicity and can lead to under-predicts the variance of the imulations on large scales ([Zürcher et al., 2021](#)).

Previous studies have examined box replication effects primarily for power spectrum and other statistical moments, focusing on biases in mean values ([Chen & Yu, 2024](#)). Also, [Fluri et al. \(2019\)](#) studied the impact of the replication scheme on the predictions of the power spectrum and Convolutional Neural Networks (CNN) by increasing the boxsize and number of particles in a reference simulation while keeping the particle density constant. However, the impact on higher-order statistics and their covariance matrices has not been thoroughly explored. Considering that higher-order statistics are more and more used in weak lensing analyses, it is essential to understand how box replication affects these statistics and their covariance matrices. By investigating these effects, we aim to provide guidelines for future surveys to mitigate these artefacts and improve the accuracy of their cosmological parameter estimates.

By addressing these two key challenges, this thesis contributes to the broader effort of maximizing the scientific return of weak lensing surveys. Accurate covariance estimation is essential for improving the precision of cosmological parameter constraints derived from higher-order statistics, enhancing the utility of these statistics for probing the underlying physics of structure formation and

dark matter, and guiding the design of future survey experiments.

1.6 Structure of the Thesis

This thesis dissertation is organized into nine chapters that systematically develop the theoretical framework, methodologies, and empirical analyses pertinent to the research objectives outlined in the previous sections.

In Chapter 2, we provide a comprehensive overview of modern cosmology, tracing the historical development of the field and highlighting key theoretical milestones that have shaped our current understanding of the universe.

Chapter 3 focuses on the theoretical basic concepts and observational aspects of weak gravitational lensing.

In Chapter 4, we explore the summary statistics employed in weak lensing analyses to extract cosmological information from observational data, focusing on the power spectrum and higher-order statistics.

Chapter 5 addresses the theoretical prediction of covariance matrices including super-sample covariance and how the covariance affects the cosmological constraints.

In Chapter 6, we review the numerical methods in astrophysics and cosmology, focusing on the N-body simulations and weak lensing simulations.

In Chapter 7, we introduce the methodologies used in this thesis, including the simulation strategies, data generation, statistical measurements, and covariance matrix estimation.

In Chapter 8, we present the results of our analyses, comparing the mean values and covariance matrices of higher-order statistics derived from the BigBox and Tiled simulations, examining how SSC influences the variances and correlations in the data.

The thesis concludes with Chapter 9, where we summarize the key contributions and conclusions of this research. We reflect on how the work advances our understanding of super-sample covariance and box replication effects in the context of higher-order weak lensing statistics.

Chapter 2

Foundational Concepts in Modern Cosmology

Contents

2.1	Einstein Field Equations	10
2.2	FLRW Metric and the Friedmann Equations	13
2.3	Redshift and Cosmological Distances	15
2.4	Initial Conditions and the Primordial Universe	17
2.5	Growth of Matter Density Fluctuations	20
2.6	The Spherical Collapse Model	22
2.7	Dark Matter Halos	24

In this chapter, we provide an overview of the fundamental concepts and equations that underpin the field of cosmology following [Dodelson \(2003\)](#) and [Weinberg \(2008\)](#) textbooks.

2.1 From Einstein to Cosmology: The Einstein Field Equations

The Einstein Field Equations (EFE) are the fundamental equations of General Relativity, describing how matter and energy influence the curvature of spacetime. Introduced by [Einstein \(1915\)](#), these equations extend Newton's law of universal gravitation to a relativistic context, generalizing the definition of inertial observer in a spacetime which can be curved under the presence of a strong gravitational potential.

The EFE establish a relationship between the geometry of spacetime and the distribution of matter within it. They are expressed with the Minkowski Metric $g_{\mu\nu}$, which describes the curvature of spacetime, and the stress-energy tensor $T_{\mu\nu}$, which characterizes the distribution of matter and energy. The EFE are given by:

$$G_{\mu\nu} + \Lambda g_{\mu\nu} = \frac{8\pi G}{c^4} T_{\mu\nu}, \quad (2.1)$$

where Λ is the cosmological constant, G is the gravitational constant, and c is the speed of light. The

Einstein tensor $G_{\mu\nu}$ is defined by:

$$G_{\mu\nu} = R_{\mu\nu} - \frac{1}{2}Rg_{\mu\nu}, \quad (2.2)$$

the $R_{\mu\nu}$ is the Ricci tensor, which can be written using the Christoffel symbols $\Gamma_{\mu\nu}^\lambda$ of metric connection as:

$$R_{\mu\nu} = \partial_\lambda \Gamma_{\mu\nu}^\lambda - \partial_\nu \Gamma_{\mu\lambda}^\lambda + \Gamma_{\lambda\sigma}^\lambda \Gamma_{\mu\nu}^\sigma - \Gamma_{\mu\sigma}^\lambda \Gamma_{\lambda\nu}^\sigma, \quad (2.3)$$

the Ricci scalar R is given by:

$$R = g^{\mu\nu} R_{\mu\nu}, \quad (2.4)$$

2.1.1 The Stress-Energy Tensor for a Perfect Fluid

Assuming a perfect fluid as the source of the gravitational field, the stress-energy tensor is given by

$$T_{\mu\nu} = (\rho + p) u_\mu u_\nu + p g_{\mu\nu}, \quad (2.5)$$

where ρ is the energy density, p is the pressure, and u_μ is the four-velocity of the fluid. In a homogeneous and isotropic universe, u_μ is given by

$$u_\mu = (-c, 0, 0, 0), \quad (2.6)$$

Therefore, each component of the stress-energy tensor can be expressed as

$$T_{00} = \rho c^2, \quad T_{ij} = pg_{ij}, \quad (2.7)$$

2.1.2 Equations of State for Different Cosmic Components

Different species of matter and energy contribute to the energy density ρ and pressure P in the universe. The equation of state parameter w is defined as the ratio of pressure P to energy density ρ :

$$w = \frac{p}{\rho}. \quad (2.8)$$

For radiation, the equation of state parameter can be derived by considering the trace of the stress-energy tensor:

$$0 = T = g^{\mu\nu} T_{\mu\nu} = (\rho + p)(-1) + 4p = -\rho + 3p, \quad (2.9)$$

For non-relativistic matter where $p = 0$, the equation of state parameter is $w = 0$. For cosmological constant, the equation of state parameter can be derived by comparing the effective stress-energy of

the cosmological constant $T_{\mu\nu}^{(\Lambda)} = \rho_\Lambda g_{\mu\nu}$ to the stress-energy tensor of a perfect fluid:

$$\rho_\Lambda = \frac{\Lambda c^4}{8\pi G} \quad (2.10)$$

$$(\rho_\Lambda + p_\Lambda) u_\mu u_\nu + p_\Lambda g_{\mu\nu} = T_{\mu\nu}^{(\Lambda)} = \rho_\Lambda g_{\mu\nu} \quad (2.11)$$

$$\rho_\Lambda + p_\Lambda = 0 \quad (\text{valid for all } \mu, \nu)$$

$$p_\Lambda = -\rho_\Lambda \quad (2.12)$$

Therefore, the equation of state parameter for cosmological constant is $w = -1$.

To summarize, the Equation os States for each component of the universe are:

$$w = \begin{cases} 0 & \text{matter,} \\ \frac{1}{3} & \text{Radiation,} \\ -1 & \text{Cosmological Constant.} \end{cases} \quad (2.13)$$

In realistic universe, the energy density and pressure are contributed by multiple components. Assuming the interaction between different components is negligible, the total stress-energy tensor is the sum of the individual stress-energy tensors:

$$T_{\mu\nu} = \sum_i (T_i)_{\mu\nu}, \quad (2.14)$$

where i denotes the different components of the universe. Therefore, the total energy density and pressure are given by:

$$\rho = \sum_i \rho_i, \quad p = \sum_i p_i. \quad (2.15)$$

Unlike the conditions in the early Universe, when photons and baryons were tightly coupled, we now consider an epoch in which each component evolves independently, without any exchange of heat or other forms of energy. Under these assumptions, the conservation of energy-momentum for each component may be derived from the first law of thermodynamics. Specifically:

$$\begin{aligned} d(\rho_i a^3) &= -p_i d(a^3) \\ a^3 d\rho_i &= -\rho_i (1 + w_i) d(a^3) \quad (p_i = w_i \rho_i) \\ \ln \rho_i &= -3(1 + w_i) \ln a + \text{const.} \\ \rho_i &\propto a^{-3(1+w_i)}. \end{aligned} \quad (2.16)$$

where w_i is the equation of state parameter for the i -th component.

2.2 FLRW Metric and the Friedmann Equations

2.2.1 The FLRW Metric

The Friedmann-Lemaître-Robertson-Walker (FLRW) metric describes a homogeneous and isotropic universe. As obtained by [Weinberg \(1972\)](#):

$$ds^2 = -c^2 dt^2 + a^2(t) [d\chi^2 + f_K^2(\chi) (d\theta^2 + \sin^2 \theta d\phi^2)], \quad (2.17)$$

where $a(t)$ is the time evolving scale factor, χ is the comoving radial coordinate, and $d\Omega^2 = d\theta^2 + \sin^2 \theta d\phi^2$ represents the metric on the unit two-sphere. The function $f_K(\chi)$ encodes the spatial curvature of the universe and is defined as:

$$f_K(\chi) = \begin{cases} \frac{1}{\sqrt{-K}} \sinh(\sqrt{-K}\chi) & \text{for } K < 0, \\ \chi & \text{for } K = 0, \\ \frac{1}{\sqrt{K}} \sin(\sqrt{K}\chi) & \text{for } K > 0, \end{cases} \quad (2.18)$$

where K is the spatial curvature constant, with $K < 0$ corresponding to an open universe, $K = 0$ to a flat universe, and $K > 0$ to a closed universe.

2.2.2 Derivation of the Friedmann Equations

For the FLRW metric, the non-zero components of the Einstein tensor are:

$$G_{00} = 3 \left(\frac{\dot{a}}{a} \right)^2 + 3 \frac{Kc^2}{a^2}, \quad (2.19)$$

$$G_{ij} = - \left(2 \frac{\ddot{a}}{a} + \left(\frac{\dot{a}}{a} \right)^2 + \frac{Kc^2}{a^2} \right) a^2 g_{ij}, \quad (2.20)$$

where the dot denotes differentiation with respect to cosmic time t .

Substituting the components of $G_{\mu\nu}$ and $T_{\mu\nu}$ into the Einstein field equations (2.1), we obtain the Friedmann equations ([Friedmann, 1922](#)):

- First Friedmann equation (00 component):

$$3 \left(\frac{\dot{a}}{a} \right)^2 + 3 \frac{Kc^2}{a^2} + \Lambda c^2 = \frac{8\pi G}{c^4} \rho c^2 \quad (2.21)$$

$$\left(\frac{\dot{a}}{a} \right)^2 = \frac{8\pi G}{3} \rho - \frac{Kc^2}{a^2} + \frac{\Lambda c^2}{3} \quad (2.22)$$

- Second Friedmann equation (ii component):

$$-\left(2\frac{\ddot{a}}{a} + \left(\frac{\dot{a}}{a}\right)^2 + \frac{Kc^2}{a^2}\right)g_{ii} + \Lambda c^2 g_{ii} = \frac{8\pi G}{c^4}Pg_{ii} \quad (2.23)$$

$$\frac{\ddot{a}}{a} = -\frac{4\pi G}{c^4}P - \frac{1}{2}\left(\left(\frac{\dot{a}}{a}\right)^2 + \frac{Kc^2}{a^2} - \Lambda c^2\right) \quad (2.24)$$

$$\frac{\ddot{a}}{a} = -\frac{4\pi G}{3}\left(\rho + \frac{3P}{c^2}\right) + \frac{\Lambda c^2}{3} \quad (2.25)$$

2.2.3 Critical Density, Density Parameters, and H_0

Introducing the Hubble parameter H and the critical density ρ_c , we can simplify the Friedmann equations. The Hubble parameter is defined as:

$$H = \frac{\dot{a}}{a}, \quad (2.26)$$

and the critical density is defined as:

$$\rho_c = \frac{3H^2}{8\pi G}. \quad (2.27)$$

Substituting H and ρ_c into the first Friedmann equation (2.22), we obtain:

$$H^2 = H^2 \frac{\rho}{\rho_c} - \frac{Kc^2}{a^2} + \frac{\Lambda c^2}{3}. \quad (2.28)$$

Rearranging terms, we get:

$$1 = \frac{\rho}{\rho_c} - \frac{Kc^2}{a^2 H^2} + \frac{\Lambda c^2}{3H^2}. \quad (2.29)$$

Defining the density parameters:

$$\Omega_m = \frac{\rho_m}{\rho_c}, \quad \Omega_r = \frac{\rho_r}{\rho_c}, \quad \Omega_\Lambda = \frac{\rho_\Lambda}{\rho_c} = \frac{\Lambda c^2}{3H^2}, \quad \Omega_K = -\frac{Kc^2}{a^2 H^2}, \quad (2.30)$$

where ρ_m and ρ_r are the energy densities of matter and radiation, respectively, and ρ_Λ is the effective energy density associated with the cosmological constant, we can write the first Friedmann equation as:

$$1 = \Omega_r + \Omega_m + \Omega_K + \Omega_\Lambda. \quad (2.31)$$

2.2.4 Evolution of Density Parameters with Scale Factor

The evolution of the density parameters with the scale factor a can be derived from the conservation of energy-momentum and the equations of state. For matter-dominated and radiation-dominated

universes, the energy densities scale as:

$$\rho_m \propto a^{-3}, \quad \rho_r \propto a^{-4}. \quad (2.32)$$

Therefore, the corresponding density parameters vary with a as:

$$\Omega_m(a) = \Omega_{m0} a^{-3} \left(\frac{H_0}{H(a)} \right)^2, \quad \Omega_r(a) = \Omega_{r0} a^{-4} \left(\frac{H_0}{H(a)} \right)^2, \quad (2.33)$$

where the subscript 0 denotes present-day values, and H_0 is the current Hubble parameter. Conventionally, the Hubble parameter is parametrized as:

$$H_0 = 100 h \text{ km s}^{-1} \text{Mpc}^{-1}, \quad (2.34)$$

where h is a dimensionless parameter that accounts for the uncertainty in the exact value of H_0 and the cosmology assumed. It allows cosmological quantities to be expressed in a way that separates the dependence on the H_0 . Combining these expressions, the Friedmann equation (2.31) can be rewritten in terms of the present-day density parameters:

$$\left(\frac{H(a)}{H_0} \right)^2 = \Omega_{r0} a^{-4} + \Omega_{m0} a^{-3} + \Omega_{K0} a^{-2} + \Omega_{\Lambda0}, \quad (2.35)$$

which describes the evolution of the Hubble parameter with scale factor a in terms of the contributions from radiation, matter, curvature, and the cosmological constant.

2.3 Redshift and Cosmological Distances

The expansion of the universe causes the wavelength of light to stretch as it propagates through space. This effect, known as cosmological redshift, is a direct consequence of the expansion of the universe and is described by the scale factor $a(t)$.

Before going into the details of the redshift, we first introduce the concept of the null geodesic $ds^2 = 0$, which describes the path of light in a curved spacetime. Then, the radial coordinate distance for a photon traveling from a source to the observer is obtained from the null condition:

$$ds^2 = 0 \quad \Rightarrow \quad d\chi = \frac{c dt}{a(t)}. \quad (2.36)$$

Integrating this expression, we obtain the comoving radial distance χ as:

$$\chi = \int_{t_e}^{t_0} \frac{c dt'}{a(t')} \quad (2.37)$$

where t_0 is the present time, and t_e is the time at which the light is emitted. Suppose a light is emitted at time $t = t_e$ with wavelength λ_e and received at time $t = t_0$ with wavelength λ_0 . Then, the same phase emitted at time $t = t_e + \Delta t_e$ is received at time $t = t_0 + \Delta t_0$. The comoving distance between the source and the observer is given by:

$$\chi = \int_{t_e}^{t_0} \frac{c dt'}{a(t')} = \int_{t_e + \Delta t_e}^{t_0 + \Delta t_0} \frac{c dt'}{a(t')}. \quad (2.38)$$

Assuming the scale factor $a(t)$ change is negligible over the time interval Δt , we can expand the integrand in Eq. (2.38) to first order:

$$\int_{t_e + \Delta t_e}^{t_0 + \Delta t_0} \frac{c dt'}{a(t')} - \int_{t_e}^{t_0} \frac{c dt'}{a(t')} = \frac{c \Delta t_e}{a(t_e)} - \frac{c \Delta t_0}{a(t_0)} = 0. \quad (2.39)$$

Therefore, the fractional change in the wavelength of light is given by:

$$\frac{\lambda_0 - \lambda_e}{\lambda_e} = \frac{a(t_0)}{a(t_e)} - 1, \quad (2.40)$$

This shift in the wavelength of light is known as the cosmological redshift z , defined as:

$$z := \frac{\lambda_0 - \lambda_e}{\lambda_e} = \frac{a(t_0)}{a(t_e)} - 1, \quad (2.41)$$

Therefore, the redshift z serves us a measure of position in the expanding universe, with $z = 0$ corresponding to the present time and $z \rightarrow \infty$ corresponding to the time of the Big Bang. However, the space-time is not static nor flat, there are several distance measures that are used to describe the separation between two objects in the universe. A characteristic length scale is the Hubble distance, defined as the inverse of the Hubble parameter:

$$d_H = \frac{c}{H_0} = 9.26 \times 10^{25} h^{-1} \text{m} \quad (2.42)$$

The most common distance measures are the comoving distance, the luminosity distance, and the angular diameter distance.

2.3.1 Luminosity Distance

The luminosity distance $d_L(z)$ is a measure of observed distance broadly used in Astronomy and Cosmology, relating the intrinsic luminosity L of a source to the observed flux F via the inverse-square law (Carroll et al., 1992):

$$F = \frac{L}{4\pi d_L^2}. \quad (2.43)$$

In an expanding universe, the luminosity distance accounts for the effects of redshift on both the energy of photons and the rate at which they are received. It is defined as (Hogg, 1999):

$$d_L(z) = (1 + z) f_K(\chi(z)). \quad (2.44)$$

The luminosity distance is crucial for determining cosmological parameters using standard candles, such as Type Ia supernovae, whose intrinsic luminosities are known (Riess et al., 1998). By measuring the observed flux F and applying Eq. (2.43), we can infer $d_L(z)$ and constrain cosmological models.

2.3.2 Angular Diameter Distance

The angular diameter distance $d_A(z)$ relates the physical size D of an object to its observed angular size:

$$\theta = \frac{D}{d_A}. \quad (2.45)$$

In an expanding universe, the angular diameter distance is given by (Hogg, 1999):

$$d_A(z) = \frac{f_K(\chi(z))}{1 + z}. \quad (2.46)$$

The angular diameter distance is essential for studying standard rulers, such as the scale of baryon acoustic oscillations (BAO) in the cosmic microwave background and large-scale structure (Eisenstein et al., 2005). By measuring the angular size θ of these features and knowing their physical size D , we can determine $d_A(z)$ and thus constrain cosmological parameters.

2.4 Initial Conditions and the Primordial Universe

The initial conditions of the universe are believed to originate from quantum fluctuations during the inflationary epoch. These fluctuations are imprinted on the cosmic microwave background (CMB) radiation, which provides a snapshot of the universe at the time of recombination ($z \sim 1100$), and these primordial perturbations served as the seeds for the formation of the large-scale structures (LSS) observed today

Figure 2.1 illustrates the CMB temperature power spectrum (TT) measured by the Planck satellite (Planck Collaboration et al., 2014), showing the primordial fluctuations imprinted at large angular scales ($\ell \lesssim 30$).

2.4.1 Primordial Fluctuations and the Power Spectrum

The standard single-field slow-roll inflation model predicts that the primordial fluctuations are nearly scale-invariant and Gaussian (Dodelson, 2003). The matter power spectrum of these primordial cur-

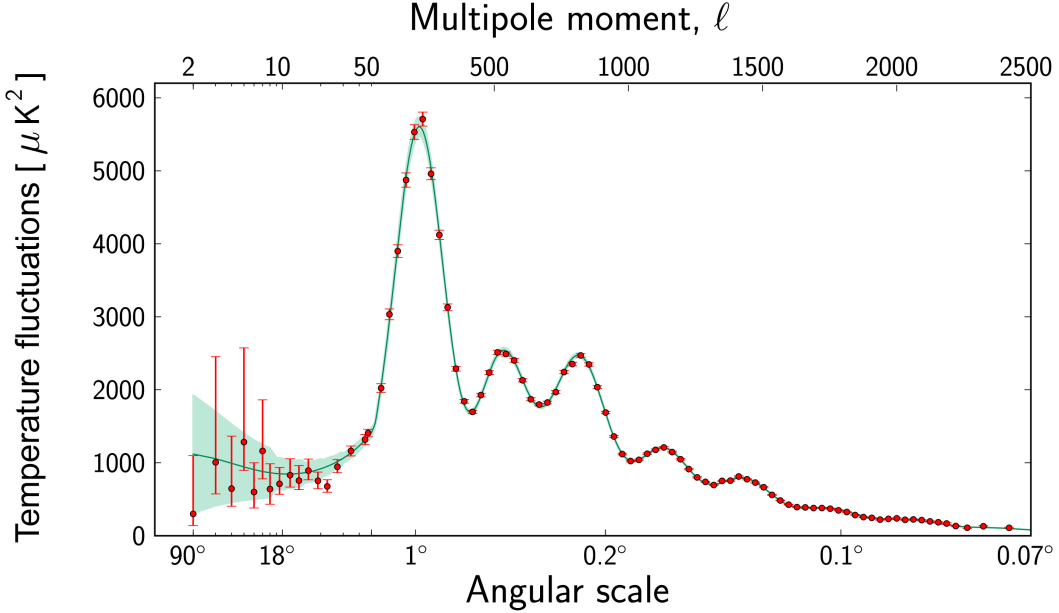


Figure 2.1: Angular Power Spectrum of Cosmic Microwave Background Temperature Fluctuations as a function of the multipole moment (ℓ) and the corresponding angular scale. The observational data are depicted by red markers with associated error bars, whereas the theoretical prediction derived from the Λ CDM cosmological model is represented by the green curve (Planck Collaboration et al., 2014). The primordial fluctuations imprinted at large angular scales ($\ell \lesssim 30$).

vature perturbations is described by a nearly scale-invariant power-law form:

$$P_p(k) = A_s \left(\frac{k}{k_*} \right)^{n_s - 1}, \quad (2.47)$$

where A_s is the amplitude of the scalar fluctuations, k_* is the pivot scale, and n_s is the spectral index. The observational constraints on these parameters are provided by the Planck satellite (Planck Collaboration et al., 2020):

$$A_s = (2.101_{-0.034}^{+0.031}) \times 10^{-9}, \quad n_s = 0.965 \pm 0.004. \quad (2.48)$$

for the pivot scale $k_* = 0.05 \text{ Mpc}^{-1}$.

As the universe evolves, various physical processes, such as radiation pressure, baryon-photon interactions, and dark matter dynamics, influence the growth of these initial perturbations. These effects are encapsulated in the transfer function $T(k)$, which modifies the primordial power spectrum to give the linear matter power spectrum at redshift z (Dodelson, 2003):

$$P(k, z) = P_p(k) T^2(k) D^2(z), \quad (2.49)$$

where $D(z)$ is the linear growth factor that describes the growth of perturbations in the linear regime, where each k -mode evolves independently of the others. The growth factor is given by:

$$D(a) = \frac{5\Omega_m a}{2} \int_0^1 \frac{dx}{(\Omega_m/x + \Omega_\Lambda x^2 + 1 - \Omega_m - \Omega_\Lambda)^{3/2}}, \quad (2.50)$$

where at the limit $a \rightarrow 0$, $D(a) \rightarrow a$.

The shape of $T(k)$ is determined by the Einstein-Boltzmann equations of a mixture of various energy components. Thus, there is no exact analytical form for $T(k)$; instead, it is typically computed using numerical codes such as CAMB (Lewis et al., 2000) and CLASS (Blas et al., 2011).

Qualitatively, the transfer function behaves differently on scales relative to the equality scale k_{eq} . Since in the radiation-dominant era, the growth of perturbations on super-horizon scales is suppressed compared to those on sub-horizon scales. In the matter-dominant era, the growth of perturbations is the same on super-horizon and sub-horizon scales. Due to this, the transfer function behaves as:

$$T(k) \propto \begin{cases} 1 & \text{for } k \ll k_{\text{eq}} \text{ Top-hat}, \\ k^{-2} & \text{for } k \gg k_{\text{eq}} \text{ Power-law.} \end{cases} \quad (2.51)$$

Figure 2.2 shows the linear matter power spectrum computed using the CLASS code. It is clear that the scaling of the linear power spectrum changes around k_{eq} . The wiggles around $k \sim 0.1 h/\text{Mpc}$ are due to Baryon Acoustic Oscillations (BAOs) imprinted.

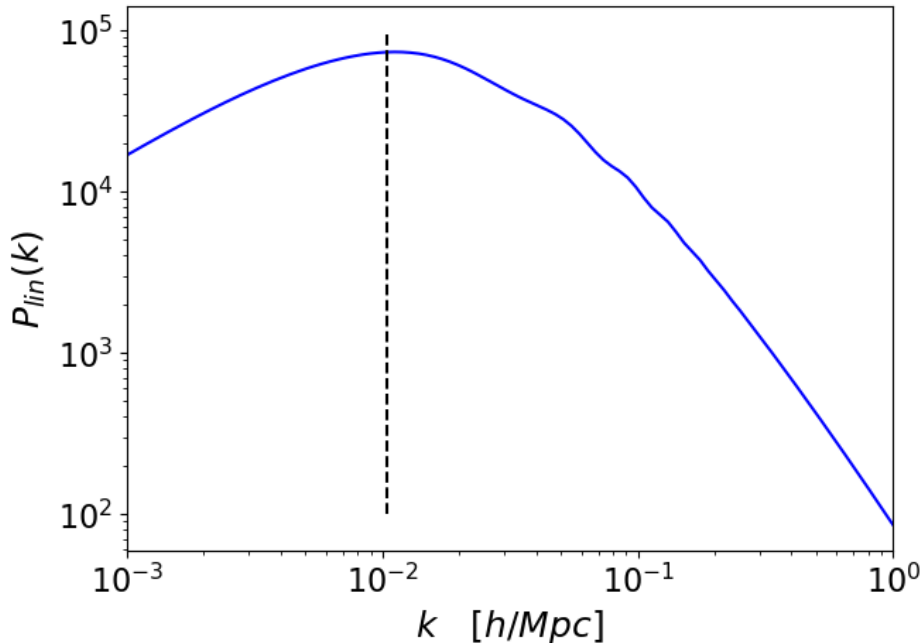


Figure 2.2: The linear matter power spectrum as a function of the wavenumber k computed using the CLASS code. The transition from the radiation-dominated to the matter-dominated era is evident around $k_{\text{eq}} = 0.0104 h/\text{Mpc}$ (Planck Collaboration et al., 2020).

2.4.2 Baryon Acoustic Oscillations (BAOs)

BAOs serve as a standard ruler for cosmological distance measurements and are crucial for constraining cosmological parameters. These features originate from the oscillatory behavior of the photon-baryon plasma in the primordial universe prior to the epoch of recombination. During this period, photons and baryons are tightly coupled, effectively forming a coherent photon-baryon fluid. The coupling between photons and baryons is quantitatively characterized by the baryon-to-photon momentum density ratio, R , defined as:

$$R = \frac{\Pi_b}{\Pi_\gamma} = \frac{\rho_b \mathbf{v}_b}{(1 + \frac{1}{3}) \rho_\gamma \mathbf{v}_\gamma} = \frac{3\rho_b}{4\rho_\gamma}, \quad (2.52)$$

where ρ_b and ρ_γ denote the baryon and photon energy densities, respectively, while \mathbf{v}_b and \mathbf{v}_γ represent their respective velocities.

The propagation of acoustic waves within the photon-baryon plasma is governed by the effective sound speed, c_s , which arises from the interplay between radiation pressure and gravitational infall. The effective sound speed is derived from the effective pressure and energy density of the photon-baryon fluid:

$$\begin{aligned} c_s^2 &= \frac{\partial p_{\text{eff}}}{\partial \rho_{\text{eff}}} = \frac{\partial p_\gamma}{\partial (\rho_b + \rho_\gamma)} \\ &= \frac{1}{1 + R} \frac{\partial p_\gamma}{\partial \rho_\gamma} = \frac{1}{1 + R} \cdot \frac{1}{3} \\ c_s &= \frac{1}{\sqrt{3(1 + R)}}, \end{aligned} \quad (2.53)$$

where p_γ and ρ_γ are the photon pressure and energy density, respectively.

The acoustic oscillations in the photon-baryon plasma can be described by solutions to the linearized perturbation equations (Eq (2.66); we will discuss in the next section). Therefore, the evolution of the photon-baryon plasma scales as:

$$\delta_\gamma(k, t) \propto \cos(kc_s t + \phi), \quad (2.54)$$

where k is the wavenumber and ϕ is the phase constant.

2.5 Growth of Matter Density Fluctuations

Density fluctuations arise from quantum fluctuations during inflation and grow under the influence of gravity. Starting from the continuity and Euler equations, which govern the conservation of mass

and momentum, respectively:

$$\frac{\partial \rho}{\partial t} + \nabla \cdot (\rho v) = 0, \quad (2.55)$$

$$\frac{\partial v}{\partial t} + (v \cdot \nabla)v = -\frac{\nabla P}{\rho} - \nabla \Phi, \quad (2.56)$$

where ρ is the density, v is the peculiar velocity field, P is the pressure, and Φ is the gravitational potential.

To analyze perturbations in an expanding universe, we move to comoving coordinates and express the density as a perturbation around the mean density, $\rho = \bar{\rho}(1 + \delta)$, where δ is the density contrast. The continuity and Euler equations then become:

$$\frac{\partial \delta}{\partial t} + \frac{1}{a}\nabla \cdot ((1 + \delta)v) = 0, \quad (2.57)$$

$$\frac{\partial v}{\partial t} + Hv + \frac{1}{a}(v \cdot \nabla)v = -\frac{\nabla \delta P}{a\bar{\rho}(1 + \delta)} - \frac{1}{a}\nabla \Phi, \quad (2.58)$$

where $a(t)$ is the scale factor, and $H = \dot{a}/a$ is the Hubble parameter.

To derive the equation of motion for the density contrast, we linearize the above equations under the assumption that $\delta \ll 1$ and v is small. Neglecting higher-order terms in δ and v , we obtain the linearized equations:

$$\frac{\partial \delta}{\partial t} + \frac{1}{a}\nabla \cdot v = 0, \quad (2.59)$$

$$\frac{\partial v}{\partial t} + Hv = -\frac{\nabla \delta P}{a\bar{\rho}} - \frac{1}{a}\nabla \Phi. \quad (2.60)$$

The gravitational potential Φ is related to the density contrast via Poisson's equation in comoving coordinates:

$$\nabla^2 \Phi = 4\pi G \bar{\rho} a^2 \delta, \quad (2.61)$$

where G is the gravitational constant. Assuming adiabatic perturbations, the pressure perturbation is related to the density perturbation by $\delta P = c_s^2 \delta \rho = c_s^2 \bar{\rho} \delta$, where c_s is the sound speed.

Taking the time derivative of the linearized continuity equation (2.59) and substituting the divergence of v from the linearized Euler equation (2.60), we obtain:

$$\frac{\partial^2 \delta}{\partial t^2} + 2H \frac{\partial \delta}{\partial t} - \frac{c_s^2}{a^2} \nabla^2 \delta = 4\pi G \bar{\rho} \delta. \quad (2.62)$$

Transforming to Fourier space, where $\nabla^2 \delta \rightarrow -k^2 \tilde{\delta}(k, t)$, the equation becomes:

$$\ddot{\tilde{\delta}}(k, t) + 2H\dot{\tilde{\delta}}(k, t) + \left(\frac{c_s^2 k^2}{a^2} - 4\pi G \bar{\rho} \right) \tilde{\delta}(k, t) = 0, \quad (2.63)$$

where $\tilde{\delta}(k, t)$ is the Fourier transform of the density contrast.

Defining the effective frequency squared $\omega^2(k, t) = 4\pi G \bar{\rho} - \frac{c_s^2 k^2}{a^2}$, the equation simplifies to:

$$\ddot{\tilde{\delta}}(k, t) + 2H\dot{\tilde{\delta}}(k, t) - \omega^2(k, t)\tilde{\delta}(k, t) = 0. \quad (2.64)$$

The solutions to this differential equation depend on the sign of $\omega^2(k, t)$:

- **Gravity-Dominated Regime ($\omega^2(k, t) > 0$)**: For large-scale perturbations where gravity overcomes pressure forces (i.e., small k), the solutions are exponential:

$$\tilde{\delta}(k, t) = C_1 e^{\lambda t} + C_2 e^{-\lambda t}, \quad (2.65)$$

where $\lambda = \sqrt{\omega^2(k, t)}$. The growing mode ($e^{\lambda t}$) leads to the amplification of perturbations and structure formation, while the decaying mode ($e^{-\lambda t}$) becomes negligible over time.

- **Pressure-Dominated Regime ($\omega^2(k, t) < 0$)**: For small-scale perturbations where pressure resists gravitational collapse (i.e., large k), the solutions are oscillatory:

$$\tilde{\delta}(k, t) = e^{-Ht} (C_1 \cos(|\omega(k, t)|t) + C_2 \sin(|\omega(k, t)|t)). \quad (2.66)$$

The perturbations oscillate with frequency $|\omega(k, t)|$ and are damped by the cosmic expansion, preventing collapse on small scales.

These results illustrate the Jeans instability criterion, which states that perturbations grow only if their wavelength exceeds the Jeans length $\lambda_J = c_s \sqrt{\frac{\pi}{G \bar{\rho}}}$ (Jeans, 1902).

2.6 The Spherical Collapse Model

As gravity is attractive force, ambient matter falls into such high density regions, which results in formation of halos. The spherical collapse model (Gunn & Gott, 1972) provides a simplified description of the formation of cosmic structures by considering the evolution of a spherically symmetric overdensity in an expanding universe. Suppose that there is spherical matter around a certain point in the Universe and initial density contrast is denoted as $\delta_i \ll 1$. The equation of motion of the shell which the radius R is given by:

$$\ddot{R} = -\frac{GM(< R)}{R^2}, \quad (2.67)$$

where $M(< R)$ is the mass enclosed within the radius R . Multiplying both sides by \dot{R} and integrating over time, we get:

$$\dot{R}^2 = \frac{2GM(< R)}{R} + E. \quad (2.68)$$

The constant E corresponds to the energy, $E < 0$ for bound systems. From this expression, we can obtain a parametric solution for the radius $R(t)$ in term of θ :

$$R(t) = (GM)^{1/3} A^2 (1 - \cos \theta) \quad (2.69)$$

$$t = A^3 (\theta - \sin \theta) \quad (2.70)$$

where A is a constant. For a matter-dominated universe, the mean density $\bar{\rho} = (6\pi G t^2)^{-1}$. The density contrast within the shell is given by:

$$1 + \delta = \frac{\rho}{\bar{\rho}} = \frac{3M}{4\pi R^3} \frac{6\pi G t^2}{M} = \frac{9}{2} \frac{(\theta - \sin \theta)^2}{(1 - \cos \theta)^3} \quad (2.71)$$

$\theta = \pi$ corresponds to the turnaround point, where the shell reaches its maximum radius and starts collapsing. The density contrast at the turnaround point is given by:

$$\delta_{ta} = \frac{9\pi^2}{16} - 1 \approx 4.55 \quad (2.72)$$

where the corresponding radius R_{ta} and time t_{ta} are:

$$R_{ta} = 2(GM)^{1/3} A^2, \quad t_{ta} = \pi A^3 \quad (2.73)$$

At $\theta = 2\pi$, the shell reaches a singularity where the radius R goes to zero and the density contrast δ diverges. However, in reality, this does not occur because the shell undergoes virialization and forms a halo. We assume the shell virializes at $R = R_{ta}/2$ at time $t = t_{coll}$. The density contrast at virialization is given by:

$$\delta_{coll} = \delta_{ta} \times 4 \times 2^3 = 18\pi^2. \quad (2.74)$$

In the early epoch ($\theta \ll 1$), the density contrast follows the linear theory. If we expand the density contrast and time around $\theta = 0$, we get:

$$\delta = \frac{3}{20}\theta^2 + \mathcal{O}(\theta^4), \quad t = \frac{A^3}{6}\theta^3 + \mathcal{O}(\theta^5) \quad (2.75)$$

This yields $\delta \propto t^{2/3}$, which is consistent with linear theory. Denoting this linear fluctuation as $\delta_L(t)$:

$$\delta_L(t) = \frac{3(6t)^{2/3}}{20A^2} \quad (2.76)$$

Substituting $t = t_{\text{ta}}$ and $t = t_{\text{coll}}$, we obtain:

$$\delta_L(t_{\text{ta}}) = \frac{3(6\pi)^{2/3}}{20} \approx 1.06, \quad \delta_L(t_{\text{coll}}) = \frac{3(12\pi)^{2/3}}{20} \approx 1.69. \quad (2.77)$$

Therefore, when the linear density contrast exceeds $\delta_L \approx 1.69$, the shell virializes and forms a halo.

2.7 Dark Matter Halos

Dark matter halos are the fundamental building blocks of cosmic structures. They form through the gravitational collapse of overdense regions in the early universe and provide the potential wells in which baryonic matter accumulates to form galaxies and galaxy clusters.

2.7.1 The Halo Mass Function: Press-Schechter

The halo mass function (HMF) describes the number density of dark matter halos as a function of their mass and redshift. The Press-Schechter (PS) formalism (Press & Schechter, 1974) provides an analytical approach to calculate the HMF based on the initial Gaussian density field and the theory of gravitational collapse.

Let us consider the density field which follows Gaussian distribution at each position. The probability distribution function is:

$$P(\delta)d\delta = \frac{1}{\sqrt{2\pi}\sigma^2} \exp\left(-\frac{\delta^2}{2\sigma^2}\right) d\delta \quad (2.78)$$

where σ^2 is the variance of the density field. Supposed that the sphere of radius R contains mass $M = \frac{4}{3}\pi R^3 \bar{\rho}$, where $\bar{\rho}$ is the mean density. The density contrast within this sphere is:

$$\delta_M(q, t) = \frac{3}{4\pi} \int_{|q' - q| < R} \delta(q', t) d^3 q' \quad (2.79)$$

This density contrast follows Gaussian distribution. The probability distribution function of the density contrast is:

$$P(\delta_M) = \frac{1}{\sqrt{2\pi\sigma^2(M)}} \exp\left(-\frac{\delta_M^2}{2\sigma^2(M)}\right) \quad (2.80)$$

The halo formation happens when the density contrast exceeds a critical value δ_c . The fraction of Lagaranian volume which collapses to form halos is:

$$P_{>\delta_c} = \int_{\delta_c}^{\infty} P(\delta_M) d\delta_M = \frac{1}{\sqrt{2\pi}} \int_{\delta_c/\sigma(M)}^{\infty} e^{-x^2/2} dx \quad (2.81)$$

Thus, mass which forms dark halo with more than mass M can be calculated as $\bar{\rho}_0 P_{>\delta_c}$. In Press-

Schechter formalism, the mass function is given by:

$$n(M)MdM = 2\bar{\rho}_0 \left| \frac{P_{\delta_c}}{d\sigma(M)} \right| \left| \frac{d\sigma(M)}{dM} \right| dM \quad (2.82)$$

Substituting Eq. (2.81) into the above equation, we obtain:

$$n(M) = \sqrt{\frac{2}{\pi}} \frac{\bar{\rho}_0}{M \sigma^2(M)} \left| \frac{d\sigma}{dM} \right| e^{-\delta_c^2/2\sigma^2(M)} \quad (2.83)$$

The mass function can be further simplified by using the relation between the variance of the density field and the linear power spectrum $P(k)$:

$$\sigma^2(M) = \int \frac{d^3k}{(2\pi)^3} P(k) W^2(kR) \quad (2.84)$$

where $W(kR)$ is the Fourier transform of the top-hat window function:

$$\begin{aligned} W(kR) &= \int d^3x e^{ik \cdot x} W_R(x) \\ &= 4\pi \int_0^R x^2 dx \frac{\sin(kx)}{kx} W_R(x) \\ &= \frac{3}{(kR)^3} [\sin(kR) - kR \cos(kR)] \end{aligned} \quad (2.85)$$

Finally, we can construct the Press-Schechter mass function only from the linear power spectrum $P(k)$. In reality, matter collapses into halos non-spherically. One of the most popular extensions of the Press-Schechter formalism is the Sheth-Tormen mass function ([Sheth & Tormen, 1999](#)), which provides a better fit to numerical simulations by incorporating ellipsoidal collapse.

2.7.2 Halo Bias

Halo bias quantifies how dark matter halos are biased tracers of the underlying matter distribution. Massive halos tend to form in regions of higher density contrast, leading to a mass-dependent bias factor $b(M)$ which is independent for a convenient scale. [Mo & White \(1996\)](#) proposed a simple model for halo bias based on the Press-Schechter formalism and the spherical collapse model. They derive the analytical expression for the linear halo bias, which defined as:

$$b_h(M, z) := \frac{\delta_h(M, z)}{\delta_m} \quad (2.86)$$

where $\delta_h(M, z)$ is the overdensity of halos of mass M at redshift z , and δ_m is the overdensity of the matter field. In the lowest-order approximation, the linear halo bias is given by:

$$b_h(M, z) = 1 + \frac{\nu(M, z)^2 - 1}{\delta_c} \quad (2.87)$$

where $\nu(M, z) = \delta_c/\sigma(M, z)$ is the peak height, and δ_c is the critical density contrast for collapse. It is then extended by [Sheth et al. \(2001\)](#) to include ellipsoidal collapse.

2.7.3 Halo Density Profiles: NFW and Einasto Models

Since halos undergo nonlinear gravitational evolution, their density profiles need numerical simulations to be determined. The most widely used model is the Navarro-Frenk-White (NFW) profile ([Navarro et al., 1996, 1997](#)), which is found universally in numerical simulations. The NFW profile is given by:

$$\rho_{\text{NFW}}(r) = \frac{\rho_s}{(r/r_s)(1+r/r_s)^2} \quad (2.88)$$

where ρ_s and r_s are the characteristic density and scale radius, respectively. At large radii, the NFW profile follows a power-law behavior $\rho_{\text{NFW}} \propto r^{-3}$, while at small radii, it behaves as $\rho_{\text{NFW}} \propto r^{-1}$. The enclosed mass is not well defined for the NFW profile, so the virial radius r_{vir} and r_{200c} , which encloses a density contrast of 200 times the critical density, are used instead.

After specifying the boundary, one can compute the halo mass as ([Oguri & Hamana, 2011](#)):

$$M_{\text{vir}} = 4\pi r_s^3 \rho_s m(c_{\text{vir}}) \quad (2.89)$$

with

$$m(c) = \int_0^c \frac{x dx}{(1+x)^2} = \ln(1+c) - \frac{c}{1+c} \quad (2.90)$$

where $c_{\text{vir}} = r_{\text{vir}}/r_s$ is the concentration parameter.

Another widely used profile is the Einasto profile ([Einasto, 1965](#)), which provides an alternative fitting function with more accuracy at relatively small halo radius. The Einasto profile is given by:

$$\rho_{\text{Ein}}(r) = \rho_s \exp \left(-\frac{2}{\alpha} \left[\left(\frac{r}{r_s} \right)^\alpha - 1 \right] \right) \quad (2.91)$$

where ρ_s and r_s are the characteristic density and scale radius, respectively, and α is the shape parameter.

Chapter 3

Theoretical Foundations of Weak Gravitational Lensing

Contents

3.1	Introduction to Weak Gravitational Lensing	27
3.2	Convergence Field	31
3.3	Shear Field	32
3.4	Lensing Estimation	33

Weak gravitational lensing (WL), also known as cosmic shear, refers to the subtle distortions in the images of distant source caused by the gravitational fields of intervening mass distributions. Unlike strong lensing, which produces noticeable effects such as multiple images or arcs, weak lensing induces small, coherent distortions that require statistical analysis to detect and interpret. For the standard approach to lensing, we refer to [Schneider et al. \(1992\)](#), [Bartelmann & Schneider \(2001\)](#) and [Bartelmann \(2010\)](#).

3.1 Introduction to Weak Gravitational Lensing

3.1.1 Derivation of the Lens Equation

To derive the lens equation, we consider a perturbed FLRW metric, which incorporates gravitational potential perturbations. The metric is expressed as

$$ds^2 = - \left(1 + \frac{2\Phi}{c^2}\right) c^2 dt^2 + a^2(t) \left(1 - \frac{2\Psi}{c^2}\right) [d\chi^2 + f_K^2(\chi) \omega_{ab} dx^a dx^b] \quad (a, b = 2, 3), \quad (3.1)$$

where the angular part of the metric is defined by

$$\omega_{ab} dx^a dx^b := d\theta^2 + \sin^2 \theta d\phi^2. \quad (3.2)$$

In this context, Φ and Ψ represent the scalar gravitational potentials, and $f_K(\chi)$ encodes the spatial curvature as previously defined in Eq. (2.18).

The trajectory of light within this spacetime is governed by the geodesic equation, which is given by

$$\frac{d^2x^\mu}{d\lambda^2} + \Gamma_{\alpha\beta}^\mu \frac{dx^\alpha}{d\lambda} \frac{dx^\beta}{d\lambda} = 0, \quad (3.3)$$

where λ is an affine parameter and $\Gamma_{\alpha\beta}^\mu$ are the Christoffel symbols corresponding to the metric in Equation (3.1).

To facilitate the derivation, we reparametrize the geodesic equation by substituting the affine parameter λ with the comoving radial distance χ . Applying the chain rule, the geodesic equation transforms to

$$\frac{d^2x^\mu}{d\chi^2} + \Gamma_{\alpha\beta}^\mu \frac{dx^\alpha}{d\chi} \frac{dx^\beta}{d\chi} - \frac{d^2\lambda}{d\chi^2} \left(\frac{d\lambda}{d\chi} \right)^{-1} \frac{dx^\mu}{d\chi} = 0. \quad (3.4)$$

Setting $\mu = 1$ (where $x^1 = \chi$) in Equation (3.4) and simplifying, we obtain

$$\frac{d^2x^\mu}{d\chi^2} + (\Gamma_{\alpha\beta}^\mu - \Gamma_{\alpha\beta}^1) \frac{dx^\alpha}{d\chi} \frac{dx^\beta}{d\chi} = 0. \quad (3.5)$$

The evaluation of Equation (3.5) requires the computation of the Christoffel symbols. Additionally, the derivative $c dt/d\chi$ is derived from the null condition

$$g_{\mu\nu} \frac{dx^\mu}{d\chi} \frac{dx^\nu}{d\chi} = 0, \quad (3.6)$$

yielding

$$\frac{c dt}{d\chi} = -a(t) \left[1 - \frac{\Phi}{c^2} - \frac{\Psi}{c^2} + \frac{f_K^2(\chi)}{2} \omega_{ab} \frac{dx^a}{d\chi} \frac{dx^b}{d\chi} \right], \quad (3.7)$$

valid to first order in Φ and second order in $dx^a/d\chi$. Notably, for the evaluation of Equation (3.5), only the zeroth-order term $c dt/d\chi = -a(t)$ is required. However, the inclusion of perturbative terms in Equation (3.7) is essential for subsequent derivations of the lens equation.

Focusing on the angular components ($\mu = a$) of Equation (3.5), we derive the following differential equation:

$$\frac{d^2x^a}{d\chi^2} + 2 \frac{f'_K(\chi)}{f_K(\chi)} \frac{dx^a}{d\chi} + \omega^{ab} \frac{\Phi_b + \Psi_b}{c^2 f_K^2(\chi)} = 0, \quad (3.8)$$

where Φ_b and Ψ_b denote the derivatives of the gravitational potentials with respect to the angular

coordinates x^a . Integrating Equation (3.8) twice with respect to χ , we obtain

$$\begin{aligned} x^a(\chi_s) - x^a(0) &= -\frac{1}{c^2} \int_0^{\chi_s} d\chi' \int_0^{\chi'} d\chi \omega_{ab} [\Phi_b(\chi, \theta(\chi)) + \Psi_b(\chi, \theta(\chi))] \\ &= -\frac{1}{c^2} \int_0^{\chi_s} d\chi \omega_{ab} [\Phi_b(\chi, \theta(\chi)) + \Psi_b(\chi, \theta(\chi))] \int_\chi^{\chi_s} d\chi' \frac{1}{f_K^2(\chi')} \\ &= -\frac{1}{c^2} \int_0^{\chi_s} d\chi \omega_{ab} [\Phi_b(\chi, \theta(\chi)) + \Psi_b(\chi, \theta(\chi))] \frac{f_K(\chi_s - \chi)}{f_K(\chi_s) f_K(\chi)}, \end{aligned} \quad (3.9)$$

where χ_s denotes the comoving radial distance to the source, and $x^a(0)$ is the angular position at the observer's location. Defining $(\nabla_\theta)^a = \omega^{ab} \partial_b$, the angular position of the source galaxy β is related to the observed angular position θ by

$$\theta(\chi_s) = \theta(0) - \frac{1}{c^2} \int_0^{\chi_s} d\chi \nabla_\theta [\Phi(\chi, \theta(\chi)) + \Psi(\chi, \theta(\chi))] \frac{f_K(\chi_s - \chi)}{f_K(\chi_s) f_K(\chi)}. \quad (3.10)$$

Applying the Born approximation (Born, 1926), and assume that $\Phi = \Psi$, we can simplify the lens equation to:

$$\theta(\chi_s) = \theta(0) - \frac{2}{c^2} \int_0^{\chi_s} d\chi \nabla_\theta [\Phi(\chi, \theta(0))] \frac{f_K(\chi_s - \chi)}{f_K(\chi_s) f_K(\chi)}. \quad (3.11)$$

This final expression constitutes the lens equation, encapsulating the deflection of light due to the gravitational potentials Φ and Ψ along the line of sight.

3.1.2 The Jacobian (Lensing) Matrix \mathcal{A}

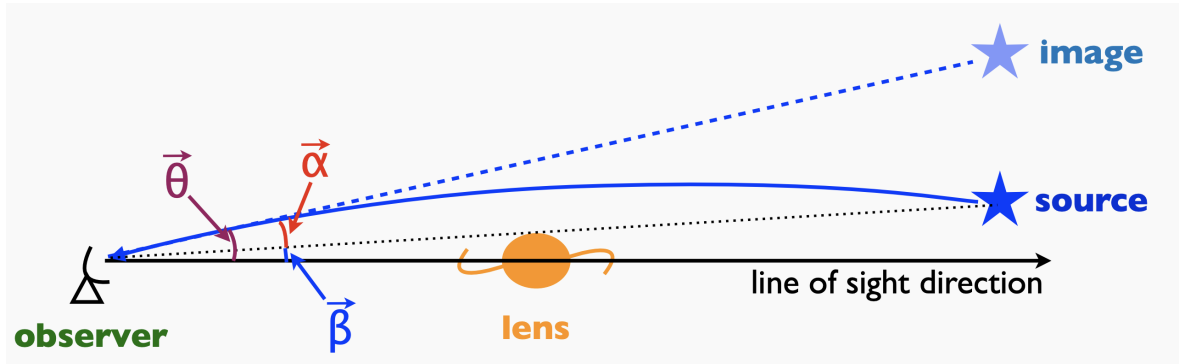


Figure 3.1: Schematic representation of the lensing geometry. The source is located at β , while the observed image is at θ . The deflection angle α is the difference between the observed and true angular positions.

Redefining the notation in Eq. (3.11) and considering the angular position of the source $\beta = \theta(\chi_s)$ and the observed angular position $\theta = \theta(0)$ (see Fig. 3.1), we can express the lens equation as (Bartelmann & Schneider, 2001; Hilbert et al., 2009; Kilbinger, 2015):

$$\beta = \theta - \alpha(\theta), \quad (3.12)$$

where the deflection angle $\alpha(\theta)$ is defined by:

$$\alpha(\theta) = \nabla_\theta \psi(\theta), \quad \psi(\theta) = \frac{2}{c^2} \int_0^{\chi_s} d\chi \frac{f_K(\chi_s - \chi)}{f_K(\chi_s) f_K(\chi)} \Phi(f_K(\chi)\theta, \chi). \quad (3.13)$$

The mapping between the source plane and the image plane can be described by the Jacobian matrix \mathcal{A} , which relates infinitesimal displacements in the source position to displacements in the image position:

$$\mathcal{A} := \frac{\partial \beta}{\partial \theta} = \begin{pmatrix} 1 - \kappa - \gamma_1 & -\gamma_2 \\ -\gamma_2 & 1 - \kappa + \gamma_1 \end{pmatrix} = (1 - \kappa) \begin{pmatrix} 1 & 0 \\ 0 & 1 \end{pmatrix} - |\gamma| \begin{pmatrix} \cos 2\phi & \sin 2\phi \\ \sin 2\phi & -\cos 2\phi \end{pmatrix}, \quad (3.14)$$

where κ is the convergence and $\gamma = \gamma_1 + i\gamma_2 = |\gamma|e^{2i\phi}$ is the shear. The quantities κ and γ will be discussed in detail in the subsequent sections. Figure 3.2 illustrates the effects of gravitational lensing on the shapes of background sources through the lensing matrix \mathcal{A} . The panels demonstrate how the combined effects of convergence and shear components in the Jacobian matrix \mathcal{A} lead to complex distortions of background sources.

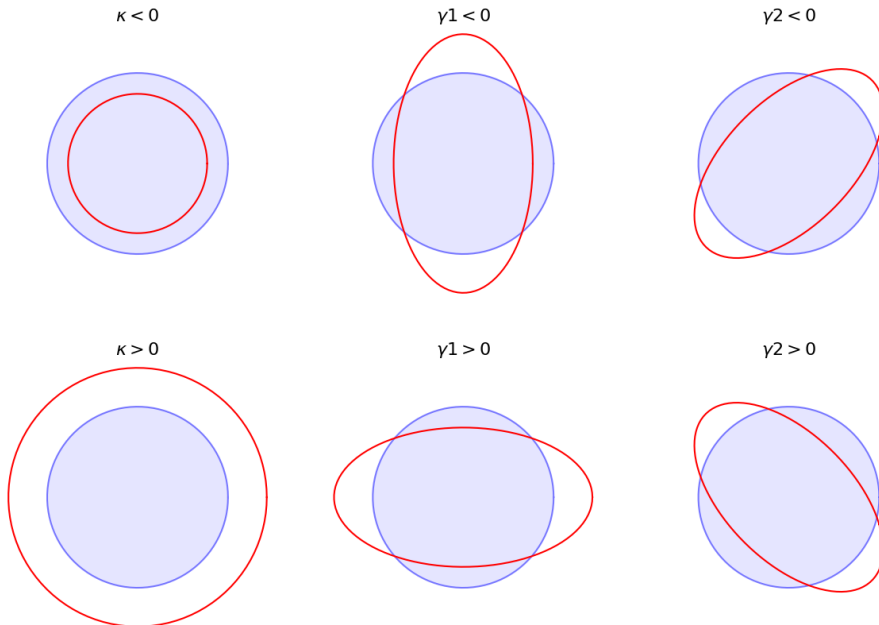


Figure 3.2: Illustration of the distortion of background sources due to gravitational lensing. The left panel depict the effect of the convergence κ and the middle and right panels show the components of the shear $\gamma = \gamma_1 + i\gamma_2$ on circular background sources. Positive and negative values of κ cause isotropic magnification or demagnification, while γ_1 and γ_2 introduce anisotropic distortions, stretching the sources along or at an angle to the principal axes.

3.2 Convergence: Mass Distribution to Lensing

3.2.1 Definition of Convergence in Real and Fourier Space

From the lensing matrix in Eq. (3.14), the convergence κ is defined as:

$$\kappa(\theta) := \frac{1}{2} \left(\frac{\partial^2 \psi}{\partial \theta_1^2} + \frac{\partial^2 \psi}{\partial \theta_2^2} \right) = \frac{1}{2} \nabla_\theta^2 \psi(\theta) \quad (3.15)$$

with θ_1 and θ_2 representing the angular coordinates on the sky. In Fourier space, the convergence field could be expressed as:

$$\tilde{\kappa}(\ell) = \int d^2\theta e^{-i\ell\cdot\theta} \kappa(\theta) = \frac{1}{2} \ell^2 \tilde{\psi}(\ell), \quad (3.16)$$

where $(\tilde{})$ denotes the Fourier transform of the corresponding quantity and $\ell = |\ell|$ is the Fourier counterpart to the angular position θ .

3.2.2 Convergence from Density Contrast and the Lensing Efficiency Function

In a flat universe, the Poisson equation in comoving coordinates is expressed as

$$\begin{aligned} \nabla_{\mathbf{x}}^2 \Phi(\mathbf{x}, \chi) &= 4\pi G a^2(\chi) \bar{\rho}_m(\chi) \delta(\mathbf{x}, \chi) \\ &= 4\pi G a^2(\chi) \left[\frac{3H_0^2 \Omega_m}{8\pi G} a^{-3}(\chi) \right] \delta(\mathbf{x}, \chi) \\ &= \frac{3}{2} \Omega_m H_0^2 a^{-1}(\chi) \delta(\mathbf{x}, \chi), \end{aligned} \quad (3.17)$$

where we utilized Eq. (2.35) and Eq. (2.27). Substituting the expression for Φ from Eq. (3.17) into the lensing potential (Eq. (3.13)) and subsequently into the convergence (Eq. (3.15)), we derive:

$$\begin{aligned} \kappa(\theta) &= \frac{1}{c^2} \int_0^{\chi_s} d\chi \frac{f_K(\chi_s - \chi)}{f_K(\chi_s) f_K(\chi)} \left[\frac{1}{f_K^2(\chi)} \nabla_{\mathbf{x}}^2 \Phi(\mathbf{x}, \chi) \right] \\ &= \int_0^{\chi_s} d\chi \frac{3\Omega_m H_0^2}{2c^2} \frac{f_K(\chi_s - \chi) f_K(\chi)}{f_K(\chi_s)} \frac{a^{-1}(\chi)}{f_K^3(\chi)} \delta(\mathbf{x}, \chi) \\ &= \int_0^{\chi_s} d\chi W(\chi, \chi_s) \delta(\mathbf{x}, \chi), \end{aligned} \quad (3.18)$$

where the lensing efficiency function $W(\chi, \chi_s)$ is defined by:

$$W(\chi, \chi_s) := \frac{3\Omega_m H_0^2}{2c^2} \frac{f_K(\chi) f_K(\chi_s - \chi)}{f_K(\chi_s)} \frac{a^{-1}(\chi)}{f_K^2(\chi)}. \quad (3.19)$$

In a flat universe ($f_K(\chi) = \chi$), this simplifies to:

$$W(\chi, \chi_s) = \frac{3\Omega_m H_0^2}{2c^2} a^{-1}(\chi) \frac{\chi(\chi_s - \chi)}{\chi_s}. \quad (3.20)$$

3.3 Shear: Anisotropic Distortions of Background Sources

The shear γ encapsulates the anisotropic stretching of galaxy images induced by gravitational lensing. Unlike convergence, which affects the size and brightness of images isotropically, shear induces distortions that alter the shapes of background galaxies coherently.

3.3.1 Definition of Shear

[Shear Components and Complex Representation] The shear components γ_1 and γ_2 describe distortions along different axes and are related to the lensing potential ψ by:

$$\gamma_1 := \frac{1}{2} \left(\frac{\partial^2 \psi}{\partial \theta_1^2} - \frac{\partial^2 \psi}{\partial \theta_2^2} \right), \quad \gamma_2 := \frac{\partial^2 \psi}{\partial \theta_1 \partial \theta_2}. \quad (3.21)$$

In Fourier space, the shear field can be expressed as:

$$\tilde{\gamma}_1(\ell) = \frac{1}{2} (\ell_1^2 - \ell_2^2) \tilde{\psi}(\ell) \quad \tilde{\gamma}_2(\ell) = \ell_1 \ell_2 \tilde{\psi}(\ell), \quad (3.22)$$

where $\tilde{\gamma}_1(\ell)$ and $\tilde{\gamma}_2(\ell)$ are the Fourier transforms of $\gamma_1(\theta)$ and $\gamma_2(\theta)$, respectively. Similar as Eq. (3.14), the shear field can be expressed in complex form as:

$$\tilde{\gamma}(\ell) := \tilde{\gamma}_1 + i\tilde{\gamma}_2 = |\tilde{\gamma}(\ell)| e^{2i\phi_\ell}, \quad \tan(2\phi_\ell) = \tilde{\gamma}_2/\tilde{\gamma}_1. \quad (3.23)$$

Therefore, the shear field in Fourier space is directly related to the convergence field combining Eq.(3.16) and Eq.(3.22) (Kaiser & Squires, 1993):

$$\tilde{\kappa}(\ell) = \frac{\ell_1^2 - \ell_2^2 + 2i\ell_1 \ell_2}{\ell^2} \tilde{\gamma}(\ell). \quad (3.24)$$

3.3.2 E-mode and B-mode Decomposition

The shear field can be decomposed into two distinct modes: the **E-mode** (gradient component) and the **B-mode** (curl component). By rotating the complex shear field to align with the principal axes of the shear $\tilde{\gamma}_{EB} = e^{-2i\phi_\ell} \tilde{\gamma}$, we can express the shear field in terms of the E-mode and B-mode components:

$$\begin{pmatrix} \tilde{\gamma}_E \\ \tilde{\gamma}_B \end{pmatrix} := \begin{pmatrix} \cos 2\phi_\ell & \sin 2\phi_\ell \\ -\sin 2\phi_\ell & \cos 2\phi_\ell \end{pmatrix} \begin{pmatrix} \tilde{\gamma}_1 \\ \tilde{\gamma}_2 \end{pmatrix} \quad (3.25)$$

where $\tilde{\gamma}_E$ and $\tilde{\gamma}_B$ are the E-mode and B-mode components of the shear, respectively. The E-mode represents the gradient component of the shear field, while the B-mode describes the curl component.

For standard gravitational lensing by density fluctuations, the B-mode component $\tilde{\gamma}_B(\ell)$ is expected to vanish in the absence of systematics or additional physical effects. This implies that all the shear signal is contained within the E-mode such that:

$$\tilde{\gamma}_E(\ell) = \tilde{\kappa}(\ell), \quad \tilde{\gamma}_B(\ell) = 0. \quad (3.26)$$

3.4 Estimating Lensing Fields from Observables

In the case of cosmic shear, not the convergence but the shear is measured from the observed galaxy shapes. Theoretical predictions of the convergence can be related to the observed shear using the relationship in Eq. (3.24). Here, we introduce a concept of the reduced shear. Furthermore, a convergence field can be estimated from the observed galaxy shapes (Kaiser & Squires, 1993) and can be estimated from magnification (Bartelmann & Schneider, 2001).

3.4.1 Galaxy Ellipticity and Reduced Shear

To quantify the shapes of galaxies, we use the second moments of their surface brightness distributions $I(\theta)$. For each galaxy, the second moments Q_{ab} are defined as (Bartelmann & Schneider, 2001):

$$Q_{ab} := \frac{\int d^2\theta I(\theta)\theta_a\theta_b}{\int d^2\theta I(\theta)}, \quad (3.27)$$

where $\theta = (\theta_1, \theta_2)$ is the angular position relative to the galaxy center. The complex ellipticity ϵ of the galaxy is then defined as:

$$\epsilon := \frac{Q_{11} - Q_{22} + 2iQ_{12}}{Q_{11} + Q_{22}}. \quad (3.28)$$

Gravitational lensing transforms the image of a source galaxy via the Jacobian matrix A (see Eq. (3.14)). Assuming that the surface brightness is conserved during lensing, $I^{(s)}(\beta) = I(\theta)$, the second moments in the source plane $Q_{ab}^{(s)}$ are related to those in the image plane by:

$$Q_{ab}^{(s)} = \frac{\int d^2\beta I^{(s)}(\beta)\beta_a\beta_b}{\int d^2\beta I^{(s)}(\beta)} \approx A_{ac}A_{bd}Q_{cd}, \quad (3.29)$$

where we have approximated the size of the galaxy as sufficiently small so that the lensing distortion is constant across the galaxy image.

By expanding the components of $Q_{ab}^{(s)}$ and performing straightforward calculations (see Schneider et al. 1992 for details), we find that the intrinsic ellipticity $\epsilon^{(s)}$ is related to the observed ellipticity ϵ

through:

$$\epsilon^{(s)} = \frac{(1-\kappa)^2\epsilon - 2(1-\kappa)\gamma + \gamma^2\epsilon^*}{(1-\kappa)^2 + |\gamma|^2 - 2(1-\kappa)\text{Re}[\gamma\epsilon^*]}, \quad (3.30)$$

where ϵ^* denotes the complex conjugate of ϵ , and Re denotes the real part.

Introducing the *reduced shear* $g = \gamma/(1-\kappa)$, the above equation simplifies to ([Schneider & Seitz, 1995](#)):

$$\epsilon^{(s)} = \frac{\epsilon - 2g + g^2\epsilon^*}{1 + |g|^2 - 2\text{Re}[g\epsilon^*]}. \quad (3.31)$$

This relation indicates that weak lensing measurements are sensitive to the reduced shear g rather than the shear γ directly. In the weak lensing regime, where $|\kappa|, |\gamma| \ll 1$, and assuming that the intrinsic ellipticities of galaxies are randomly oriented (i.e., $\langle \epsilon^{(s)} \rangle = 0$), the observed ellipticity becomes an unbiased estimator of the reduced shear:

$$\langle \epsilon \rangle \approx g \approx \gamma. \quad (3.32)$$

However, in the weak-lensing regime, the shear cannot be detected from an individual galaxy due to the dominance of intrinsic shape noise. The typical root mean square (rms) of the intrinsic ellipticity is $\sigma_\epsilon \approx 0.26$ ([Euclid Collaboration et al., 2019](#)), which necessitates averaging over a large number of galaxies to measure the shear signal accurately. The noise for the reduced shear estimator is dominated by Poisson noise, which is given by:

$$\sigma_\gamma = \frac{\sigma_\epsilon}{\sqrt{N}}, \quad (3.33)$$

where N is the number of galaxies used in the shear estimation. It is known that the following transformation of convergence does not change the reduced shear,

$$\kappa' = \lambda\kappa + (1-\lambda), \quad (3.34)$$

where λ is an arbitrary constant. This degree of freedom in the convergence field is known as the mass-sheet degeneracy ([Falco et al., 1985](#)).

3.4.2 Inversion Techniques: From Shear to Convergence

As we have seen in Eq. (3.24), shear and convergence are related through the Fourier transform. Following [Kaiser & Squires \(1993\)](#), the relation between the shear and convergence fields in real space can be expressed as:

$$\gamma(\theta) = \frac{1}{\pi} \int d^2\theta' \mathcal{D}(\theta - \theta') \kappa(\theta'), \quad (3.35)$$

where $\mathcal{D}(\theta)$ is a kernel function defined by:

$$\mathcal{D}(\theta) = -\frac{\theta_1^2 - \theta_2^2 + 2i\theta_1\theta_2}{\theta^4} = -\frac{1}{(\theta_1 - i\theta_2)^2}. \quad (3.36)$$

Therefore, the convolution with the kernel function in Fourier space yields:

$$\tilde{\gamma}(\ell) = \frac{1}{\pi} \tilde{\mathcal{D}}(\ell) \tilde{\kappa}(\ell), \quad (3.37)$$

The Fourier transform of the kernel function, $\tilde{\mathcal{D}}(\ell)$, is given by:

$$\tilde{\mathcal{D}}(\ell) = \pi \frac{\ell_1^2 - \ell_2^2 + 2i\ell_1\ell_2}{\ell^2} \quad (3.38)$$

It is notable that this kernel function and its conjugate satisfies:

$$\tilde{\mathcal{D}}(\ell) \tilde{\mathcal{D}}^*(\ell) = \pi^2 \left(\frac{\ell_1^2 - \ell_2^2 + 2i\ell_1\ell_2}{\ell^2} \right) \left(\frac{\ell_1^2 - \ell_2^2 - 2i\ell_1\ell_2}{\ell^2} \right) = \pi^2. \quad (3.39)$$

Substituting the expression for $\tilde{\mathcal{D}}(\ell)$ into the relation between the shear and convergence fields, we find:

$$\tilde{\kappa}(\ell) = \frac{1}{\pi} \tilde{\gamma}(\ell) \tilde{\mathcal{D}}^*(\ell). \quad (3.40)$$

$$\kappa(\theta) = \kappa_0 + \frac{1}{\pi} \int d^2\theta' \mathcal{D}^*(\theta - \theta') \gamma(\theta'). \quad (3.41)$$

The constant term κ_0 arises from the unknown $\ell = 0$ mode in the Fourier space, which is not constrained by the observed shear field.

Chapter 4

Statistical Measures and Non-Gaussian Signatures in Weak Lensing

Contents

4.1	Two-point Correlation Function	36
4.2	Convergence Power Spectrum	36
4.3	Convergence Bispectrum	39
4.4	Probability Density Functions	41
4.5	Peak and Minimum Counts	42
4.6	Minkowski Functionals	44

4.1 Two-point Correlation Function

4.1.1 Overdensities and the Definition of the 2PCF

4.1.2 2PCF for Biased Tracers

4.2 Convergence Power Spectrum

The matter power spectrum, $P(k)$, is a fundamental quantity in cosmology that characterizes the distribution of dark matter density fluctuations in Fourier space. It is defined as the Fourier transform of the two-point correlation function of the dark matter density field, $\delta(\mathbf{x})$ ([Bartelmann & Schneider, 2001](#)). Mathematically, the matter power spectrum is expressed as:

$$\langle \tilde{\delta}(\mathbf{k}) \tilde{\delta}(\mathbf{k}') \rangle = (2\pi)^3 \delta^{(3)}(\mathbf{k} + \mathbf{k}') P(k), \quad (4.1)$$

where $\tilde{\delta}(\mathbf{k})$ represents the Fourier transform of the density contrast $\delta(\mathbf{x})$, and $\delta^{(3)}$ is the three-dimensional Dirac delta function ensuring statistical isotropy and homogeneity.

In the context of weak gravitational lensing, the matter power spectrum $P(k)$ is not directly observable. Instead, observations yield the angular power spectrum of the convergence field, $C_\ell^{\kappa\kappa}$, which encapsulates the statistical properties of the convergence $\kappa(\theta)$ across the sky (Bartelmann & Schneider, 2001). The convergence power spectrum, $C_\ell^{\kappa\kappa}$, is defined through the relation:

$$\langle \tilde{\kappa}(\ell) \tilde{\kappa}(\ell') \rangle = (2\pi)^2 \delta^{(2)}(\ell + \ell') C_\ell^{\kappa\kappa}, \quad (4.2)$$

where $\tilde{\kappa}(\ell)$ is the Fourier transform of the convergence field $\kappa(\theta)$, and $\delta^{(2)}$ is the two-dimensional Dirac delta function.

4.2.1 Derivation of the Convergence Power Spectrum

The convergence field $\kappa(\theta)$ can be expressed as a weighted projection of the matter density contrast along the line of sight (see Eq. (3.18)):

$$\kappa(\theta) = \int_0^{\chi_s} d\chi W(\chi) \delta_m(\chi\theta, \chi), \quad (4.3)$$

where $W(\chi)$ is the lensing kernel, χ is the comoving radial distance.

Recognizing the Fourier transform of the matter density field $\delta_m(\chi\theta, \chi)$, we write:

$$\delta_m(\chi\theta, \chi) = \int \frac{d^3\mathbf{k}}{(2\pi)^3} \tilde{\delta}(\mathbf{k}) e^{i\mathbf{k}\cdot\mathbf{x}}, \quad (4.4)$$

where $\mathbf{x} = (\chi\theta, \chi)$ is the comoving position vector. Substituting this into the Fourier transform of the convergence field $\tilde{\kappa}(\ell)$, we obtain:

$$\begin{aligned} \tilde{\kappa}(\ell) &= \int_0^{\chi_s} d\chi W(\chi) \int d\theta e^{-i\ell\cdot\theta} \delta_m(\chi\theta, \chi) \\ &= \int_0^{\chi_s} d\chi W(\chi) \int \frac{d^3\mathbf{k}}{(2\pi)^3} \tilde{\delta}(\mathbf{k}) e^{ik_{\parallel}\chi} \int d\theta e^{-i\ell\cdot\theta} e^{i\chi\mathbf{k}_{\perp}\cdot\theta} \\ &= \int_0^{\chi_s} d\chi W(\chi) \int \frac{dk_{\parallel}}{2\pi} \frac{d^2\mathbf{k}_{\perp}}{(2\pi)^2} \tilde{\delta}_m(k_{\parallel}, \mathbf{k}_{\perp}) e^{ik_{\parallel}\chi} \int d\theta e^{-i(\ell-\chi\mathbf{k}_{\perp})\cdot\theta} \\ &= \int_0^{\chi_s} d\chi \frac{W(\chi)}{\chi^2} \int \frac{dk_{\parallel}}{2\pi} \tilde{\delta}_m\left(k_{\parallel}, \frac{\ell}{\chi}\right) e^{ik_{\parallel}\chi}, \end{aligned} \quad (4.5)$$

where \mathbf{k}_{\perp} and k_{\parallel} are the components of \mathbf{k} perpendicular and parallel to the line of sight, respectively.

Next, we evaluate the ensemble average of the Fourier transform of the convergence field. Starting

from the definition, we have:

$$\begin{aligned}\langle \tilde{\kappa}(\ell) \tilde{\kappa}(\ell') \rangle &= \int_0^{\chi_s} d\chi \frac{W(\chi)}{\chi^2} \int_0^{\chi_s} d\chi' \frac{W(\chi')}{\chi'^2} \int \frac{dk_{\parallel}}{2\pi} \int \frac{dk'_{\parallel}}{2\pi} \\ &\quad \times \langle \tilde{\delta}_m \left(k_{\parallel}, \frac{\ell}{\chi} \right) \tilde{\delta}_m \left(k'_{\parallel}, \frac{\ell'}{\chi'} \right) \rangle e^{ik_{\parallel}\chi} e^{ik'_{\parallel}\chi'} \\ &= \int_0^{\chi_s} d\chi \frac{W(\chi)}{\chi^2} \int_0^{\chi_s} d\chi' \frac{W(\chi')}{\chi'^2} \int \frac{dk_{\parallel}}{2\pi} e^{ik_{\parallel}(\chi-\chi')} \\ &\quad \times (2\pi)^2 \delta^{(2)} \left(\frac{\ell}{\chi} + \frac{\ell'}{\chi'} \right) P_m \left(\sqrt{k_{\parallel}^2 + \frac{\ell^2}{\chi^2}} \right)\end{aligned}$$

with $P_m(k)$ being the matter power spectrum.

To proceed, we invoke the Limber approximation (Limber, 1954). This approximation assumes that the dominant contributions arise from modes close to the line of sight, implying $k_{\parallel} \ll \ell/\chi$. Physically, this corresponds to the limit of small angular separations (or large multipole number ℓ) where the geometry of the problem simplifies. In this regime, functions that vary slowly along the line of sight can be factored out of integrals, and the highly oscillatory spherical Bessel functions that would appear in a full-sky calculation can be approximated by their limiting behavior.

Under the Limber approximation, the integral simplifies as:

$$\int \frac{dk_{\parallel}}{2\pi} e^{ik_{\parallel}(\chi-\chi')} P_m \left(\sqrt{k_{\parallel}^2 + \frac{\ell^2}{\chi^2}} \right) \approx P_m \left(\frac{\ell}{\chi} \right) \delta(\chi - \chi'), \quad (4.6)$$

where $P_m(k)$ is evaluated at $k = \ell/\chi$. Substituting this into Eq. (4.6), we obtain:

$$\langle \tilde{\kappa}(\ell) \tilde{\kappa}(\ell') \rangle = (2\pi)^2 \delta^{(2)}(\ell + \ell') \int_0^{\chi_s} d\chi \frac{W^2(\chi)}{\chi^2} P_m \left(\frac{\ell}{\chi}; \chi \right), \quad (4.7)$$

where $P_m \left(\frac{\ell}{\chi}; \chi \right)$ denotes the matter power spectrum evaluated at wavenumber $k = \ell/\chi$ and at the comoving distance χ . Finally, equating this result with the definition of the convergence power spectrum in Eq. (4.2), we derive the expression for $C_{\ell}^{\kappa\kappa}$:

$$C_{\ell}^{\kappa\kappa} = \int_0^{\chi_s} d\chi \frac{W^2(\chi)}{\chi^2} P_m \left(\frac{\ell}{\chi}; \chi \right). \quad (4.8)$$

This relation demonstrates how the observable convergence angular power spectrum $C_{\ell}^{\kappa\kappa}$ is sourced by the underlying matter power spectrum $P_m(k; \chi)$ integrated along the line of sight.

4.2.2 Halofit Model

Based on the halo models (discussed in Sec. 2.7), Halofit model is a widely used prescription to compute the non-linear matter power spectrum $P(k)$ from the linear power spectrum $P_L(k)$ (Smith et al., 2003; Takahashi et al., 2012). In the Halofit regime, the power spectrum consists of two terms:

$$P(k) = P_{1h}(k) + P_{2h}(k), \quad (4.9)$$

where the two-halo term $P_{2h}(k)$ captures the contribution from large-scale linear structures, given by:

$$P_{2h}(k) = P_L(k) \left[\frac{1}{\bar{\rho}} \int dM b(M) n(M) \tilde{\rho}(k, M) \right]^2, \quad (4.10)$$

and one-halo term $P_{1h}(k)$ accounts for the contribution from small-scale non-linear structures, defined as:

$$P_{1h}(k) = \frac{1}{\bar{\rho}^2 (2\pi)^3} \int dM n(M) |\tilde{\rho}(k, M)|^2. \quad (4.11)$$

Here, $\bar{\rho}$ is the mean matter density, $n(M)dM$ is the halo mass function, $b(M)$ is the halo bias, and $\tilde{\rho}(k, M)$ is the Fourier transform of the halo density profile. Those two terms are then approximated into empirical fitting formulae and calibrated against N -body simulations.

The one-halo term resembles a shot noise spectrum on large scales but is progressively reduced on small scales due to the filtering effects of halo profiles and the mass function. Conversely, the two-halo term modifies the relative correlations of halos beyond what is predicted by linear theory and becomes negligible on small scales.

4.3 Convergence Bispectrum

The bispectrum, $B(k)$, serves as the Fourier counterpart to the three-point correlation function and is the lowest-order statistical quantity capable of characterizing non-Gaussianity in the matter distribution (Bernardeau et al., 2002). While the power spectrum effectively captures Gaussian fluctuations through two-point statistics, the bispectrum provides deeper insights by incorporating three-point correlations, thereby unveiling more complex structures in the cosmic density field (Scoccimarro et al., 1999; Takada & Jain, 2004). In a purely Gaussian scenario, the bispectrum vanishes, whereas any non-zero measurement directly signals skewness and reveals the presence of non-Gaussian features in the matter distribution.

Analogous to the angular power spectrum, the convergence bispectrum can be expressed as the ensemble average of three Fourier-transformed convergence modes, $\tilde{\kappa}$ (Dodelson & Zhang, 2005):

$$\langle \tilde{\kappa}(\mathbf{l}_1) \tilde{\kappa}(\mathbf{l}_2) \tilde{\kappa}(\mathbf{l}_3) \rangle = (2\pi)^2 \delta_D(\mathbf{l}_1 + \mathbf{l}_2 + \mathbf{l}_3) B_{\ell_1 \ell_2 \ell_3}^\kappa, \quad (4.12)$$

Building upon the derivations analogous to Equations (4.5) through (4.7), the convergence bispectrum can be expressed as:

$$B_{\ell_1 \ell_2 \ell_3}^{\kappa} = \int_0^{\chi_s} d\chi \frac{W^3(\chi)}{\chi^4} B_m \left(\frac{\ell_1}{\chi}, \frac{\ell_2}{\chi}, \frac{\ell_3}{\chi}; \chi \right), \quad (4.13)$$

where $B_m(k_1, k_2, k_3, z)$ denotes the matter bispectrum at redshift z , and $W(\chi)$ is the lensing kernel.

The bispectrum depends not only on the magnitudes of the wavevectors but also on the shapes formed by the triplet (k_1, k_2, k_3) , constrained by the condition $k_1 + k_2 + k_3 = 0$. Different triangle configurations (e.g. equilateral, squeezed, isoceles) probe different physical processes and scales in the Universe (Dodelson & Zhang, 2005). For instance, equilateral triangles are sensitive to primordial non-Gaussianity, while squeezed triangles probe the growth of structure and the impact of gravity on large scales.

4.3.1 BiHalofit Model

The BiHalofit model (Takahashi et al., 2020) extends the Halofit prescription to compute the non-linear matter bispectrum $B_m(k_1, k_2, k_3)$ from the linear matter power spectrum $P_L(k)$. The bispectrum is decomposed into one-halo and three-halo terms, given by:

$$B_m(k_1, k_2, k_3) = B_{1h}(k_1, k_2, k_3) + B_{3h}(k_1, k_2, k_3), \quad (4.14)$$

The one-halo term describes the correlation in an individual halo, and the three-halo term captures the correlation between three different halos. Because the two-halo term is subdominant in most of the triangle configurations (except at the squeezed limit; Valageas & Nishimichi 2011), it is neglected in the BiHalofit model.

The one-halo term is given by:

$$B_{1h}(k_1, k_2, k_3) = \int dM \frac{dn(M)}{dM} \left(\frac{M}{\bar{\rho}} \right)^3 u(k_1; M) u(k_2; M) u(k_3; M) \quad (4.15)$$

where $u(k; M)$ is the Fourier transform of the scaled halo density profile $\rho(r; M)/M$. The three-halo term is given by:

$$B_{3h}(k_1, k_2, k_3) = 2 \left[F_2(k_1, k_2) + \frac{I_1^2(k_3)}{2I_1^1(k_3)} \right] I_1^1(k_1) I_1^1(k_2) I_1^1(k_3) P_L(k_1) P_L(k_2) + 2 \text{ perm.} \quad (4.16)$$

with

$$I_1^{\beta}(k) = \int dM \frac{dn(M)}{dM} \frac{M}{\bar{\rho}} b_{\beta}(M) u(k; M) \quad (4.17)$$

and

$$F_2(k_1, k_2) = \frac{5}{7} + \frac{1}{2} \left(\frac{k_1}{k_2} + \frac{k_2}{k_1} \right) \mu_{12} + \frac{2}{7} \mu_{12}^2 \quad (4.18)$$

which is given at the tree level (leading order) in perturbation theory ([Bernardeau et al., 2002](#)).

4.4 Probability Density Functions

The Probability Density Function (PDF) of the convergence field, κ , provides a fundamental statistical characterization of the field's one-point distribution. By encompassing all moments and cumulants, the PDF captures both Gaussian and non-Gaussian features intrinsic to the convergence field. The PDF is defined as:

$$P(\kappa) d\kappa = \text{Prob}(\kappa \leq \kappa' \leq \kappa + d\kappa), \quad (4.19)$$

where Prob denotes the probability that the convergence κ' lies within the interval $[\kappa, \kappa + d\kappa]$.

4.4.1 Smoothing and Normalization Procedures

To effectively suppress noise and small-scale fluctuations, the convergence map $\kappa(\hat{\mathbf{n}})$ is first smoothed with a Gaussian kernel. The smoothed convergence field, $\kappa_{\text{smooth}}(\hat{\mathbf{n}})$, is defined as:

$$\kappa_{\text{smooth}}(\hat{\mathbf{n}}) = \int_{S^2} \kappa(\hat{\mathbf{n}}') W(\hat{\mathbf{n}} - \hat{\mathbf{n}}') d\hat{\mathbf{n}}', \quad (4.20)$$

where $W(\theta)$ is the Gaussian smoothing kernel given by:

$$W(\theta) = \frac{1}{2\pi\sigma_\theta^2} \exp\left(-\frac{\theta^2}{2\sigma_\theta^2}\right), \quad (4.21)$$

with $\theta = \arccos(\hat{\mathbf{n}} \cdot \hat{\mathbf{n}}')$ representing the angular separation between the points $\hat{\mathbf{n}}$ and $\hat{\mathbf{n}}'$ with $\hat{\mathbf{n}}$, the unitary normal vector over the unit sphere S^2 , and σ_θ is the smoothing scale. To standardize the statistical analysis, the smoothed convergence values are normalized by their standard deviation. The normalized smoothed convergence, $\tilde{\kappa}_{\text{smooth},i}$, is defined as:

$$\nu_i = \frac{\kappa_{\text{smooth},i} - \langle \kappa_{\text{smooth}} \rangle}{\sigma_{\text{smooth}}}, \quad (4.22)$$

where:

$$\langle \kappa_{\text{smooth}} \rangle = \frac{1}{N_{\text{pix}}} \sum_{i=1}^{N_{\text{pix}}} \kappa_{\text{smooth},i}, \quad \sigma_{\text{smooth}}^2 = \sigma_{\text{signal}}^2 + \sigma_{\text{noise}}^2. \quad (4.23)$$

Formally, the PDF $P(\nu)$ is defined such that:

$$P(\nu) d\nu = \text{Prob}(\nu \leq \nu' \leq \nu + d\nu), \quad (4.24)$$

4.4.2 Practical Estimation of the Convergence PDF

For a discrete set of normalized convergence measurements $\{\nu_i\}_{i=1}^{N_{\text{pix}}}$ obtained from N_{pix} pixels, the PDF can be represented using the Dirac delta function δ_D :

$$P(\nu) = \frac{1}{N_{\text{pix}}} \sum_{i=1}^{N_{\text{pix}}} \delta_D(\nu - \nu_i). \quad (4.25)$$

This expression effectively constructs the PDF by summing over all pixel values, assigning a weight to each normalized convergence measurement ν_i at its exact value.

In practical applications, however, the Dirac delta function is not computationally feasible. Instead, we approximate the PDF by discretizing the normalized convergence values into bins of finite width $\Delta\nu$. This leads to a binned estimator:

$$P(\nu) \approx \frac{1}{N_{\text{pix}} \Delta\nu} \sum_{i=1}^{N_{\text{pix}}} \Theta\left(|\nu_i - \nu| \leq \frac{\Delta\nu}{2}\right), \quad (4.26)$$

where $\Theta(x)$ is the Heaviside step function. This estimator counts the number of normalized convergence ν_i that fall within each bin centered at ν , normalizing by the total number of pixels and the bin width $\Delta\nu$.

4.4.3 hmpdf Model

The `hmpdf` model ([Thiele et al., 2020](#)) presents a halo-model formalism to compute the weak lensing convergence PDF, and its covariance matrix. The one-point $P(\kappa_a)$ and two-point $P(\kappa_a, \kappa_b; \phi)$ PDFs are separated into one-halo and two-halo terms as:

$$P_{\text{1pt/2pt}} = P_{\text{1pt/2pt}}^{\text{1h}} P_{\text{1pt/2pt}}^{\text{2h}}, \quad (4.27)$$

for exact formulae, see [Thiele et al. \(2020\)](#). Expanding the exponentials to the first order, the p -th order of the one-halo term describes overlaps of p halos along the line of sight. The two-halo term arises from the dependence of halo density on the underlying matter density field.

4.5 Peak and Minimum Counts

Local maxima (peaks) and minima in convergence field correspond to regions of over-densities and under-densities, respectively. Analyzing the statistics of these extrema offers insights into the non-Gaussian features of the matter distribution, providing a powerful tool to constrain cosmological models beyond traditional two-point statistics like the power spectrum ([Jain & Van Waerbeke, 2000](#); [Dietrich & Hartlap, 2010](#)).

The i -th pixel in the normalized convergence map, ν is identified as a peak or a minimum by comparing its value with those of its neighboring pixels. Formally, let $\mathcal{N}(i)$ denote the set of neighboring pixels adjacent to pixel i . The conditions for a pixel to be classified as a peak or a minimum are then defined as:

$$\text{Peak Condition: } \kappa_{\text{smooth},i} > \kappa_{\text{smooth},j} \quad \forall j \in \mathcal{N}(i), \quad (4.28)$$

$$\text{Minimum Condition: } \kappa_{\text{smooth},i} < \kappa_{\text{smooth},j} \quad \forall j \in \mathcal{N}(i). \quad (4.29)$$

These conditions ensure that peaks are local maxima and minima are local minima in the convergence field. Figure 4.1 illustrates the identification of peaks (red circles) and minima (blue circles) in the smoothed convergence map $\kappa_{\text{smooth}}(\hat{\mathbf{n}})$.

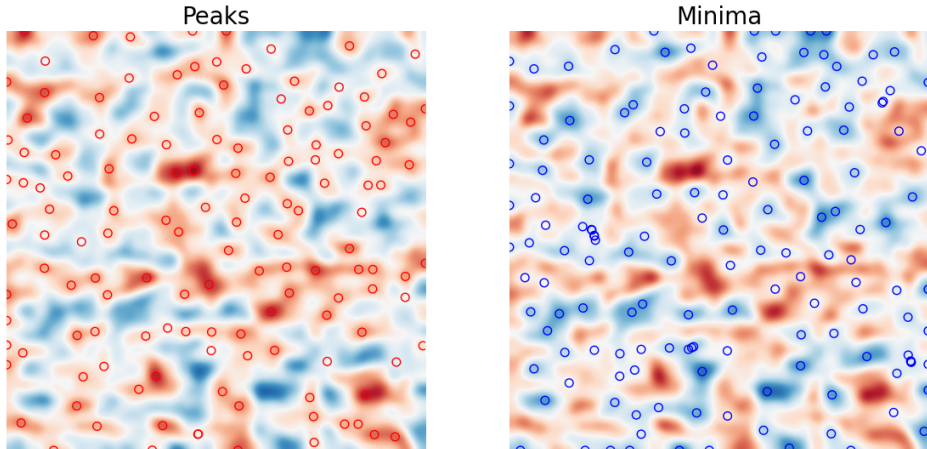


Figure 4.1: Identification of peaks and minima in a smoothed convergence map. The left panel shows the smoothed convergence field $\kappa_{\text{smooth}}(\hat{\mathbf{n}})$ with peaks (red circles) satisfying the peak condition (Equation (4.28)), and the right panel highlights the minima (blue circles) satisfying the minimum condition (Equation (4.29)).

The noise properties of peaks can be analytically described using Gaussian statistics ([Bardeen et al., 1986](#); [Bond & Efstathiou, 1987](#)). Due to the symmetry of a Gaussian field, the expected number density of minima below $-\nu$ is equal to that of peaks above ν , $N_{\text{min}}(-\nu) = N_{\text{peak}}(\nu)$.

Different approaches to analytically predict weak lensing peak counts have been developed over the recent years. One milestone is the model for Gaussian random Field developed by [Bardeen et al. \(1986\)](#), and the extention to the weak lensing field by [Maturi et al. \(2010\)](#). Another popular way to analyze weak lensing data is to compare the measured peak counts to weak lensing maps generated by N-body simulations ([Matsubara, 2010](#); [Kacprzak et al., 2016](#); [Martinet et al., 2018](#); [Zürcher et al., 2021](#)).

4.6 Minkowski Functionals

Minkowski functionals provide an algebraic description of the geometrical properties of a field and are widely used to quantify the morphology of cosmic structures (Mecke et al., 1994). In cosmology, they measure the features of the patterns formed by large-scale structure of the Universe (Schmalzing et al., 1996; Schmalzing & Buchert, 1997).

4.6.1 Definition of Minkowski Functionals

For a two-dimensional normalized convergence field $\nu(\hat{\mathbf{n}})$ with zero mean and variance σ_0^2 , the excursion set $\Sigma(\nu_0)$ at threshold ν_0 is defined as the set of points where the field exceeds a certain threshold value:

$$\Sigma(\nu_0) = \left\{ \hat{\mathbf{n}} \in S^2 \mid \nu(\hat{\mathbf{n}}) > \nu_0 \right\}. \quad (4.30)$$

Figure 4.2 shows $\Sigma(\nu_0)$ for increasing threshold values $\nu_0 = 0.5, 1, 1.5$ and 2 . As the threshold increases, the size and connectivity of the excursion sets diminish, reflecting the decreasing number of high-value regions in the field.

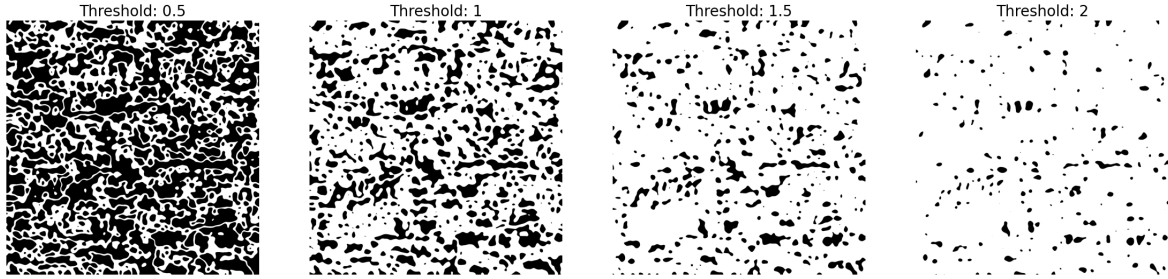


Figure 4.2: Excursion sets $\Sigma(\nu) = \{\kappa > \nu\sigma_0\}$ for increasing thresholds ($\nu = 0.5, 1, 1.5, 2$). Black regions indicate areas where κ exceeds $\nu\sigma_0$, showing reduced size and connectivity as ν increases.

The Minkowski functionals $V_0(\nu_0)$, $V_1(\nu_0)$, and $V_2(\nu_0)$ quantify the morphological properties of these excursion sets (Matsubara, 2010):

$$V_0(\nu_0) = \frac{1}{A} \int_{\Sigma(\nu_0)} da, \quad (4.31)$$

$$V_1(\nu_0) = \frac{1}{4A} \int_{\partial\Sigma(\nu_0)} dl, \quad (4.32)$$

$$V_2(\nu_0) = \frac{1}{2\pi A} \int_{\partial\Sigma(\nu_0)} \mathcal{K} dl, \quad (4.33)$$

where A is the total area, da and dl are area and length elements, and \mathcal{K} is the geodesic curvature of the boundary $\partial\Sigma(\nu)$. Specifically: $V_0(\nu)$ measures the area fraction of the excursion set, $V_1(\nu)$ measures half the boundary length per unit area, and $V_2(\nu)$ quantifies the Euler characteristic per unit area.

For a pixelized map with ν_{pix} pixels, the continuous integrals in Equations (4.31)–(4.33) are approximated by discrete sums (Kratochvil et al., 2012):

$$V_0(\nu_0) \approx \frac{1}{N_{\text{pix}}} \sum_{i=1}^{N_{\text{pix}}} \Theta(\nu_i - \nu_0), \quad (4.34)$$

$$V_1(\nu_0) \approx \frac{1}{4N_{\text{pix}}} \sum_{i=1}^{N_{\text{pix}}} \sum_{j \in \mathcal{N}(i)} |\Theta(\nu_i - \nu_0) - \Theta(\nu_j - \nu_0)|, \quad (4.35)$$

$$V_2(\nu_0) \approx \frac{1}{2\pi N_{\text{pix}}} \sum_{i=1}^{N_{\text{pix}}} \delta_D(\nu_i - \nu_0) \left(\frac{\nu_{,xx}\nu_{,yy} - \nu_{,xy}^2}{\nu_{,x}^2 + \nu_{,y}^2} \right), \quad (4.36)$$

where Θ is the Heaviside function, δ_D the Dirac delta function, $\mathcal{N}(i)$ the neighboring pixels of i , and derivatives are estimated via finite differences.

4.6.2 Analytical Expressions in Gaussian Random Fields

For a two-dimensional GRF $\kappa(\hat{\mathbf{n}})$ with zero mean and unit variance (after normalization), the Minkowski functionals are (Matsubara, 2010):

$$V_0(\nu) = \frac{1}{2} \operatorname{erf} \left(\frac{\nu}{\sqrt{2}} \right), \quad (4.37)$$

$$V_1(\nu) = \frac{\sigma_1}{8\sqrt{2}\sigma_0} e^{-\nu^2/2}, \quad (4.38)$$

$$V_2(\nu) = \frac{\sigma_1^2}{2\pi\sigma_0^3} \nu e^{-\nu^2/2}, \quad (4.39)$$

where erf is the error function, and $\sigma_1^2 = \langle |\nabla \nu|^2 \rangle = \langle \kappa_{,x}^2 + \kappa_{,y}^2 \rangle$. These expressions provide a Gaussian benchmark for identifying non-Gaussian features in the data.

Chapter 5

Estimation of Covariance Matrix for Weak Lensing Statistics

Contents

5.1	The Role of the Covariance Matrix in Parameter Inference	47
5.2	Covariance of the Matter Power Spectrum	48
5.3	Covariance of the Angular Convergence Power Spectrum	50
5.4	Covariance of Higher-Order Weak Lensing Statistics	51

The covariance matrix encapsulates the uncertainties and correlations between different measurements. It plays a critical role in parameter estimation techniques, including maximum likelihood analyses and Bayesian inference, and is foundational in forecasting the capabilities of future surveys through the Fisher information matrix.

The covariance matrix between two observables \mathcal{O}_i and \mathcal{O}_j is defined as:

$$\text{Cov}(\mathcal{O}_i, \mathcal{O}_j) = \langle (\mathcal{O}_i - \langle \mathcal{O}_i \rangle)(\mathcal{O}_j - \langle \mathcal{O}_j \rangle) \rangle, \quad (5.1)$$

where $\langle \cdot \rangle$ denotes the ensemble average over multiple realizations. For an unbiased estimator, the covariance matrix is given by:

$$\text{Cov}(\mathcal{O}_i, \mathcal{O}_j) = \frac{1}{N_{\text{sim}} - 1} \sum_{n=1}^{N_{\text{sim}}} (\mathcal{O}_i^{(n)} - \langle \mathcal{O}_i \rangle)(\mathcal{O}_j^{(n)} - \langle \mathcal{O}_j \rangle), \quad (5.2)$$

where N_{sim} is the number of simulations, and $\mathcal{O}_i^{(n)}$ is the i -th realization of the statistic in the n -th simulation.

5.1 The Role of the Covariance Matrix in Parameter Inference

The study of the covariance matrix is essential for Fisher information analyses, but we will defer a comprehensive discussion to future work. Nonetheless, it is instructive to briefly discuss the importance of the covariance matrix in the context of weak lensing statistics ([Takada & Jain, 2004](#); [Kilbinger & Schneider, 2005](#)). In particular, the covariance matrix serves as a fundamental ingredient in quantifying the uncertainties, correlations, and overall statistical properties of the data.

5.1.1 Likelihood Functions and the Gaussian Approximation

In cosmology, as in many areas of science, we want to determine the values of underlying model parameters \mathbf{p} that best describe the data \mathbf{d} . This process is typically done within a Bayesian framework:

$$P(\mathbf{p}|\mathbf{d}) = \frac{\mathcal{L}(\mathbf{d}|\mathbf{p})\pi(\mathbf{p})}{\epsilon(\mathbf{d})}, \quad (5.3)$$

where $P(\mathbf{p}|\mathbf{d})$ is the posterior distribution, $\pi(\mathbf{p})$ is the prior distribution of the parameters, and $\epsilon(\mathbf{d})$ is the evidence, which normalizes the posterior distribution:

$$\epsilon(\mathbf{d}) = \int \mathcal{L}(\mathbf{d}|\mathbf{p})\pi(\mathbf{p}) d\mathbf{p}. \quad (5.4)$$

The likelihood function $\mathcal{L}(\mathbf{d}|\mathbf{p})$ quantifies the probability of observing the data \mathbf{d} given the model parameters \mathbf{p} . Suppose we have a set of data points $\mathbf{d} = \{d_1, d_2, \dots, d_N\}$, the joint probability of observing the data is obtained as:

$$\mathcal{L}(\mathbf{d}|\mathbf{p}) = \prod_{i=1}^N \mathcal{L}(d_i|\mathbf{p}), \quad (5.5)$$

For Gaussian-distributed data, it can be simply combine into a multivariate Gaussian distribution, and thus the likelihood function can be expressed as:

$$\ln \mathcal{L}(\mathbf{d}|\mathbf{p}) = -\frac{1}{2}(\mathbf{d} - \mathbf{m}(\mathbf{p}))^\top \mathbf{C}^{-1} (\mathbf{d} - \mathbf{m}(\mathbf{p})) + \text{const}, \quad (5.6)$$

where $\mathbf{m}(\mathbf{p})$ is the model prediction for the data vector \mathbf{d} . The covariance matrix \mathbf{C} quantifies the uncertainties and correlations between different data points.

5.1.2 Fisher Information and Parameter Constraints

Based on the likelihood function, we can construct the Fisher information matrix $\mathcal{F}_{\alpha\beta}$, which quantifies the sensitivity of the likelihood function to changes in the model parameters \mathbf{p} . The Fisher information matrix is defined as:

$$\mathcal{F}_{\alpha\beta} = - \left\langle \frac{\partial^2 \ln \mathcal{L}}{\partial p_\alpha \partial p_\beta} \right\rangle, \quad (5.7)$$

In the case of Gaussian likelihoods, the Fisher information matrix is simplified to:

$$\mathcal{F}_{\alpha\beta} = \frac{1}{2} \text{Tr} \left[\mathbf{C}^{-1} \frac{\partial \mathbf{C}}{\partial p_\alpha} \mathbf{C}^{-1} \frac{\partial \mathbf{C}}{\partial p_\beta} \right] \Big|_{p_\alpha = \mu_\alpha} + \left(\frac{\partial \mu}{\partial p_\alpha} \right)^T \mathbf{C}^{-1} \frac{\partial \mu}{\partial p_\beta}, \quad (5.8)$$

where μ is the mean of the data vector \mathbf{d} . As assumed in most studies, the covariance matrix \mathbf{C} is model independent, so that the Fisher information matrix can be reduced to:

$$\mathcal{F}_{\alpha\beta} = \left(\frac{\partial \mu}{\partial p_\alpha} \right)^T \mathbf{C}^{-1} \frac{\partial \mu}{\partial p_\beta}, \quad (5.9)$$

The Fisher matrix allows us to forecast the expected uncertainties on the parameters via the Cramér-Rao bound (Rao, 1952):

$$\langle (\Delta p_\alpha)^2 \rangle \geq (\mathcal{F}^{-1})_{\alpha\alpha}, \quad (5.10)$$

where Δp_α is the uncertainty on the α -th parameter. Note that this condition is marginalized over all other parameters, p_β ($\beta \neq \alpha$). The correlation coefficient between two parameters p_α and p_β is given by:

$$\rho_{\alpha\beta} = \frac{(\mathcal{F}^{-1})_{\alpha\beta}}{\sqrt{(\mathcal{F}^{-1})_{\alpha\alpha}(\mathcal{F}^{-1})_{\beta\beta}}}. \quad (5.11)$$

Therefore, the prior information $\pi(\mathbf{p})$ together with the likelihood function $\mathcal{L}(\mathbf{d}|\mathbf{p})$ can be used to infer the posterior distribution $P(\mathbf{p}|\mathbf{d})$.

5.2 Covariance of the Matter Power Spectrum

Understanding the covariance matrix of the matter power spectrum $P_m(k)$ is crucial before delving into two-dimensional weak lensing statistics. The covariance matrix for the matter power spectrum is defined as:

$$\text{Cov}(k, k') = \langle \hat{P}_m(k) \hat{P}_m(k') \rangle - \langle \hat{P}_m(k) \rangle \langle \hat{P}_m(k') \rangle, \quad (5.12)$$

where $\hat{P}_m(k)$ is an estimator of the matter power spectrum obtained from a finite volume V . An estimator for the matter power spectrum in a finite survey volume is given by (Feldman et al., 1994):

$$\hat{P}_m(k) = (2\pi)^3 \delta_D(\mathbf{k} + \mathbf{k}') \tilde{\delta}(\mathbf{k}) \tilde{\delta}(-\mathbf{k}) = V_f \int_{V_s(k)} \frac{d^3 \mathbf{k}}{V_s(k)} \tilde{\delta}(\mathbf{k}) \tilde{\delta}(-\mathbf{k}), \quad (5.13)$$

where $V_f = (2\pi)^3/V$ is the volume of a Fourier cell where V is the total survey volume, and $V_s(k) = 4\pi k^2 \Delta k$ is the volume of the shell in Fourier space corresponding to wavenumber k .

To derive the covariance matrix, we substitute the estimator $\hat{P}_m(k)$ into the covariance definition:

$$\text{Cov}(\mathbf{k}, \mathbf{k}') = V_f^2 \left(\langle \tilde{\delta}(\mathbf{k}) \tilde{\delta}(-\mathbf{k}) \tilde{\delta}(\mathbf{k}') \tilde{\delta}(-\mathbf{k}') \rangle - \langle \tilde{\delta}(\mathbf{k}) \tilde{\delta}(-\mathbf{k}) \rangle \langle \tilde{\delta}(\mathbf{k}') \tilde{\delta}(-\mathbf{k}') \rangle \right) \quad (5.14)$$

The four-point correlation function $\langle \tilde{\delta}(\mathbf{k}_1)\tilde{\delta}(\mathbf{k}_2)\tilde{\delta}(\mathbf{k}_3)\tilde{\delta}(\mathbf{k}_4) \rangle$ can be decomposed using Wick's theorem into products of two-point functions (Wick, 1950):

$$\begin{aligned}\langle \tilde{\delta}(\mathbf{k})\tilde{\delta}(-\mathbf{k})\tilde{\delta}(\mathbf{k}')\tilde{\delta}(-\mathbf{k}') \rangle &= \langle \tilde{\delta}(\mathbf{k})\tilde{\delta}(-\mathbf{k}) \rangle \langle \tilde{\delta}(\mathbf{k}')\tilde{\delta}(-\mathbf{k}') \rangle \\ &+ \langle \tilde{\delta}(\mathbf{k})\tilde{\delta}(\mathbf{k}') \rangle \langle \tilde{\delta}(-\mathbf{k})\tilde{\delta}(-\mathbf{k}') \rangle \\ &+ \langle \tilde{\delta}(\mathbf{k})\tilde{\delta}(-\mathbf{k}') \rangle \langle \tilde{\delta}(-\mathbf{k})\tilde{\delta}(\mathbf{k}') \rangle \\ &+ \langle \tilde{\delta}(\mathbf{k})\tilde{\delta}(-\mathbf{k})\tilde{\delta}(\mathbf{k}')\tilde{\delta}(-\mathbf{k}') \rangle_c,\end{aligned}\quad (5.15)$$

where the last term represents the connected (non-Gaussian) part of the four-point function, known as the trispectrum $T(\mathbf{k}, -\mathbf{k}, \mathbf{k}', -\mathbf{k}')$.

Using the properties of the Dirac delta function and assuming statistical isotropy, the covariance matrix simplifies to:

$$\text{Cov}(k, k') = \frac{2P_m(k)^2}{N(k)}\delta_{kk'} + \frac{T(k, k')}{V} \quad (5.16)$$

where $N(k) = V_s(k)/V_f$ is the number of independent modes in the shell at wavenumber k . The first term represents the Gaussian (disconnected) contribution, and the second term accounts for the non-Gaussian (connected) contribution from the trispectrum. The first term indicates the unavoidable cosmic variance because we are only able to measure from only one realization of the Universe.

5.2.1 Shot Noise and Super-Sample Covariance

In practice, we can only observe from discrete tracers, such as galaxies, which introduce shot noise into the power spectrum. The shot noise term can be included in the matter power spectrum as:

$$P_{\text{obs}}(k) = P_m(k) + \frac{1}{\bar{n}}, \quad (5.17)$$

where \bar{n} is the number density of galaxies.

In the presence of a finite survey volume, super-sample covariance arises due to modes larger than the survey size influencing the observed modes (Takada & Hu, 2013). This effect adds an additional term to the covariance matrix:

$$\text{Cov}(k, k') = \frac{2P_m^2(k)}{N(k)}\delta_{kk'} + \frac{1}{V}T(k, k') + \left(\frac{\partial P_m(k)}{\partial \delta_b} \right) \left(\frac{\partial P_m(k')}{\partial \delta_b} \right) \sigma_b^2, \quad (5.18)$$

where δ_b represents the large-scale (background) density fluctuation, and σ_b^2 is its variance:

$$\sigma_b^2 = \int \frac{d^3k}{(2\pi)^3} P_m(k) |\tilde{W}(\mathbf{k})|^2, \quad (5.19)$$

with $\tilde{W}(\mathbf{k})$ being the Fourier transform of the survey window function $W(\mathbf{x})$. The derivatives $\partial P_m(k)/\partial \delta_b$

quantify the response of the power spectrum to changes in the background density and can be related to the concept of the response function or integrated perturbation theory (Li et al., 2014).

5.3 Covariance of the Angular Convergence Power Spectrum

We consider a cosmological survey characterized by a window function $\mathcal{W}(\theta)$ and a total survey area $\Omega_{\mathcal{W}}$, defined as the integral of the window function over the sky (Takada & Hu, 2013):

$$\Omega_{\mathcal{W}} = \int d^2\theta \mathcal{W}(\theta). \quad (5.20)$$

The window function $\mathcal{W}(\theta)$, and its Fourier transform, $\tilde{\mathcal{W}}(\ell)$, accounts for the survey geometry and selection effects. Therefore, we can define the observed convergence field $\kappa_{\mathcal{W}}(\theta)$ as:

$$\kappa_{\mathcal{W}}(\theta) = \mathcal{W}(\theta) \kappa(\theta). \quad (5.21)$$

where $\kappa(\theta)$ is the true convergence field. The Fourier transform of the observed convergence field is given by:

$$\tilde{\kappa}_{\mathcal{W}}(\ell) = \int \frac{d^2\ell'}{(2\pi)^2} \tilde{\mathcal{W}}(\ell') \tilde{\kappa}(\ell - \ell'). \quad (5.22)$$

In the presence of the window function, the estimator for the angular power spectrum C_{ℓ} is given by (Takada & Hu, 2013):

$$\hat{C}_{\ell} = \frac{1}{\Omega_{\mathcal{W}}} \tilde{\kappa}_{\mathcal{W}}(\ell) \tilde{\kappa}_{\mathcal{W}}(-\ell). \quad (5.23)$$

The covariance matrix of the angular power spectrum C_{ℓ} is defined as:

$$\text{Cov}(\ell_1, \ell_2) = \langle \hat{C}_{\ell_1} \hat{C}_{\ell_2} \rangle - \langle \hat{C}_{\ell_1} \rangle \langle \hat{C}_{\ell_2} \rangle, \quad (5.24)$$

which measures the statistical correlation between estimates of C_{ℓ_1} and C_{ℓ_2} .

Substituting the estimator \hat{C}_{ℓ} into the covariance definition and expanding the resulting expression leads to terms involving two-point and four-point correlation functions of the convergence field $\kappa(\theta)$. Specifically, the covariance can be expressed as:

$$\begin{aligned} \text{Cov}(\ell_1, \ell_2) &= \frac{1}{\Omega_{\mathcal{W}}^2} [\langle \tilde{\kappa}_{\mathcal{W}}(\ell_1) \tilde{\kappa}_{\mathcal{W}}(-\ell_1) \tilde{\kappa}_{\mathcal{W}}(\ell_2) \tilde{\kappa}_{\mathcal{W}}(-\ell_2) \rangle - \langle \tilde{\kappa}_{\mathcal{W}}(\ell_1) \tilde{\kappa}_{\mathcal{W}}(-\ell_1) \rangle \langle \tilde{\kappa}_{\mathcal{W}}(\ell_2) \tilde{\kappa}_{\mathcal{W}}(-\ell_2) \rangle] \\ &= \frac{1}{\Omega_{\mathcal{W}}^2} [\langle \tilde{\kappa}(\ell_1) \tilde{\kappa}(-\ell_1) \tilde{\kappa}(\ell_2) \tilde{\kappa}(-\ell_2) \rangle + (\ell_2 \leftrightarrow -\ell_2)] \\ &+ \frac{1}{\Omega_{\mathcal{W}}^2} \langle \tilde{\kappa}(\ell_1) \tilde{\kappa}(-\ell_1) \tilde{\kappa}(\ell_2) \tilde{\kappa}(-\ell_2) \rangle_c \end{aligned} \quad (5.25)$$

By a straightforward calculation, this expression can be simplified to:

$$\begin{aligned}\text{Cov}(\ell_1, \ell_2) &= \frac{1}{\Omega_{\mathcal{W}}^2} [C_{\ell_1}]^2 \left[|\tilde{\mathcal{W}}(\ell_1 + \ell_2)|^2 + |\tilde{\mathcal{W}}(\ell_1 - \ell_2)|^2 \right] \\ &+ \frac{1}{\Omega_{\mathcal{W}}^2} \int \frac{d^2 \ell'}{(2\pi)^2} \mathcal{T}(\ell'_1, -\ell'_1 + \ell', \ell'_2, -\ell'_2 - \ell'),\end{aligned}\quad (5.26)$$

where $\mathcal{T}(\ell_1, -\ell_1, \ell_2, -\ell_2)$ is the trispectrum of the convergence field.

Using the Limber approximation (Limber, 1954), which simplifies the projection of three-dimensional quantities into two dimensions, the covariance matrix can be related to the matter power spectrum.

$$C_\ell = \int d\chi \frac{W^2(\chi)}{\chi^2} P_m \left(\frac{\ell}{\chi}, \chi \right), \quad (5.27)$$

$$\mathcal{T}(\ell_1, -\ell_1, \ell_2, -\ell_2) = \int d\chi \frac{W^4(\chi)}{\chi^6} T_m \left(\frac{\ell_1}{\chi}, -\frac{\ell_1}{\chi}, \frac{\ell_2}{\chi}, -\frac{\ell_2}{\chi} \right), \quad (5.28)$$

Similar to the matter power spectrum, the covariance matrix for the angular power spectrum can be decomposed into:

$$\text{Cov}(\ell_1, \ell_2) = \text{Cov}^G(\ell_1, \ell_2) + \text{Cov}^{\text{cNG}}(\ell_1, \ell_2) + \text{Cov}^{\text{SSC}}(\ell_1, \ell_2), \quad (5.29)$$

where:

$$\text{Cov}^G(\ell_1, \ell_2) = \frac{1}{\Omega_{\mathcal{W}}^2} [C_{\ell_1}]^2 \left[|\tilde{\mathcal{W}}(\ell_1 + \ell_2)|^2 + |\tilde{\mathcal{W}}(\ell_1 - \ell_2)|^2 \right], \quad (5.30)$$

$$\text{Cov}^{\text{cNG}}(\ell_1, \ell_2) = \frac{1}{\Omega_{\mathcal{W}}^2} \int \frac{d^2 \ell'}{(2\pi)^2} \mathcal{T}^{\text{cNG}}(\ell'_1, -\ell'_1 + \ell', \ell'_2, -\ell'_2 - \ell'), \quad (5.31)$$

$$\text{Cov}^{\text{SSC}}(\ell_1, \ell_2) = \frac{1}{\Omega_{\mathcal{W}}^2} \int \frac{d^2 \ell'}{(2\pi)^2} |\tilde{\mathcal{W}}(\ell')|^2 \sigma_{\ell_1, \ell_2}^{\ell'}, \quad (5.32)$$

with:

$$\sigma_{\ell_1, \ell_2}^{\ell'} = \int d\chi \frac{W^4(\chi)}{\chi^6} \left(\frac{\partial P_m \left(\frac{\ell_1}{\chi}, \chi \right)}{\partial \delta_b} \right) \left(\frac{\partial P_m \left(\frac{\ell_2}{\chi}, \chi \right)}{\partial \delta_b} \right) P_m \left(\frac{\ell_1}{\chi}, \chi \right) P_m \left(\frac{\ell_2}{\chi}, \chi \right) P_L \left(\frac{\ell'}{\chi} \right), \quad (5.33)$$

where $P_L(k)$ is the linear matter power spectrum. Notably, the SSC term $\text{Cov}^{\text{SSC}}(\ell_1, \ell_2)$ arises from the large-scale density fluctuations modulating the observed power spectrum within the survey area (Takada & Hu, 2013).

5.4 Covariance of Higher-Order Weak Lensing Statistics

Despite some successes in analytical modeling (Chan et al. 2018; Lacasa et al. 2018; Lacasa & Grain 2019; Uhlemann et al. 2023), computing the covariance matrices for higher-order statistics still need

to rely on simulations. Drawing an analogy with the matter power spectrum, the covariance matrix for higher-order statistics can be expressed as:

$$\text{Cov}(\mathcal{O}_i, \mathcal{O}_j) = \text{Cov}^{\text{noSSC}}(\mathcal{O}_i, \mathcal{O}_j) + \text{Cov}^{\text{SSC}}(\mathcal{O}_i, \mathcal{O}_j), \quad (5.34)$$

A rigorous super-sample covariance for line-of-sight integrated observable \mathcal{O}_i , where $\mathcal{O}_i = \int dV_i \mathfrak{o}_i = \int \chi_i^2 d\chi \mathfrak{o}_i$, is given by (Lacasa & Rosenfeld, 2016):

$$\text{Cov}^{\text{SSC}}(\mathcal{O}_i, \mathcal{O}_j) = \iint dV_i dV_j \left(\frac{\partial \mathfrak{o}_i}{\partial \delta_b} \right) \left(\frac{\partial \mathfrak{o}_j}{\partial \delta_b} \right) \sigma_b^2, \quad (5.35)$$

In most cases, the accurate estimation of such covariance matrices still necessitates averaging over numerous realizations of N-body simulations. These simulations capture the relevant mode-coupling and environmental dependencies that are difficult to model analytically, ensuring that the resulting covariance matrices are both realistic and robust. This approach is exactly what we will adopt in this study to quantify the uncertainties due to super-sample covariance in higher-order statistics.

Chapter 6

Numerical Simulations for Large Scale Structure and Weak Lensing

Contents

6.1	Introduction to Numerical Simulations in Cosmology	53
6.2	Initial Condition Generation	54
6.3	N-Body Simulation Methods	56
6.4	Computational Tools and Optimization Techniques	59
6.5	Advanced Codes and Methods: FASTPM	62
6.6	Generating Weak Lensing Maps from Simulations	65

6.1 Introduction to Numerical Simulations in Cosmology

Numerical simulations are crucial in physics and astronomy for studying complex systems of interacting particles, such as galaxies and the Universe's large-scale structure, where analytical solutions are often impractical due to complexity and nonlinearity (Hockney & Eastwood, 1981; Efstathiou et al., 1985; Springel et al., 2005; Springel, 2005). This section provides an overview of N -body simulations commonly used in cosmology.

6.1.1 Dark Matter-Only vs. Hydrodynamical Simulations

In cosmology and astrophysics, simulation can be grouped into two main categories: dark matter-only simulations and hydrodynamical simulations.

Dark matter simulations are used to study the large-scale structure of the universe, the formation of dark matter halos, and the evolution of dark matter particles under the influence of gravity. Since dark matter is effectively collisionless and interacts primarily through gravity, it can be modeled as a collection of particles that evolve under the influence of gravitational forces (Efstathiou et al., 1985).

Hydrodynamical simulations, on the other hand, include the effects of gas dynamics, star formation, and feedback processes from supernovae and active galactic nuclei (AGN) (Hernquist & Katz, 1989; Springel et al., 2005; Springel, 2005). These simulations are more computationally expensive and require additional physics beyond gravity, such as hydrodynamics, radiative transfer, and chemistry.

6.1.2 Historical Evolution and Growth in Particle Number

Since the 1980s, numerical cosmology has developed algorithms to mitigate the computational challenges posed by long-range gravitational interactions by reducing global communication across the computational domain. Key algorithms include mesh-based methods, tree codes, and multipole expansions (Hockney & Eastwood, 1981). Figure 6.1 displays the number of particles used in selected N -body simulations employing these techniques. Symbols and colors indicate the gravitational solvers: particle-particle-particle-mesh (P^3M) and adaptive P^3M (AP^3M); parallel or vectorized P^3M ; Tree codes; TreePM; and particle-mesh methods with adaptive mesh refinement (PM AMR).

Advancements in algorithms and software optimization have increased the number of particles in cosmological simulations beyond what direct summation methods allow. Since 1990, gravity-only simulations have exhibited a super-exponential growth trend, indicated by the quadratic regression in Figure 6.1, reflecting significant methodological innovations beyond hardware improvements (Leclercq, 2020).

6.2 Initial Condition Generation

As we have seen in Section 2.4, the primordial power spectrum $P(k)$ is a key ingredient in generating initial conditions for cosmological simulations. Based on the linear power spectrum, we will review the process of generating initial conditions for N -body simulations.

6.2.1 Initial Density Field

To generate the initial density field for the simulations, we express the density contrast $\delta(\mathbf{x})$ in terms of its Fourier components:

$$\delta(\mathbf{x}) = \int \frac{d^3k}{(2\pi)^3} \tilde{\delta}(\mathbf{k}) e^{i\mathbf{k}\cdot\mathbf{x}}. \quad (6.1)$$

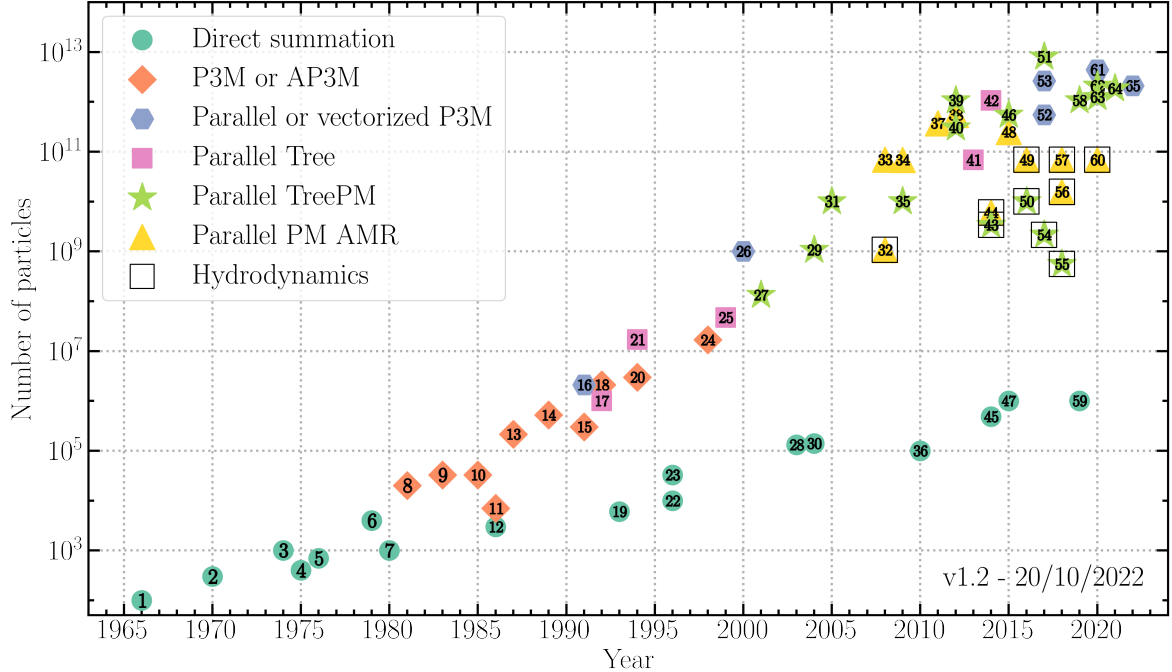


Figure 6.1: Evolution of the number of particles used in N -body simulations as a function of the year of publication (Leclercq, 2020). The symbols and colors indicate the gravitational solver employed: P^3M and adaptive P^3M (AP^3M); parallel or vectorized P^3M ; Tree codes; TreePM; and particle-mesh methods with adaptive mesh refinement (PM AMR). Hydrodynamic simulations are represented by black squares.

Assuming a Gaussian random field, each Fourier mode $\tilde{\delta}(\mathbf{k})$ is a complex Gaussian random variable with zero mean and variance $P(k)$:

$$\tilde{\delta}(\mathbf{k}) = A(\mathbf{k}) + iB(\mathbf{k}), \quad (6.2)$$

$$\langle A(\mathbf{k}) \rangle = \langle B(\mathbf{k}) \rangle = 0, \quad (6.3)$$

$$\langle A(\mathbf{k})A(\mathbf{k}') \rangle = \langle B(\mathbf{k})B(\mathbf{k}') \rangle = \frac{1}{2}P(k)\delta_D(\mathbf{k} - \mathbf{k}'), \quad (6.4)$$

$$\langle A(\mathbf{k})B(\mathbf{k}') \rangle = 0, \quad (6.5)$$

where $A(\mathbf{k})$ and $B(\mathbf{k})$ are real Gaussian random variables, and δ_D is the Dirac delta function.

6.2.2 Initial Displacement Field

The initial displacement field $\Psi(\mathbf{q})$ relates the Lagrangian coordinates \mathbf{q} to the Eulerian coordinates \mathbf{x} :

$$\mathbf{x}(\mathbf{q}) = \mathbf{q} + \Psi(\mathbf{q}). \quad (6.6)$$

The displacement field is proportional to the gradient of the gravitational potential $\Phi(\mathbf{q})$:

$$\Psi(\mathbf{q}) = -\nabla\Phi(\mathbf{q}), \quad (6.7)$$

where the potential satisfies Poisson's equation:

$$\nabla^2 \Phi(\mathbf{q}) = \delta(\mathbf{q}). \quad (6.8)$$

The first order solution to the displacement field is given by the Zel'dovich approximation ([Zel'dovich, 1970](#)):

$$-k^2 \tilde{\Phi}(\mathbf{k}) = \tilde{\delta}(\mathbf{k}), \quad (6.9)$$

$$\tilde{\Psi}(\mathbf{k}) = i\mathbf{k}\tilde{\Phi}(\mathbf{k}) = i\mathbf{k} \frac{\tilde{\delta}(\mathbf{k})}{k^2}, \quad (6.10)$$

$$\Psi(\mathbf{q}) = \int \frac{d^3 k}{(2\pi)^3} i\mathbf{k} \frac{\tilde{\delta}(\mathbf{k})}{k^2} e^{i\mathbf{k}\cdot\mathbf{q}}. \quad (6.11)$$

6.2.3 Initial Velocities

The initial velocities of particles are derived from the time derivative of the displacement field. The velocities are given by ([Efstathiou et al., 1985](#)):

$$\mathbf{v}(\mathbf{q}) = aHf(a)\Psi(\mathbf{q}), \quad (6.12)$$

$$\tilde{\mathbf{v}}(\mathbf{k}) = aHf(a)\tilde{\Psi}(\mathbf{k}) = aHf(a)i\mathbf{k} \frac{\tilde{\delta}(\mathbf{k})}{k^2}, \quad (6.13)$$

$$\mathbf{v}(\mathbf{q}) = iaHf(a) \int \frac{d^3 k}{(2\pi)^3} \frac{\mathbf{k}}{k^2} \tilde{\delta}(\mathbf{k}) e^{i\mathbf{k}\cdot\mathbf{q}}, \quad (6.14)$$

where a is the scale factor, H is the Hubble parameter, and $f(a)$ is the growth rate defined as:

$$f(a) = \frac{d \ln D}{d \ln a}, \quad (6.15)$$

6.3 N-Body Simulation Methods: An Overview

We outline the fundamental concepts and algorithms used in N -body simulations, including direct summation, particle-mesh methods, particle-particle particle-mesh (P3M) methods, and tree-particle-mesh (Tree-PM) methods.

Table 6.1 summarizes the key features of these methods, including computational complexity and example objectives they are best suited for.

6.3.1 Direct Summation

Direct Summation calculates gravitational forces between all particle pairs directly, scaling as $\mathcal{O}(N^2)$ and becoming computationally intensive for large N . Therefore, direct summation is typically used for small systems like globular clusters, where accuracy is paramount ([Wang et al., 2015; Panamarev](#)

Method	Complexity	Objective	Key Features
Direct Summation	$\mathcal{O}(N^2)$	Globular Clusters	Accurate, computationally intensive
PM	$\mathcal{O}(N + M \log M)$	Large-Scale Structure	Fast, smooths small-scale forces
P3M	$\mathcal{O}(N \log N)$	Large-Scale Structure	Combines direct summation and PM
Tree-PM	$\mathcal{O}(N \log N)$	Large-Scale Structure	Tree algorithm for short-range forces

Table 6.1: Comparison of N -body simulation methods

et al., 2019). Each particle i has position \mathbf{r}_i , velocity \mathbf{v}_i , and mass m_i . At each time step t :

1. Compute Forces:

$$\mathbf{F}_i = G m_i \sum_{\substack{j=1 \\ j \neq i}}^N \frac{m_j (\mathbf{r}_j - \mathbf{r}_i)}{\|\mathbf{r}_j - \mathbf{r}_i\|^3}$$

2. Update Particle States:

$$\mathbf{v}_i(t + \Delta t) = \mathbf{v}_i(t) + \frac{\mathbf{F}_i}{m_i} \Delta t, \quad \mathbf{r}_i(t + \Delta t) = \mathbf{r}_i(t) + \mathbf{v}_i(t + \Delta t) \Delta t$$

3. Advance Time:

$$t \leftarrow t + \Delta t$$

6.3.2 Particle-Mesh (PM) Method

The PM method approximates gravitational forces by mapping particles onto a grid and solving for the gravitational potential, reducing computational cost to $\mathcal{O}(N + M \log M)$, where M is the number of grid points. Combining with Adaptive Mesh Refinement (AMR), PM simulations can achieve high resolution in regions of interest while maintaining efficiency so that it is used in Hydrodynamical simulations recently (Springel et al., 2018; Trebitsch et al., 2021). The main difference between the PM method and direct summation is the grid-based force calculation:

1. Assign Particles to Grid: See Section 6.4.2.

2. Compute Density Field:

$$\rho(\mathbf{x}) = \sum_i m_i W(\mathbf{x} - \mathbf{r}_i) \quad (\text{where } W: \text{Interpolation Kernel})$$

3. Solve Poisson's Equation:

$$\nabla^2 \Phi = 4\pi G \rho$$

4. Compute Force due to Potential:

$$\mathbf{E} = -\nabla \Phi$$

6.3.3 Particle-Particle Particle-Mesh (P³M) Method

The P³M method combines direct summation for short-range forces with the PM approach for long-range interactions, achieving $\mathcal{O}(N \log N)$ complexity while enhancing accuracy for nearby particles. Due to its balance between accuracy and efficiency, the P³M (or the Adaptive P³M ([Couchman, 1991](#))) method is widely used in hydrodynamical simulations ([Couchman et al., 1995](#); [Teyssier, 2002](#)).

Key parameters include mesh size, softening parameter ϵ , and force resolution.

The difference between the P³M method and the PM method lies in the force calculation:

1. Long-Range Forces (PM):

$$\mathbf{F}_{\text{long},i} = m_i \mathbf{E}_{\text{long}}(\mathbf{r}_i)$$

2. Short-Range Forces (Direct Summation):

(a) **Neighbor Search:** Identify particles j within cutoff radius r_{cut} of particle i .

(b) **Force Calculation:**

$$\mathbf{F}_{\text{short},i} = -Gm_i \sum_{j \in \text{neighbors}} \frac{m_j(\mathbf{r}_i - \mathbf{r}_j)}{(\|\mathbf{r}_i - \mathbf{r}_j\|^2 + \epsilon^2)^{3/2}}$$

3. Combine Forces:

$$\mathbf{F}_i = \mathbf{F}_{\text{long},i} + \mathbf{F}_{\text{short},i}$$

6.3.4 Tree-Particle-Mesh (Tree-PM) Method

The Tree-PM method integrates the PM approach for long-range forces with a tree algorithm for short-range interactions, reducing complexity to $\mathcal{O}(N \log N)$ ([Barnes & Hut, 1986](#)). Several popular simulations such as Illustris ([Vogelsberger et al., 2014](#)) and EAGLE ([Schaye et al., 2015](#); [Crain et al., 2015](#); [The EAGLE team, 2017](#)) use the Tree-PM method. Proper tuning of parameters like grid size, softening length ϵ , and opening angle θ_{\max} is essential.

The main updates in the Tree-PM method compared to the P³M method are in the tree construction when calculating short-range forces:

1. Tree Construction:

(a) **Build Spatial Cells:** Partition the simulation volume into spatial cells (e.g., octree) and assign particles to nodes.

(b) **Multipole Moments:** For each node j , calculate mass M_j and center of mass $\mathbf{r}_{\text{cm},j}$.

2. Force Calculation: For each particle i , traverse the tree to compute the short-range gravitational force:

$$\mathbf{F}_{\text{short},i} = -Gm_i \sum_{\text{nodes}} \frac{M_j(\mathbf{r}_i - \mathbf{r}_j)}{(\|\mathbf{r}_i - \mathbf{r}_j\|^2 + \epsilon^2)^{3/2}}$$

using the opening angle criterion:

$$\theta = \frac{l_j}{\|\mathbf{r}_i - \mathbf{r}_j\|} < \theta_{\max}$$

where l_j is the size of node j and θ_{\max} is the maximum allowed opening angle.

6.4 Computational Tools and Optimization Techniques

Efficient computational tools are crucial for large-scale simulations and data analysis in scientific and engineering applications. This section overviews key computational techniques and algorithms used in N -body simulations and large-scale structure studies.

6.4.1 Fast Fourier Transforms (FFT)

The Fast Fourier Transform (FFT) is a highly efficient algorithm for computing the Discrete Fourier Transform (DFT) of a sequence. Given a sequence of N complex numbers $\{x_n\}_{n=0}^{N-1}$, the DFT is defined as:

$$X_k = \sum_{n=0}^{N-1} x_n e^{-2\pi i k n / N}, \quad k = 0, 1, \dots, N-1. \quad (6.16)$$

The naive computation of the DFT requires $\mathcal{O}(N^2)$ operations. The FFT reduces this complexity to $\mathcal{O}(N \log N)$ by exploiting the symmetry and periodicity properties of the exponential kernel. The most common FFT algorithm is the Cooley-Tukey radix-2 FFT ([Cooley & Tukey, 1965](#)), which recursively decomposes the DFT into smaller DFTs of even and odd-indexed elements:

$$X_k = \sum_{n=0}^{N/2-1} x_{2n} e^{-2\pi i k (2n) / N} + \sum_{n=0}^{N/2-1} x_{2n+1} e^{-2\pi i k (2n+1) / N} \quad (6.17)$$

$$= X_k^{\text{even}} + e^{-2\pi i k / N} X_k^{\text{odd}}, \quad (6.18)$$

where X_k^{even} and X_k^{odd} are the DFTs of the even and odd subsequences, respectively.

6.4.2 Mass Assignment Schemes

Mass assignment schemes map particle masses onto a computational grid to compute density fields and gravitational forces, ensuring mass conservation and minimizing aliasing errors. Common schemes include:

- **Nearest Grid Point (NGP):** Each particle is assigned entirely to the nearest grid point.
- **Cloud-In-Cell (CIC):** Mass is linearly interpolated to the nearest $2^3 = 8$ surrounding grid points.

- **Triangular-Shaped Cloud (TSC):** Mass is distributed to the nearest $3^3 = 27$ grid points using a quadratic interpolation function.

In Fourier space, these mass assignment window functions are represented as:

$$W(\mathbf{k}) = \prod_{i=1}^3 W(k_i), \quad (6.19)$$

where

$$W(k_i) = \left[\frac{\sin(\pi k_i / (2k_N))}{\pi k_i / (2k_N)} \right]^p, \quad (6.20)$$

with k_N being the Nyquist wavenumber, k_i the i -th component of the wavevector \mathbf{k} , and $p = 1$ for NGP, $p = 2$ for CIC, and $p = 3$ for TSC (Hockney & Eastwood, 1981; Efstathiou et al., 1985).

Figure 6.2 illustrates the mass assignment process for a particle distribution on a 1D grid using different schemes.

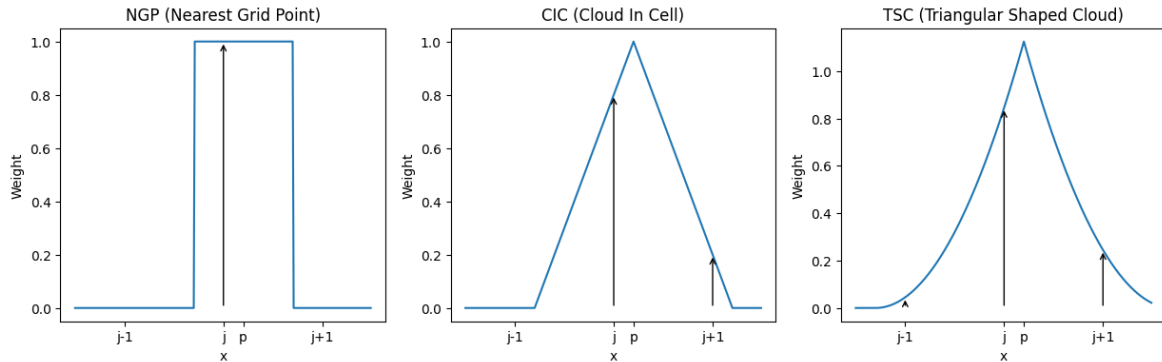


Figure 6.2: Illustration of three mass assignment schemes—Nearest Grid Point (NGP), Cloud-In-Cell (CIC), and Triangular-Shaped Cloud (TSC)—used to map a particle’s mass onto a 1D grid.

6.4.3 Parallelization Techniques

Parallelization accelerates computations in large-scale simulations by leveraging multiple processors or computing nodes. Key strategies include:

- **Domain Decomposition:** The computational domain is partitioned into smaller subdomains, each assigned to a separate processor (Barnes & Hut, 1986).
- **Task Parallelism:** Distributing independent tasks across multiple processors.
- **Data Parallelism:** Performing identical operations concurrently on different data elements, enabling SIMD (Single Instruction, Multiple Data) execution.

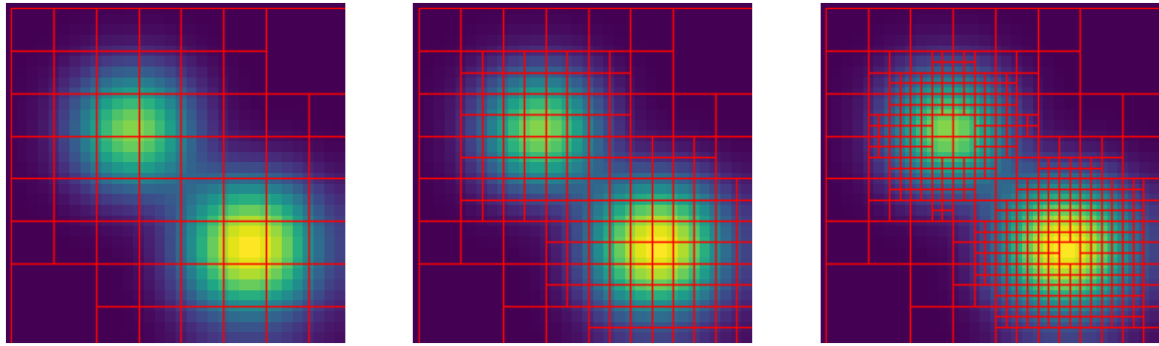


Figure 6.3: Illustration of adaptive mesh refinement (AMR) applied to a 2D image with two Gaussian kernels. The left panel shows the initial coarse grid structure over the image. The middle and right panels demonstrate progressively finer levels of mesh refinement in regions of higher intensity, where the Gaussian kernels are located. The red grid outlines indicate the adaptively refined mesh hierarchy, ensuring higher resolution where needed while maintaining computational efficiency in lower-intensity regions.

6.4.4 Adaptive Mesh Refinement (AMR)

Adaptive Mesh Refinement (AMR) dynamically adjusts grid resolution, refining the mesh where higher accuracy is needed (e.g., regions with high density gradients) and coarsening it elsewhere (Berger & Colella, 1989). This technique is typically used in hydrodynamical simulations to capture complex fluid dynamics and shock fronts accurately. Because N-body simulations with discrete particles do not require continuous field solution and have more efficient methods like Tree-PM, AMR is not commonly used in N-body simulations.

This creates a hierarchy of grids with increasing resolution and optimizes computational resources. Refinement is typically triggered when:

$$|\nabla \phi(\mathbf{x})| > \theta, \quad (6.21)$$

with θ being a predefined threshold.

Figure 6.3 demonstrates the application of Adaptive Mesh Refinement (AMR) to a two-dimensional image containing two Gaussian kernels. Initially, a uniformly coarse grid overlays the entire image (left panel). As the refinement process progresses, the mesh becomes increasingly finer in regions with higher intensity, specifically around the Gaussian kernels (middle and right panels). The red grid lines represent the hierarchy of the refined meshes, enabling higher resolution where it is most needed and optimizing computational resources by keeping a coarser grid in less significant areas.

6.4.5 Tree Construction

Tree-based data structures efficiently organize hierarchical spatial data. The Barnes-Hut algorithm employs an octree to partition space, reducing computational complexity from $\mathcal{O}(N^2)$ to $\mathcal{O}(N \log N)$

by approximating distant particle clusters as single mass points. This approximation is controlled by the opening angle θ :

$$\frac{s}{d} < \theta, \quad (6.22)$$

where s is the node size and d is the distance from the particle to the node's center of mass.

One of the popular algorithms for tree construction is the Barnes-Hut Octree ([Barnes & Hut, 1986](#)), which recursively subdivides the simulation volume into hierarchical grid cells. Figure 6.4 illustrates the Octree decomposition for a 3D volume containing four particles.

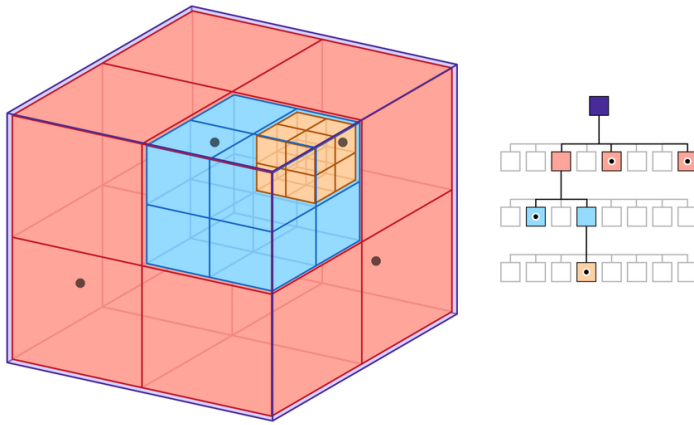


Figure 6.4: Illustration of an Octree decomposition for a 3D volume containing four particles. The left panel showcases the spatial subdivision of the volume into hierarchical grid cells, with color-coding indicating different levels of refinement. The right panel presents the corresponding Octree data structure, highlighting the hierarchical relationships between nodes. Credit by [Powell et al. \(2023\)](#)

Parallel tree construction involves building local trees within each subdomain and integrating them for global computations ([Dubinski, 1996](#)). Efficient parallelization enhances scalability and performance in large-scale simulations.

6.5 Advanced Codes and Methods: FASTPM

FASTPM (Fast Particle Mesh; [Feng et al. 2016](#)) is an advanced N-body simulation code tailored for efficiently modeling the evolution of dark matter and halo structures on cosmological scales. Building upon the foundational PM approach, FASTPM integrates modified kick and drift factors derived from the Zel'dovich Approximation (ZA). This enhancement allows FASTPM to achieve high accuracy in large-scale structure formation while significantly reducing computational overhead. This subsection delineates the core methodology of FASTPM, incorporating the mathematical formalism of its modified kick and drift factors.

6.5.1 Modified Kick and Drift Factors

The cornerstone of FASTPM’s enhanced performance lies in its **modified kick** (K_{FASTPM}) and **drift** (D_{FASTPM}) factors. These factors are meticulously derived from the Zel’dovich Approximation (ZA), a first-order Lagrangian perturbation theory (1LPT), to rectify inaccuracies in large-scale growth inherent in standard PM solvers, especially when operating with a limited number of time steps.

First, the Zel’dovich equation of motion to the first order is defined as:

$$\begin{aligned}\mathbf{x}_{\text{ZA}}(a) &= \mathbf{q} + D(a)\mathbf{s}_1, \\ \mathbf{p}_{\text{ZA}}(a) &= a^3 E(a)g_p(a)\mathbf{s}_1, \\ \mathbf{f}_{\text{ZA}}(a) &= a^2 E(a)g_f(a)\mathbf{s}_1,\end{aligned}\tag{6.23}$$

where $E(a) = \frac{H(a)}{H(a=1)}$ is the dimensionless Hubble parameter, and $g_p(a)$ and $g_f(a)$ are auxiliary factors defined as:

$$g_p(a) = \frac{dD}{da}, G_p(a) = D(a)\tag{6.24}$$

$$g_f(a) = \frac{d(a^3 E g_p)}{da}, G_f(a) = a^3 E g_p(a)\tag{6.25}$$

The ZA equations of motion are reformulated in terms of drift and kick operators by integrating over a time step from a_0 to a_1 and eliminating the ZA displacement \mathbf{s}_1 :

$$\begin{aligned}\Delta\mathbf{x}_{\text{ZA}} &= \mathbf{x}_{\text{ZA}}(a_1) - \mathbf{x}_{\text{ZA}}(a_0) \\ &= [D(a)]_{a_0}^{a_1} \mathbf{s}_1 \\ &= \frac{\mathbf{p}_{\text{ZA}}(a_r)}{a_r^3 E(a_r)} \left(\frac{\Delta G_p}{g_p(a_r)} \right),\end{aligned}\tag{6.26}$$

$$\begin{aligned}\Delta\mathbf{p}_{\text{ZA}} &= \mathbf{p}_{\text{ZA}}(a_1) - \mathbf{p}_{\text{ZA}}(a_0) \\ &= \frac{\mathbf{f}_{\text{ZA}}(a_r)}{a_r^2 E(a_r)} \left(\frac{\Delta G_f}{g_f(a_r)} \right),\end{aligned}\tag{6.27}$$

where $\Delta\mathbf{x}_{\text{ZA}}$ is the change in displacement over the time step, $\Delta\mathbf{p}_{\text{ZA}}$ is the change in momentum over the time step, a_r is a reference scale factor within the time step, $\Delta G_p = G_p(a_1) - G_p(a_0)$, and

$\Delta G_f = G_f(a_1) - G_f(a_0)$. Therefore, the modified kick and drift factors in FASTPM are defined as:

$$\mathcal{D}_{\text{FASTPM}} = \frac{\Delta \mathbf{x}_{\text{ZA}}}{\mathbf{p}_{\text{ZA}}} = \frac{1}{a_r^3 E(a_r)} \left(\frac{\Delta G_p}{g_p(a_r)} \right) \quad (6.28)$$

$$\mathcal{K}_{\text{FASTPM}} = \frac{\Delta \mathbf{p}_{\text{ZA}}}{\mathbf{f}_{\text{ZA}}} = \frac{1}{a_r^2 E(a_r)} \left(\frac{\Delta G_f}{g_f(a_r)} \right) \quad (6.29)$$

These operators ensure the exact integration of the ZA equations of motion, thereby accurately capturing the linear growth of structures within each time step.

6.5.2 Algorithm Steps

The main steps of the FASTPM algorithm follow the standard PM method discussed in Section 6.3.2, with the addition of the modified kick and drift operators to ensure accurate linear growth.

1. **Apply Modified Operators:** Utilize the modified kick (K_{FASTPM}) and drift (D_{FASTPM}) factors to update particle velocities and positions. These factors, derived from the ZA, ensure accurate linear growth:

- (a) **Kick Step:** Update particle velocities by applying the gravitational acceleration scaled by the modified kick factor:

$$\mathbf{v}_i \left(t + \frac{\Delta t}{2} \right) = \mathbf{v}_i(t) + \mathbf{g}_i(t) \cdot K_{\text{FASTPM}} \cdot \Delta t$$

- (b) **Drift Step:** Update particle positions using the updated velocities and the modified drift factor:

$$\mathbf{r}_i(t + \Delta t) = \mathbf{r}_i(t) + \mathbf{v}_i \left(t + \frac{\Delta t}{2} \right) \cdot D_{\text{FASTPM}} \cdot \Delta t$$

- (c) **Second Kick Step:** Apply another kick to update velocities to the full time step:

$$\mathbf{v}_i(t + \Delta t) = \mathbf{v}_i \left(t + \frac{\Delta t}{2} \right) + \mathbf{g}_i(t + \Delta t) \cdot K_{\text{FASTPM}} \cdot \Delta t$$

2. **Update Particle States:** Finalize the update of particle velocities and positions after applying the modified kick and drift operators:

$$\mathbf{v}_i(t + \Delta t) = \mathbf{v}_i \left(t + \frac{\Delta t}{2} \right) + \mathbf{g}_i(t + \Delta t) \cdot K_{\text{FASTPM}} \cdot \Delta t$$

$$\mathbf{r}_i(t + \Delta t) = \mathbf{r}_i(t) + \mathbf{v}_i \left(t + \frac{\Delta t}{2} \right) \cdot D_{\text{FASTPM}} \cdot \Delta t$$

3. **Advance Time:** Increment the simulation time by the time step Δt :

$$t \leftarrow t + \Delta t$$

6.6 Generating Weak Lensing Maps from Simulations

To extract statistics from N-body simulations, it is necessary to generate detailed WL maps by simulating the propagation of a vast number of virtual light rays from source galaxies to the observer. This process involves calculating the distortions and magnifications of the source images caused by the cumulative gravitational deflections from the intervening matter distribution along each line of sight.

6.6.1 Conventional Ray-Tracing Algorithm

Conventional ray-tracing algorithms are fundamental tools for generating WL maps from N-body simulations. These algorithms simplify the complex three-dimensional matter distribution by projecting it onto a series of two-dimensional lens planes. The numerical implementation of the ray-tracing algorithm involves several key computational steps, outlined below ([Das & Bode, 2008](#); [Teyssier et al., 2009](#); [Shirasaki et al., 2015](#)):

1. **Lens Plane Generation:** The first step involves constructing the surface mass density $\Delta_{\Sigma}^j(\theta)$ for each lens plane j . This is achieved by projecting the three-dimensional matter density $\rho(\chi, \chi\theta)$ within a spherical shell bounded by comoving distances χ_j and χ_{j+1} onto a two-dimensional plane:

$$\Delta_{\Sigma}^j(\theta) = \int_{\chi_j}^{\chi_{j+1}} [\rho(\chi, \chi\theta) - \bar{\rho}(\chi)] \chi^2 d\chi, \quad (6.30)$$

where $\bar{\rho}(\chi)$ is the mean matter density at distance χ . The effective comoving distance to the center of the j -th shell, χ^j , is calculated as ([Shirasaki et al., 2015](#)):

$$\chi^j = \frac{\int_{\chi_{\min}}^{\chi_{\max}} \chi^3 d\chi}{\int_{\chi_{\min}}^{\chi_{\max}} \chi^2 d\chi} = \frac{3}{4} \frac{\chi_{\max}^4 - \chi_{\min}^4}{\chi_{\max}^3 - \chi_{\min}^3}, \quad (6.31)$$

where χ_{\min} and χ_{\max} are the minimum and maximum comoving distances of the shell, respectively. The convergence field $\kappa_j(\theta)$ for the j -th lens plane is then computed as:

$$\kappa_j(\theta) = \frac{4\pi G}{c^2} \frac{\Delta_{\Sigma}^j(\theta)}{a_j \chi_j}, \quad (6.32)$$

with a_j being the scale factor and χ_j the comoving distance to the j -th lens plane.

To express $\kappa_j(\theta)$ in terms of the simulation parameters, we consider the following quantities:

- V_{sim} : The simulation volume.
- N_{part} : The total number of particles in the simulation.
- N_{pix} : The number of pixels on each lens plane.
- n_{part}^j : The number of particles in the j -th shell.
- \bar{n}_{part}^j : The mean number of particles per pixel in the j -th shell.

The convergence field is then given by:

$$\kappa_j(\theta) = \frac{3H_0^2\Omega_m}{2c^2a_j\chi_j} \frac{V_{\text{sim}}}{N_{\text{part}}} \frac{N_{\text{pix}}}{4\pi} \left(n_{\text{part}}^j - \bar{n}_{\text{part}}^j \right), \quad (6.33)$$

2. **Potential Calculation:** To facilitate the computation of lensing effects, the lensing potential $\psi^j(\theta)$ for each lens plane is derived from the convergence field $\kappa_j(\theta)$. This is efficiently done using spherical harmonics:

$$\psi_{lm}^j = \frac{2}{l(l+1)} \kappa_{lm}^j \quad \text{for } l \neq 0, \quad (6.34)$$

and $\psi_{lm}^j = 0$ for $l = 0$. Subsequently, the lensing potential in real space is reconstructed, allowing the calculation of the deflection field $\alpha^j(\theta)$ and the optical tidal matrix $U_{ik}^j(\theta)$ through:

$$\alpha_i^j = -\nabla_i \psi^j, \quad U_{ik}^j = \nabla_i \nabla_k \psi^j. \quad (6.35)$$

3. **Deflection Angle Determination:** The deflection field $\alpha^j(\theta)$ and the optical tidal matrix $U_{ik}^j(\theta)$ are interpolated to arbitrary positions on each lens plane. The lensing matrix \mathcal{A}_{ik}^j at each plane is then updated using the recurrence relation:

$$\begin{aligned} \mathcal{A}_{ik}^{j+1} &= \left(1 - \frac{\chi_j}{\chi_{j+1}} \frac{\chi_{j+1} - \chi_{j-1}}{\chi_j - \chi_{j-1}} \right) \mathcal{A}_{ik}^{j-1} + \frac{\chi_j}{\chi_{j+1}} \frac{\chi_{j+1} - \chi_{j-1}}{\chi_j - \chi_{j-1}} \mathcal{A}_{ik}^j \\ &\quad - \frac{\chi_{j+1} - \chi_j}{\chi_{j-1}} U_{im}^j \mathcal{A}_{mk}^j, \end{aligned} \quad (6.36)$$

with the initial conditions:

$$\mathcal{A}_{ik}^1 = \delta_{ik}, \quad \mathcal{A}_{ik}^0 = \delta_{ik}, \quad (6.37)$$

for $j \geq 1$. The closest lens plane to the observer is designated as $j = 0$.

4. **Ray Propagation:** Light rays are propagated from the source galaxies to the observer through the sequence of lens planes. At each plane, the accumulated deflection angles are updated based on the lensing matrix \mathcal{A}_{ik}^j .

5. **Map Assembly:** After propagating all light rays through the lens planes, the convergence $\kappa(\theta)$ and shear $\gamma(\theta)$ fields are compiled into full-sky maps, using Eq. (3.14). These maps are typically represented on the HEALPix grid.

6.6.2 Born-approximated Ray-tracing

The Born approximation offers a simplified approach to weak lensing map generation by assuming that light rays travel along their unperturbed, straight-line paths from the source galaxies to the observer. This approximation neglects the bending of light rays due to gravitational deflections between lens planes, thereby reducing the computational complexity of the ray-tracing process (Schneider, 2006).

While this simplification can lead to faster computations, it introduces certain limitations in accurately capturing multiple deflections and non-linear lensing effects. To overcome these limitations, researchers have developed Post-Born corrections (Cooray & Hu, 2002; Dodelson et al., 2005) that account for the deflection during ray propagation and for the so-called lens-lens coupling, which describes how gravitational lenses at different redshifts can interact to generate rotational modes in the observable fields. It is shown that the Post-Born corrections can impact the higher-order moments or peak statistics of galaxy weak lensing convergence maps (Petri et al., 2017; Fabbian et al., 2019). Figure 6.5 (Petri et al., 2017) illustrates the parameter bias induced by the Born approximation in the convergence power spectrum and moments of the convergence field. The Born approximation is accurate in predicting the convergence power spectrum, but it leads to significant biases in the moments of the convergence field.

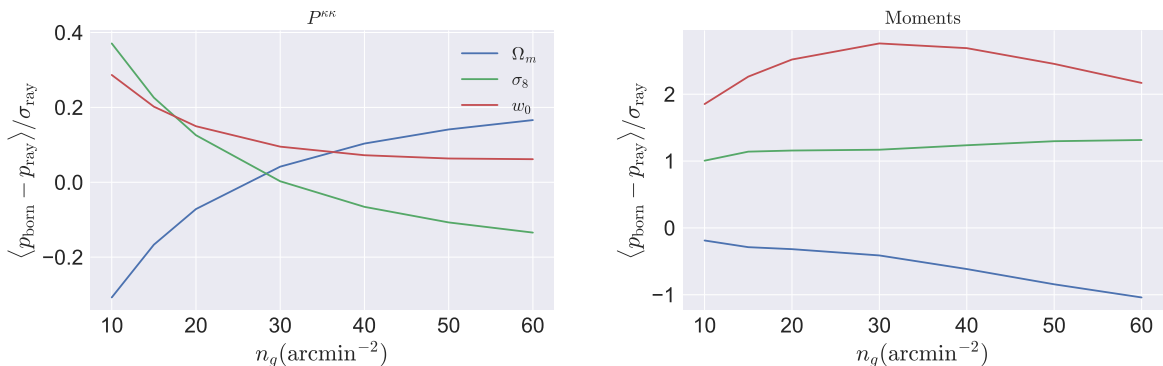


Figure 6.5: Parameter bias induced by the Born approximation in the convergence power spectrum (Left Panel) and moments of the convergence field (Right Panel). While the Born approximation is accurate in predicting the convergence power spectrum, it leads to significant biases in the moments of the convergence field. credit by Petri et al. (2017)

Nonetheless, the Born-approximation remains a valuable tool for generating weak lensing maps in large-scale structure studies (Fosalba et al., 2008; Hilbert et al., 2009; Fosalba et al., 2015a). The Born-approximated ray-tracing algorithm comprises the following key steps:

1. **Lens Plane Calculation:** For each lens plane j , the convergence contribution $\kappa_j(\theta)$ is computed independently, incorporating the lensing efficiency function $W(\chi_j, \chi_s)$, where χ_j is the comoving distance to the j -th lens plane and χ_s is the comoving distance to the source galaxy. The convergence on the j -th plane is given by

$$\kappa_j(\theta) = W(\chi_j, \chi_s) \delta_j(\theta) \Delta \chi_j, \quad (6.38)$$

where $\delta_j(\theta) = n_{\text{part}}^j(\theta)/\bar{n}_{\text{part}}^j - 1$ represents the projected matter density contrast on the j -th lens plane, and $\Delta \chi_j$ is the comoving thickness of the j -th lens plane. The lensing efficiency function, previously defined in Eq. (3.20), is discretized for each lens plane as:

$$W(\chi_j, \chi_s) = \frac{3H_0^2 \Omega_m}{2c^2} \frac{(\chi_s - \chi_j)}{\chi_s} \frac{\chi_j}{a_j}, \quad (6.39)$$

2. **Convergence Field Assembly:** The total convergence field $\kappa(\theta)$ is obtained by summing the contributions from all individual lens planes:

$$\kappa(\theta) = \sum_j \kappa_j(\theta). \quad (6.40)$$

This linear superposition is a direct consequence of the Born approximation, which assumes that each lens plane contributes independently to the total convergence without accounting for the altered path of the light ray due to previous deflections.

Chapter 7

Simulation-Based Methodology for Assessing Higher-Order Weak Lensing Covariance

Contents

7.1	Constructing the BIGBOX and TILED Datasets	69
7.2	Producing Weak Lensing Convergence Maps at Multiple Redshifts	71
7.3	Incorporating Galaxy Shape Noise into Convergence Maps	72
7.4	Patch Selection and Projection	73
7.5	Applying Gaussian Kernels to Convergence Fields	76
7.6	Extracting Weak Lensing Statistics from Convergence Maps	78
7.7	Comparing Covariances from BIGBOX and TILED	80

In this work, we quantified the effect of the super-sample covariance on the covariance matrix of higher-order statistics for a weak lensing survey. To achieve this, we conducted a series of N-body simulations and analyzed the resulting convergence maps. These maps enable the computation of covariance matrices for various statistical measures. Thus, we could investigate the impact of the super-sample covariance on these matrices.

In the following sections, we discuss the methodology used to generate the convergence maps, extract patches for analysis, incorporate noise, apply Gaussian smoothing, and compute the statistical measures. We also outline the process for estimating the covariance matrices and comparing the results between the BIGBOX and TILED simulations.

7.1 Constructing the BIGBOX and TILED Datasets

We employed the publicly available particle-mesh simulation code, FASTPM ([Feng et al., 2016](#)), to generate the simulations used in this study. As discussed in Section [6.5](#), FASTPM was chosen to achieve high accuracy while minimizing computational time.

The two simulations used in this work are **BIGBOX** and **TILED**. For both simulations, we adopted the same cosmological parameters as those used in the IllustrisTNG project ([Nelson et al., 2019](#)). The parameters are listed in Table 7.1.

Parameter	Symbol	Value
Hubble constant	H_0	67.74 [km s ⁻¹ Mpc ⁻¹]
Matter density	Ω_m	0.3089
Baryon density	Ω_b	0.0486
Amplitude of fluctuations	σ_8	0.8159
Spectral index	n_s	0.9667
Sum of neutrino masses	M_ν	0.0 [eV]

Table 7.1: Cosmological parameters used in the N-body simulations.

The BIGBOX simulation, conducted as part of the HalfDome project ([Bayer et al., 2024](#)), uses 6144^3 particles within a box of side length 3750 Mpc/h, employing periodic boundary conditions. The simulation volume is replicated approximately 2.6 times per dimension to cover the redshift range $z = 0$ to $z = 4$, resulting in a total volume of about 10 Gpc/h³. At the maximum redshift considered in this work, $z = 2.5$, the simulation volume is replicated approximately 1.2 times per dimension.

The TILED simulation covers a smaller volume with a side length of $L = 625$ Mpc/h, populated with 1024^3 particles and also employing periodic boundary conditions. This combination of box size and particle number was chosen to match the resolution of the BIGBOX simulation. To cover the same redshift range as the BIGBOX simulation, the TILED box was replicated 10 times along each axis, although 6 replications are sufficient for the range $z = 0$ to $z = 2.5$. Figure 7.1 illustrates the spatial and redshift setup for the BIGBOX and TILED simulations employed in this cosmological study.

Both simulations commenced at an initial redshift of $z = 9$, utilizing an initial linear matter power spectrum at $z = 0$ generated via the CLASS code ([Blas et al., 2011](#)). The simulations were evolved over 60 time steps to reach the present day ($z = 0$). The resulting particle distributions were output in 80 shells spanning scale factors from $a = 0.2$ to $a = 1.0$, with a uniform spacing of $\Delta a = 0.01$. At each scale factor a_i , particles within the shells were projected onto a HEALPix grid ([Górski et al., 2005](#)) with $N_{\text{side}} = 8192$, providing an angular resolution of approximately 0.43 arcminutes, to generate mass maps.

The BIGBOX and TILED simulations were executed on the TACC (Texas Advanced Computing Center) cluster. The BIGBOX simulations required approximately 4 hours per realization, utilizing 2048 nodes, while the TILED simulations were completed in 2 hours per realization using 64 nodes.

In total, we generated 11 realizations of the BIGBOX simulation and 20 realizations of the TILED simulation, each initialized with distinct random seeds. This ensemble of realizations enables us to

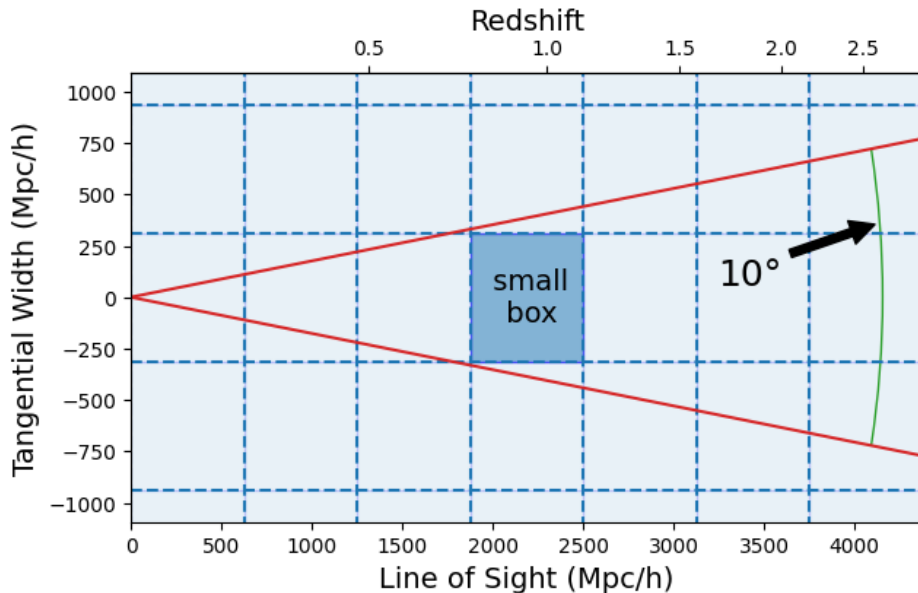


Figure 7.1: Spatial and redshift setup for the BIGBOX and TILED simulations. Dashed blue grids partition the overall simulation volume into smaller, manageable tiling regions, with each tile representing a replication of the TILED simulation. The lower horizontal axis indicates the line-of-sight distance in Mpc/h , while the corresponding redshift values are displayed on the top axis.

robustly sample cosmic variance and ensures that our statistical analyses are not biased by the initial conditions of any single simulation.

It is important to note that the observer is positioned at the corner point shared by 8 replicated boxes in both the TILED and BIGBOX simulations. This placement induces the Box Replication Effect, characterized by a kaleidoscope-like pattern of heavily tiled regions along the line of sight, particularly near the equatorial regions and in directions parallel to the box edges (see Figure 7.2 for $z = 1.5$). These replicated regions can introduce artificial correlations and anisotropies in the mass maps, potentially biasing our statistical measurements. To mitigate this effect, we exclude the most heavily tiled regions from our analysis, ensuring that the Box Replication Effect does not significantly impact our results. A detailed discussion of this phenomenon and its implications is provided in Section 8.5.

7.2 Producing Weak Lensing Convergence Maps at Multiple Redshifts

Since we already have the projected mass map at each scale factor, we calculate the convergence map at each redshift following the discussion in Sections 3.2 and 6.6. As the difference between the TILED and BIGBOX simulations due to the super-sample effect becomes apparent around redshift $z \approx 1$, it is worthwhile to examine the contribution from each redshift to the convergence map.

Figure 7.3 shows the normalized lensing efficiency as a function of comoving distance (in Mpc/h)

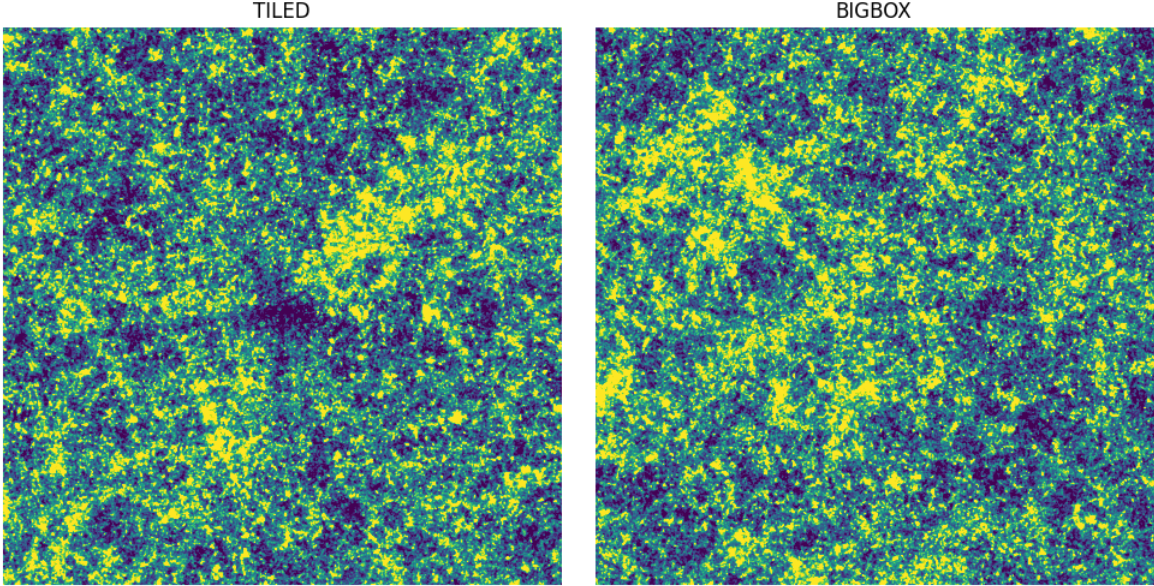


Figure 7.2: Illustration of a 5×5 patch around $(\theta, \phi) = (\pi/2, 0)$ extracted from the TILED and BIGBOX simulations at $z = 1.5$. The TILED simulation displays a distinct kaleidoscope-like pattern caused by box replication, resulting in heavily tiled regions along the line of sight and near the equator. This pattern becomes more pronounced at higher redshifts.

for multiple source redshifts (z). The lensing efficiency curves exhibit distinct peaks at intermediate comoving distances, highlighting the regions where the matter distribution along the line of sight most significantly enhances the gravitational lensing signal

We considered source redshifts $z_s = [0.5, 1.0, 1.5, 2.0, 2.5]$, covering the range of distances relevant for both current and upcoming galaxy surveys. At low redshifts ($z < 1$), both the BIGBOX and TILED simulations are affected by super-sample effects. However, at higher redshifts ($z > 1$), these effects become more pronounced in the BIGBOX simulation. This divergence occurs because, at approximately $z = 1$, the light cone in the TILED simulation begins to extend tangentially across multiple replicated boxes. As a result, no additional super-survey modes arise within the TILED simulation beyond this redshift, effectively mitigating the influence of super-sample covariance.

Figure 7.4 shows the convergence maps generated from both the BIGBOX and TILED simulations for a source redshift of $z_s = 1.5$. These maps are depicted on Healpix grids with $N_{\text{side}} = 8192$, consistent with the methodology described.

7.3 Incorporating Galaxy Shape Noise into Convergence Maps

In actual observations, measurements of the lensing signal are affected by noise arising from the intrinsic shapes of galaxies and inaccuracies in shape measurements. This type of noise, known as shape noise, is a major source of uncertainty, especially on small angular scales. For example, shape noise can differ the number densities by approximately 12% in the HSC shear catalog (See Section

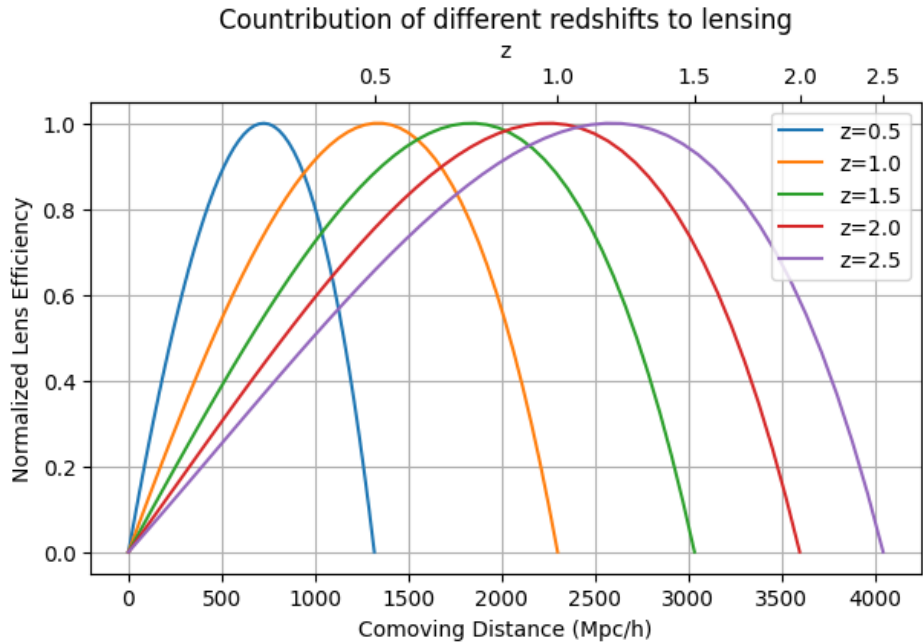


Figure 7.3: Normalized lensing efficiency as a function of comoving distance for multiple source redshifts. The efficiency curves peak at intermediate comoving distances, indicating regions where the matter distribution enhances the gravitational lensing signal.

5.2 of [Mandelbaum et al. 2018a](#)).

We considered four different surveys with varying galaxy number densities, as detailed in Table 1.1. The variance of the shape noise per pixel was calculated using the following expression:

$$\sigma_{\kappa, \text{noise}}^2 = \frac{\sigma_\epsilon^2}{2n_{\text{gal}}A_{\text{pix}}}, \quad (7.1)$$

where σ_ϵ is the intrinsic ellipticity dispersion of galaxies, set to $\sigma_\epsilon = 0.26$ ([Euclid Collaboration et al. 2019](#)), n_{gal} is the galaxy number density per square arcminute, and A_{pix} is the solid angle of a pixel, set to 0.43 arcminutes². Using this calculated variance, we generated a Gaussian random field, $n(\hat{\mathbf{n}})$, and added it to the convergence maps to simulate the observed signal:

$$\kappa_{\text{obs}}(\hat{\mathbf{n}}) = \kappa(\hat{\mathbf{n}}) + n(\hat{\mathbf{n}}). \quad (7.2)$$

7.4 Patch Selection and Projection

To simplify the analysis onto a flat patch, we extracted $10^\circ \times 10^\circ$ patches from the full-sky convergence maps. To maximize the number of uniformly distributed patches without repetition, we employed a Fibonacci grid ([Swinbank & James Purser, 2006; Ferlito et al., 2023](#)) for extracting patches from the full-sky map. The center of each patch was positioned at the vertices of the Fibonacci grid, defined

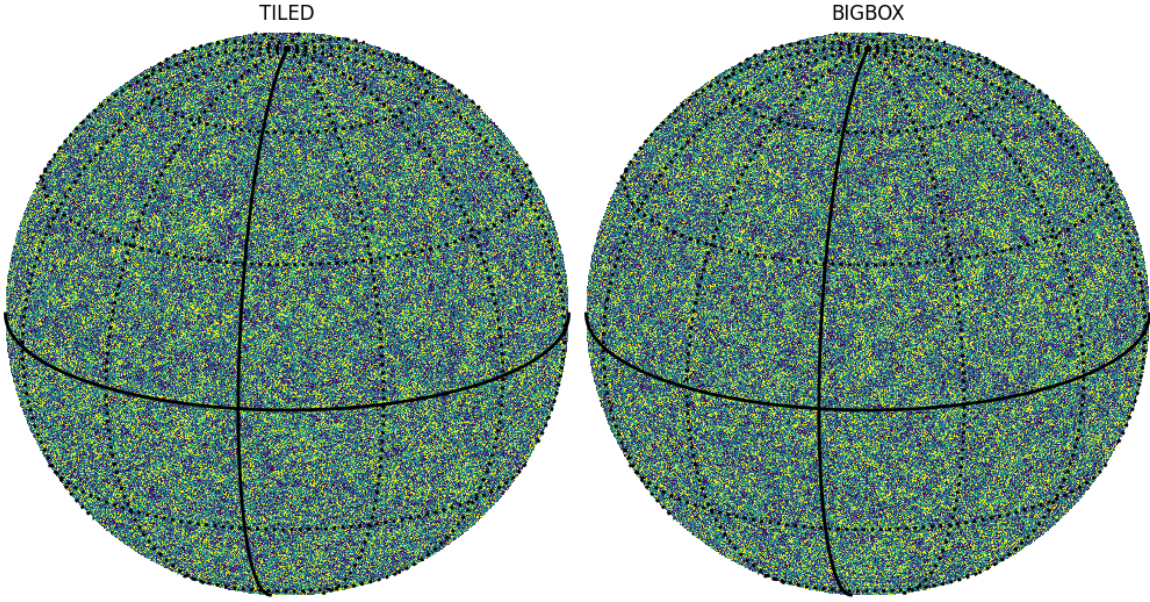


Figure 7.4: Convergence maps from the BIGBOX and TILED simulations for source redshift $z_s = 1.5$. Yellow regions indicate positive convergence, while blue regions represent negative convergence. The maps exhibit similar large-scale structures, highlighting the agreement in the overall distribution of matter.

by golden ratio spirals:

$$\sin \theta_i = \frac{2i}{2N+1}, \quad \phi_i = \frac{2\pi i}{\varphi}, \quad -N \leq i \leq N, \quad -\frac{\pi}{2} \leq \theta_i \leq \frac{\pi}{2}, \quad (7.3)$$

where N is the number of patches and $\varphi = (1 + \sqrt{5})/2$ is the golden ratio. The visualization of the Fibonacci grid is shown in Figure 7.5. Following Ferlito et al. (2023), the maximum number of

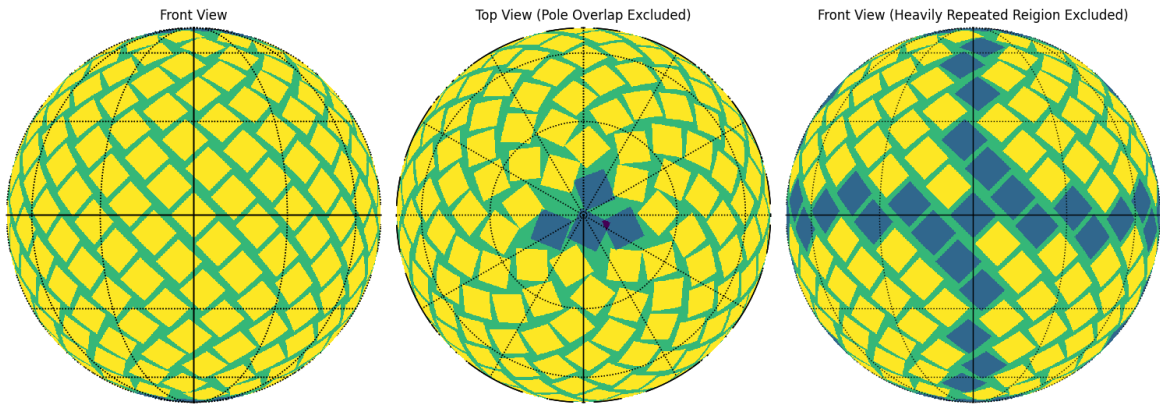


Figure 7.5: Visualization of the Fibonacci grid with $N_{\text{patches}} = 273$, where each patch covers approximately $10^\circ \times 10^\circ$. After optimization and masking, the number of patches is reduced to $N_{\text{patches}} = 194$, effectively covering 47% of the sky. Each panel shows the patch distribution from a front view, top view, and the final front view after masking.

patches can be obtained by aligning the diagonals of square patches with the longitude lines. However, due to programming constraints, we extracted patches with their sides aligned to the latitude lines.

To achieve the desired $10^\circ \times 10^\circ$ shape, we first extracted patches with a larger side length and then rotated and cropped them accordingly.

Before extracting the patches, we optimized the number of patches to be extracted from the full-sky map. The number of patches, denoted N_{patches} , was determined to ensure that individual patches do not overlap, except in regions near the poles, where overlapping patches were subsequently discarded. Each patch on the full-sky map is defined as:

$$\begin{aligned} & (\theta_i - R_{\text{patch}}, \phi_i + R_{\text{patch}} \sin \theta_i), \quad (\theta_i + R_{\text{patch}}, \phi_i + R_{\text{patch}} \sin \theta_i), \\ & (\theta_i - R_{\text{patch}}, \phi_i - R_{\text{patch}} \sin \theta_i), \quad (\theta_i + R_{\text{patch}}, \phi_i - R_{\text{patch}} \sin \theta_i) \end{aligned} \quad (7.4)$$

with $R_{\text{patch}} = 5\sqrt{2}$ deg, the half diagonal length of the patch. The optimization process began with an initial count of $N_{\text{patches}} = 400$ and involved iteratively reducing this number until a configuration was achieved in which patches remained non-overlapping, except for centers located within $2R_{\text{patch}}$ of the poles. Specifically, the thresholds $|\theta_i| \geq 2R_{\text{patch}}$ and $|\phi_i| \leq \pi - 2R_{\text{patch}}$ were applied to ensure that the patches did not include the poles.

After optimization and masking, the number of patches was reduced to $N_{\text{patches}} = 273$, further decreasing to $N_{\text{patches}} = 265$ to effectively cover 64% of the sky. Additionally, patches containing points heavily tiled along the line of sight were excluded to mitigate the severe Box Replication Effect (see Section 8.5 for further details). Consequently, the final number of patches used for analysis was $N_{\text{patches}} = 194$, effectively covering 47% of the sky.

For a Fibonacci grid center characterized by coordinates (θ_i, ϕ_i) , we first employed the `gnomview` function from the `healpy` library (Zonca et al., 2019) to project each spherical patch onto a flat plane using a gnomonic projection. Each patch was then rotated by 45° around its center to align the diagonal of the patch with the longitude lines. Finally, the patch was cropped according to the corresponding vertices to achieve the desired shape. Figure 7.6 illustrates the process of extracting a patch from the full-sky convergence map and the additional steps taken to obtain the final patch.

Each patch is represented by a 2048×2048 grid of pixels, resulting in a pixel size of:

$$\Delta\theta = \frac{10^\circ}{2048} \approx 0.00488^\circ \approx 0.293' \quad \text{per pixel.} \quad (7.5)$$

For each realization, the covariance was computed using 194 patches extracted from the full-sky map of each simulation. This resulted in a total of 2134 patches from the BIGBOX simulation and 3880 patches from the TILED simulation. This ensemble of patches enables us to robustly sample both cosmic variance and shot noise, ensuring that our statistical analyses are sufficient for the power spectrum at $\ell = 5283$ and peak counts in $\kappa \in [-0.06, 0.45]$ (Petri et al., 2016).

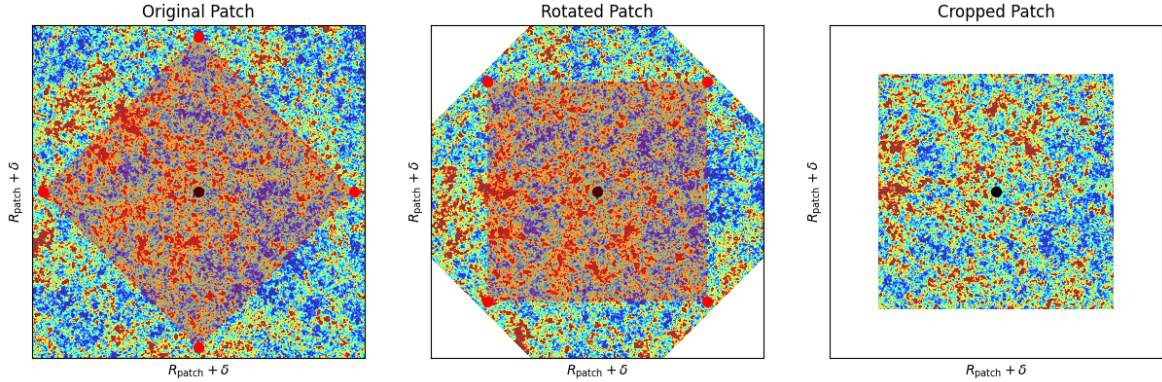


Figure 7.6: Extraction of a patch from the full-sky convergence map using a Fibonacci grid. The patch covers an area of $10^\circ \times 10^\circ$ and is centered at a vertex of the Fibonacci grid. From left to right, the panels show the originally extracted patch, the patch rotated 45° around its center, and the final patch after a second rotation. The red-shaded region represents the final patch used for analysis.

7.5 Applying Gaussian Kernels to Convergence Fields

Shape noise predominantly affects small angular scales. To mitigate this noise and enhance the detection of the underlying lensing signal, we applied Gaussian smoothing to the noisy convergence maps. The Gaussian filter is defined as:

$$W(\theta) = \frac{1}{\pi\theta_G^2} \exp\left(-\frac{\theta^2}{\theta_G^2}\right), \quad (7.6)$$

where θ is the angular distance from the center of the filter, and θ_G is the smoothing scale. For our analysis, we selected $\theta_G = 2'$, $5'$, $8'$, and $10'$.

By convolving the noisy convergence map with the Gaussian filter, we obtained the smoothed convergence map:

$$\kappa_{\text{smoothed}}(\hat{\mathbf{n}}) = \int d\Omega' W(|\hat{\mathbf{n}} - \hat{\mathbf{n}}'|) \kappa_{\text{obs}}(\hat{\mathbf{n}}'). \quad (7.7)$$

Figure 7.7 illustrates the impact of Gaussian smoothing on a noisy convergence map, demonstrating the progressive suppression of small-scale fluctuations. The figure consists of four panels, each corresponding to a different smoothing scale: $\theta_G = 2'$, $5'$, $8'$, and $10'$. As the smoothing scale increases, the Gaussian kernel increasingly attenuates small-scale noise, reducing the amplitude of fluctuations in the map. Although this process naturally diminishes the power spectrum at small angular scales, smoothing scales below $10'$ are sufficient to mitigate shape noise while retaining the non-Gaussian structures of the convergence field.

For the analysis of non-Gaussian statistics, we employ a Gaussian smoothing procedure, after which the statistics are computed from the resulting smoothed convergence maps. The application of a smoothing kernel effectively suppresses small-scale structures, thereby modifying the range of κ values. To avoid the smoothing issues and the complex binning to consider, we normalize κ values

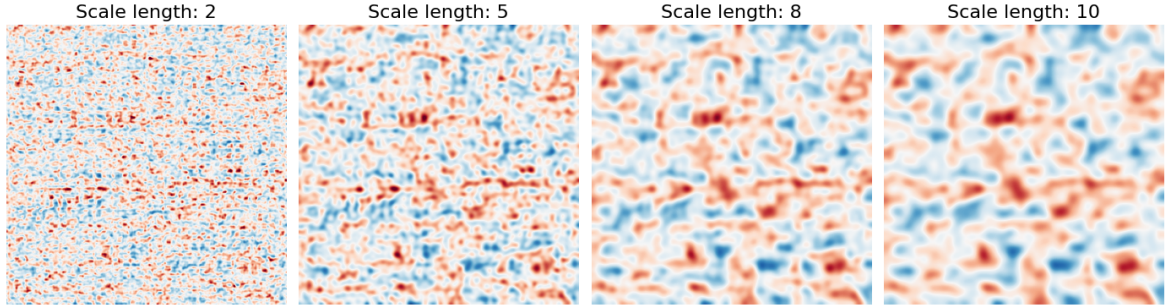


Figure 7.7: Effect of Gaussian smoothing on a noisy convergence map. Each panel shows the result of applying a Gaussian filter with a smoothing scale of $\theta_G = 2'$, $5'$, $8'$, or $10'$. As the smoothing scale increases, small-scale noise is progressively suppressed, making large-scale structures more prominent. This demonstrates how Gaussian smoothing effectively reduces shape noise while preserving the underlying lensing signal.

by the standard deviation of each patch’s convergence map, σ_κ .

Figure 7.8 shows the mean standard deviation of the noiseless convergence maps obtained from both the BIGBOX and TILED simulations. While there is no significant difference between the two simulations, the standard deviation increases with both redshift and smoothing scale. The observed increase with redshift reflects the inclusion of additional shells along the line of sight, leading to greater variability in density contrasts. Similarly, the increase with smoothing scale arises from the smoothing process itself, which suppresses small-scale structures and amplifies the variability of larger-scale fluctuations.

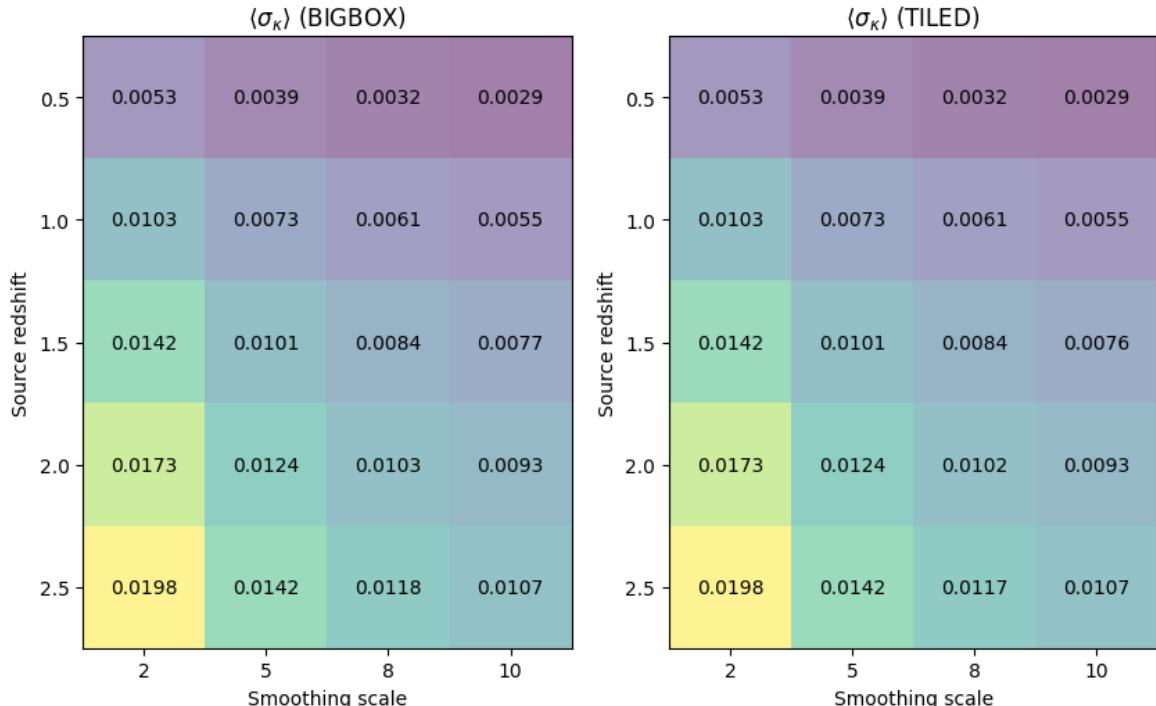


Figure 7.8: Average standard deviation of the noiseless convergence maps for the BIGBOX and TILED simulations. The standard deviation increases with both redshift and smoothing scale, with only subtle differences observed between the BIGBOX and TILED simulations.

7.6 Extracting Weak Lensing Statistics from Convergence Maps

To characterize the influence of super-sample covariance on higher-order statistics, this study focuses on the bispectrum, probability distribution function (PDF), peak counts, minima counts, and Minkowski functionals.

Table 7.2 summarizes the range of values and the computational subroutines employed for each statistical measure.

Statistic	Range	Subroutine (Sky Patch)
Angular Power Spectrum	$300 \leq \ell \leq 3000$	<code>lenstools.powerSpectrum</code>
Bispectrum	$300 \leq \ell \leq 3000$	<code>lenstools.bispectrum</code>
Peak Counts	$-4 \leq \kappa/\sigma_\kappa \leq 4$	<code>lenstools.peakCount</code>
Minima Counts	$-4 \leq \kappa/\sigma_\kappa \leq 4$	<code>lenstools.peakCount</code>
Probability Distribution Function (PDF)	$-4 \leq \kappa/\sigma_\kappa \leq 4$	<code>lenstools.pdf</code>
Minkowski Functionals	$-4 \leq \kappa/\sigma_\kappa \leq 4$	Custom implementation

Table 7.2: Summary of the statistical measures employed in this study, including their respective value ranges and the computational subroutines used for analysis.

7.6.1 Angular Power Spectrum

The angular power spectrum ($C_\ell^{\kappa\kappa}$) is estimated directly from the simulated convergence maps using `lenstools` (Petri, 2016), without any preliminary smoothing. The considered multipole range spans from $\ell = 300$ to $\ell = 3000$, partitioned into eight logarithmically spaced bins. This binning scheme is chosen to maintain consistency with the multipole selection used in the Hyper Suprime-Cam Year 3 (HSC Y3) cosmic shear analysis (Dalal et al., 2023).

The lower limit of $\ell = 300$ excludes large-scale modes, as the primary focus of this study is on higher-order statistics, which are most sensitive to intermediate and small angular scales. Conversely, the upper limit of $\ell = 3000$ ensures the inclusion of small-scale modes where the super-sample effect becomes increasingly significant. Furthermore, this multipole range is robust given the sampling of simulated maps, as discussed in Section 7.4.

For benchmarking, we compute the theoretical angular power spectrum using the `Halofit` model (Takahashi et al., 2012) and compare it with the measured angular power spectrum. The theoretical prediction is generated using the same set of cosmological parameters as those employed in the simulations.

7.6.2 Bispectrum

The bispectrum (B_ℓ) is computed from the unsmoothed convergence maps using `lenstools`. We consider three distinct configurations: equilateral ($\ell_1 = \ell_2 = \ell_3$), squeezed ($\ell_1 = \ell_2 = 10\ell_3$),

and isosceles ($\ell_1 = \ell_2 = 2\ell_3$). These configurations are chosen to capture different shapes of the bispectrum, providing complementary information about the underlying matter distribution.

The bispectrum computations are confined to the same multipole range as the angular power spectrum, specifically $\ell \in [300, 3000]$, divided into eight logarithmically spaced bins. Although the bispectrum is more sensitive to noise and small-scale structures, maintaining an identical multipole range facilitates direct comparison with the angular power spectrum results.

For theoretical validation, we compute the bispectrum prediction using the BiHalofit model (Takahashi et al., 2020) and compare it with the measured bispectrum from the simulations. The theoretical bispectrum is derived using the same cosmological parameters as those employed in the simulations.

7.6.3 PDF

We compute the probability distribution function (PDF) of the convergence field using `lenstools`. Each PDF is derived from the smoothed convergence maps over a normalized range of $-4 \leq \kappa/\sigma_\kappa \leq 4$, divided into eight equally spaced bins. Here, σ_κ represents the standard deviation of the convergence field within each individual patch. This range is chosen to align with the study by Thiele et al. (2023), while the binning is optimized to ensure that each bin contains a sufficient number of data points.

The theoretical prediction for the PDF is generated using the `hmpdf` code (Thiele et al., 2020), employing the same linear matter power spectrum as that used in the simulations. The theoretically predicted PDF is then compared with the measured PDF to evaluate the consistency and accuracy of the underlying cosmological model and its assumptions.

7.6.4 Peak/Minima Counts

Peak and minima counts are computed from the smoothed convergence maps using `lenstools`, utilizing the same normalized range as the PDF: $-4 \leq \kappa/\sigma_\kappa \leq 4$, divided into eight evenly spaced bins. While the highest and lowest peaks are represented by relatively few data points, these extreme bins are retained to ensure consistency with the binning scheme adopted for the PDF.

7.6.5 Minkowski Functionals

The Minkowski functionals are calculated from the smoothed convergence maps using a custom implementation that adheres closely to the definitions outlined in Section 4.6. As with the PDF and peak/minima counts, these functionals are computed over the normalized range $-4 \leq \kappa/\sigma_\kappa \leq 4$, divided into eight linearly spaced bins.

Figure 7.9 illustrates the variance of the gradient field, $\sigma_1 = \sqrt{\kappa_x^2 + \kappa_y^2}$, which is a critical

input for calculating the Minkowski functionals. As the smoothing scale increases, σ_1 decreases, reflecting the reduced influence of small-scale structures. Differences between the BIGBOX and TILED simulations, as well as across varying redshifts, remain subtle, highlighting the robustness of these measures and their relative insensitivity to large-scale environmental variations.

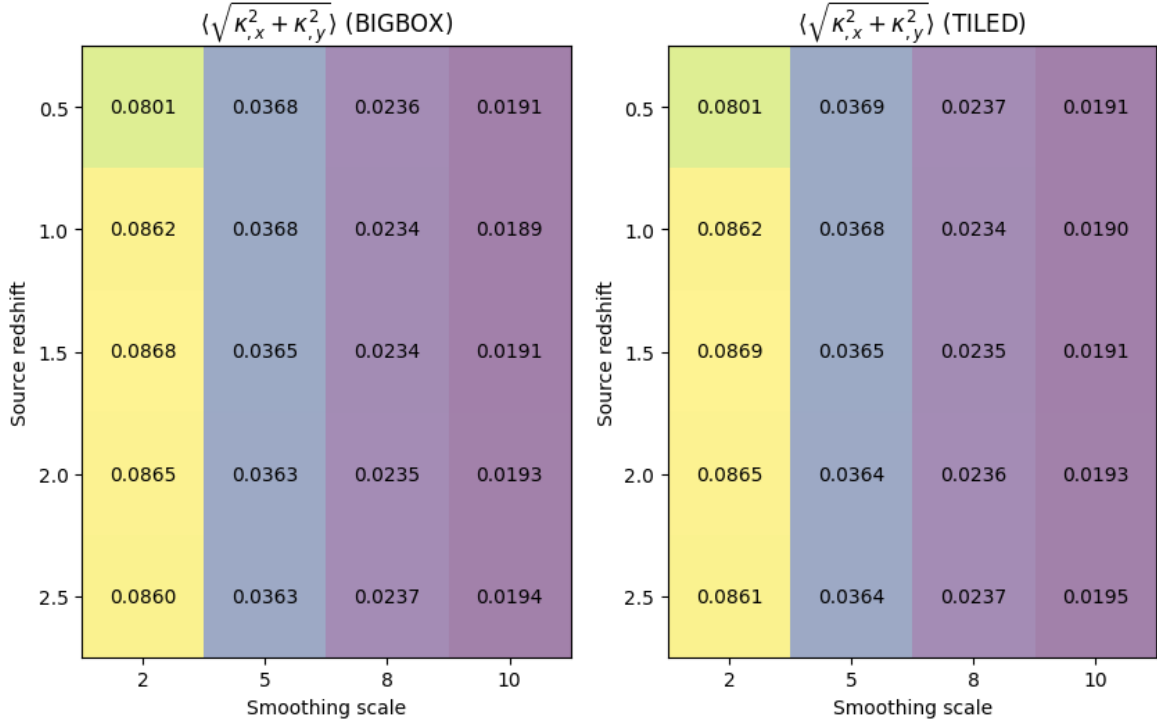


Figure 7.9: Average $\sigma_1 = \sqrt{\kappa_x^2 + \kappa_y^2}$ of the noiseless convergence maps for the BIGBOX and TILED simulations. These values are calculated for the smoothing scales $\theta_G = 2', 5', 8',$ and $10'.$ σ_1 decreases as the smoothing scale increases, while differences between the BIGBOX and TILED simulations, or across redshifts, remain subtle.

7.7 Comparing Covariances from BIGBOX and TILED

After the measurement phase, this study investigates the impact of super-sample covariance on the covariance matrices of the statistical measures discussed earlier. To facilitate this analysis, we use an unbiased estimator for the covariance matrix, as defined in Equation 7.8.

$$\text{Cov}(\mathcal{O}_i, \mathcal{O}_j) = \frac{1}{N_{\text{sim}} - 1} \sum_{n=1}^{N_{\text{sim}}} (\mathcal{O}_i^{(n)} - \langle \mathcal{O}_i \rangle)(\mathcal{O}_j^{(n)} - \langle \mathcal{O}_j \rangle), \quad (7.8)$$

Additionally, we compute the correlation matrix for each statistical measure to analyze the interdependence between different scales and configurations. The correlation matrix is defined as:

$$\rho_{ij} = \frac{\text{Cov}(\mathcal{O}_i, \mathcal{O}_j)}{\sqrt{\text{Cov}(\mathcal{O}_i, \mathcal{O}_i)\text{Cov}(\mathcal{O}_j, \mathcal{O}_j)}}, \quad (7.9)$$

where \mathcal{O}_i and \mathcal{O}_j represent the i -th and j -th statistical measures, respectively. Correlation matrix normalize off-diagonal elements by the scale dependent variance, thereby enabling a direct comparison between different simulations and statistical measures.

After computing the covariance and correlation matrices for both the BIGBOX and TILED simulations, we assess the impact of super-sample covariance by comparing the two sets of matrices. The comparison is performed by calculating the ratio of the BIGBOX to TILED matrices, defined as:

$$R_{ij}^{\text{Cov}} = \frac{\text{Cov}_{ij}^{\text{BIGBOX}}}{\text{Cov}_{ij}^{\text{TILED}}}, \quad R_{ij}^{\rho} = \frac{\rho_{ij}^{\text{BIGBOX}}}{\rho_{ij}^{\text{TILED}}}, \quad (7.10)$$

where $\text{Cov}_{\text{BIGBOX}}$ and $\text{Cov}_{\text{TILED}}$ denote the covariance matrices derived from the BIGBOX and TILED simulations, respectively. Similarly, ρ_{BIGBOX} and ρ_{TILED} represent the corresponding correlation matrices.

To quantitatively evaluate the overall influence of super-sample covariance, we compute the mean values of the ratios R_{ij}^{Cov} and R_{ij}^{ρ} across the respective covariance and correlation matrices. Specifically, the average of R^{ρ} is calculated by excluding the diagonal elements, which are intrinsically equal to unity by definition. In contrast, the average of R^{Cov} utilizes all elements of the covariance matrix, including the diagonal.

For ℓ -binned statistics, such as the angular power spectrum ($C_{\ell}^{\kappa\kappa}$) and the bispectrum, the average ratio is determined across all available multipole bins. Conversely, for ν -binned statistics, such as the PDF, peak/minima counts, and Minkowski functionals, the first and last bins are excluded from the ratio calculation to avoid biases introduced by limited data points and the inherent unreliability of these extreme bins. The average ratios are defined as follows:

$$\langle R^{\text{Cov}} \rangle = \frac{1}{N_{\text{bins}}^2} \sum_{i,j} R_{ij}^{\text{Cov}}, \quad \langle R^{\rho} \rangle = \frac{1}{N_{\text{bins}}^2 - N_{\text{bins}}} \sum_{i \neq j} R_{ij}^{\rho}, \quad (7.11)$$

where $N_{\text{bins}} = 8$ for ℓ -binned statistics and $N_{\text{bins}} = 6$ for ν -binned statistics.

Chapter 8

Comparative Analysis of Statistical Measures and Covariance Structures in BIGBOX and TILED

Contents

8.1	Comparison of Mean and Variance for Statistical Measures	82
8.2	Analysis of Covariance and Correlation Matrices	85
8.3	Effects of Noise on Statistical Measures	91
8.4	Influence of Smoothing Scale	94
8.5	Systematic Effects: Box Replication Artifact	97

This chapter compares a suite of weak lensing statistics obtained from two simulation sets: BIGBOX and TILED. Our goal is to quantify differences in mean values, covariance, and correlation matrices to evaluate the impacts of super-sample covariance and other systematic effects on these measurements. We will also examine the effects of shape noise, smoothing scales, and box replication artifacts on the results. Unless otherwise specified, the main results presented are derived from noiseless simulations with a smoothing scale of 2 arcminutes.

8.1 Comparison of Mean and Variance for Statistical Measures

We analyze and compare the mean (μ) and variance (σ^2) of statistical measures derived from the BIGBOX and TILED simulations. Figures 8.1 and 8.2 illustrate these comparisons for the angular power spectrum, bispectrum, and other higher-order statistics, highlighting the differences caused by simulation methodologies and super-sample covariance effects.

The mean values, represented by the ratio R_μ , exhibit remarkable consistency in capturing statistical distributions across the two simulation sets. For most statistics, deviations in R_μ are less than 1%, underscoring the robustness of both pipelines in reproducing the underlying statistics. However, systematic deviations emerge at low ν values for peak counts, minima, and Minkowski Functionals.

These deviations likely stem from the limited ability of the TILED simulations to resolve low-density regions.

In contrast, the variance ratios R_{σ^2} reveal more pronounced differences, highlighting the critical impact of super-sample covariance on variance measurements. The variance for the angular power spectrum exhibits a significant increase in the BIGBOX simulations at high ℓ , consistent with the expected amplification due to the inclusion of larger-scale modes in the BIGBOX setup, which are absent in the TILED simulations. Furthermore, variance ratio discrepancies grow with increasing source redshift, reflecting the progressive loss of large-scale modes in the TILED simulations. For ν -binned statistics, the BIGBOX simulations consistently yield higher variances across nearly all ν bins, with this trend becoming more pronounced at higher source redshifts. These findings highlight the influence of super-sample covariance on higher-order statistics.

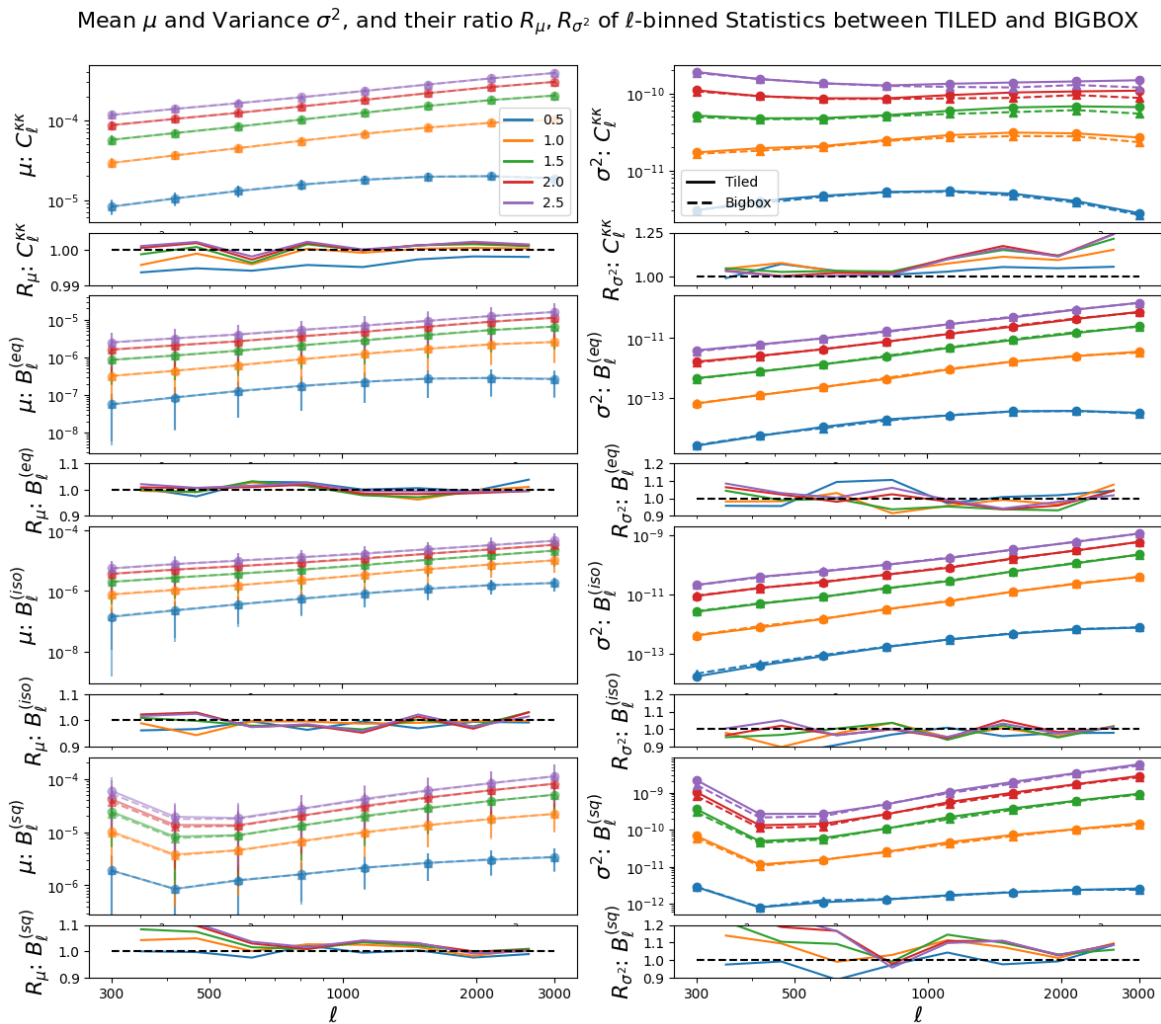


Figure 8.1: Comparison of the mean and variance for the angular power spectrum ($C_{\ell}^{\kappa\kappa\ell}$) and the bispectrum components across three configurations: equilateral ($B_{\ell}^{(eq)}$), isosceles ($B_{\ell}^{(iso)}$), and squeezed ($B_{\ell}^{(sq)}$). Results are presented for the BIGBOX and TILED simulations across source redshifts $z_s = 0.5, 1.0, 1.5, 2.0$, and 2.5 .

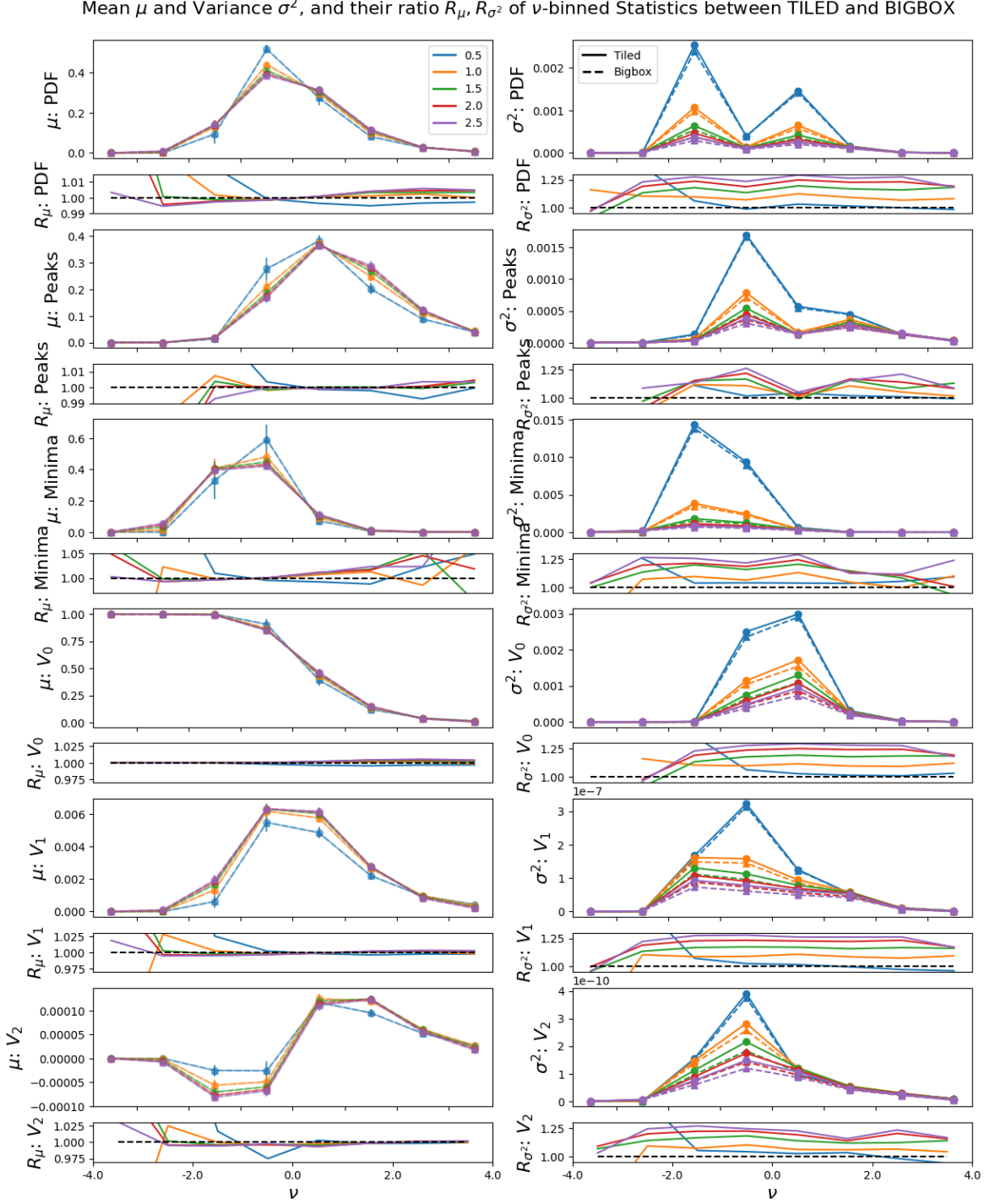


Figure 8.2: Comparison of the mean and variance for ν -binned statistics, including the Minkowski Functionals (V_0, V_1, V_2), the probability density function (PDF), and peak and minima counts. Results are derived from the BIGBOX and TILED simulations across source redshifts $z_s = 0.5, 1.0, 1.5, 2.0$, and 2.5 , highlighting their sensitivity to super-sample covariance.

8.2 Analysis of Covariance and Correlation Matrices

To quantify the impact of super-sample covariance on the off-diagonal terms, we compare the covariance and correlation matrices of the statistical measures.

Figure 8.4 presents the covariance matrices for the BIGBOX simulations. Figure 8.5 displays the corresponding matrices for the TILED simulations. The general covariance structures are consistent between the two simulation sets, with the BIGBOX simulations exhibiting higher covariance values on average. Figure 8.6 illustrates the correlation matrices for the BIGBOX and TILED simulations. The upper-left triangle of each panel shows the correlation coefficients derived from the BIGBOX simulations, while the lower-right triangle displays the corresponding values from the TILED simulations. No obvious discrepancies are visible in the color scale, suggesting that the correlation structures are almost consistent between the two simulation sets.

Figures 8.7 and 8.8 illustrate the ratios of covariance and correlation matrices between the BIGBOX and TILED simulations, denoted R_{Cov} and R_{ρ} , respectively. These comparisons quantitatively assess the influence of super-sample covariance on the diagonal and off-diagonal elements of the covariance structure. The covariance ratios R_{Cov} generally exceed unity, ranging from 10% to 30% above the baseline values for most statistical measures. This consistent elevation underscores the significant contribution of super-sample covariance to the overall covariance matrix. Conversely, the correlation ratios R_{ρ} typically deviate by less than 5%. These results suggest that the super-sample effect impacts not only the diagonal terms but also the off-diagonal elements of the covariance matrix, thereby elevating the entire covariance structure. Notable exceptions to these trends occur in the angular power spectrum and peak/minima counts. For the angular power spectrum, larger deviations in the correlation ratios are consistent with super-sample covariance effects, which arise from the strong correlations introduced by shared large-scale modes, particularly at small ℓ . In contrast, the deviations observed in the peak/minima counts likely stem from systematic shifts in peak positions within the TILED simulations, leading to changes in correlations near the peak bins. For a summary of the average ratios of covariance and correlation matrices, see Figure 8.3.

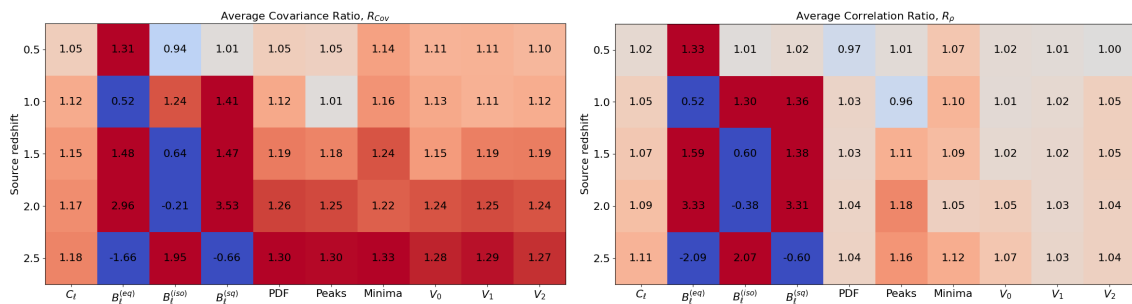


Figure 8.3: Average ratios of covariance matrices (left) and correlation matrices (right) between the BIGBOX and TILED simulations for multiple source redshifts. The increasing trend in the covariance ratios highlights the contribution of super-sample covariance to the covariance structure.

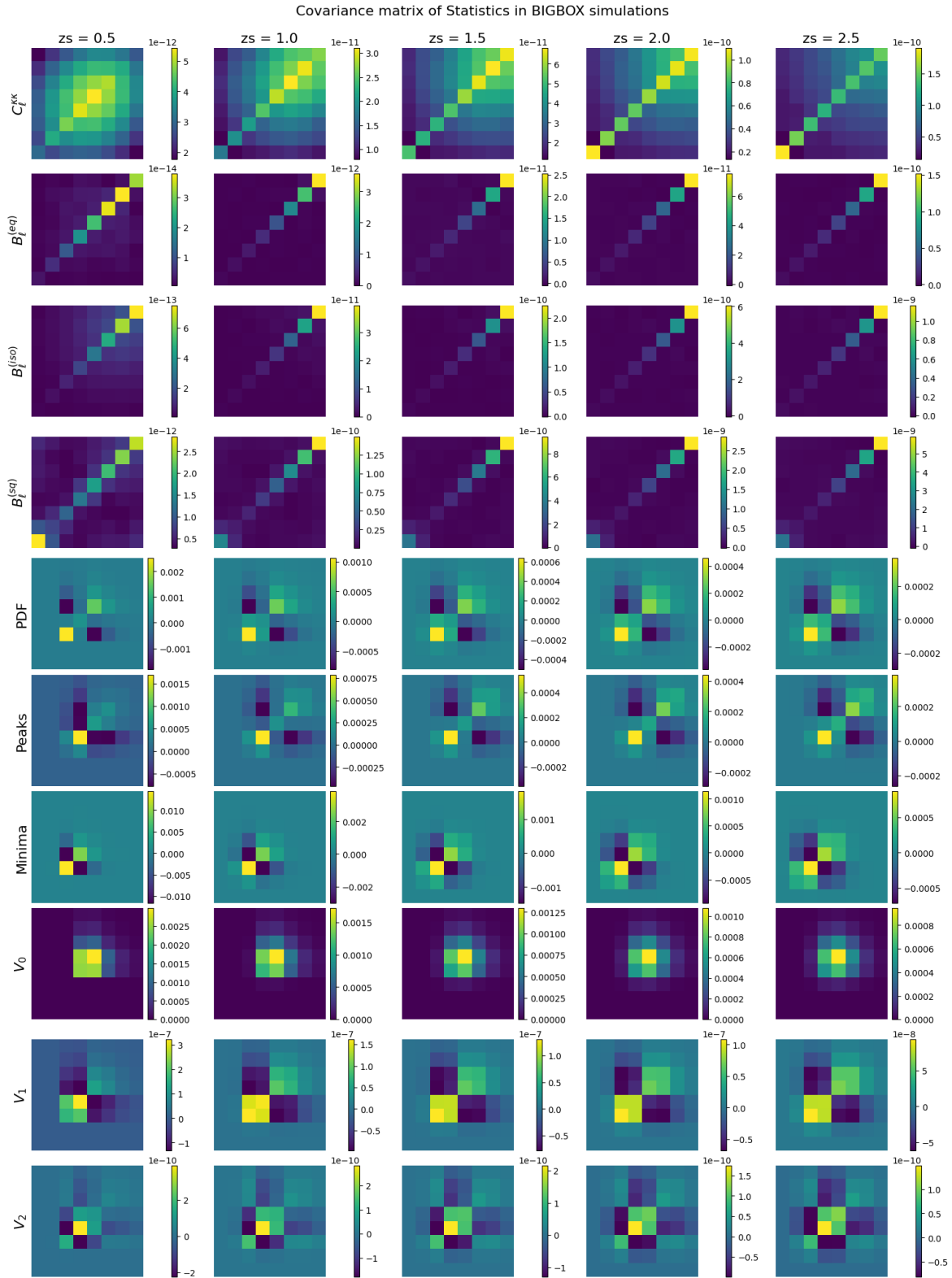


Figure 8.4: Covariance matrices of statistical measures in the BIGBOX simulations across multiple source redshifts, illustrating the covariance structure influenced by super-sample covariance.

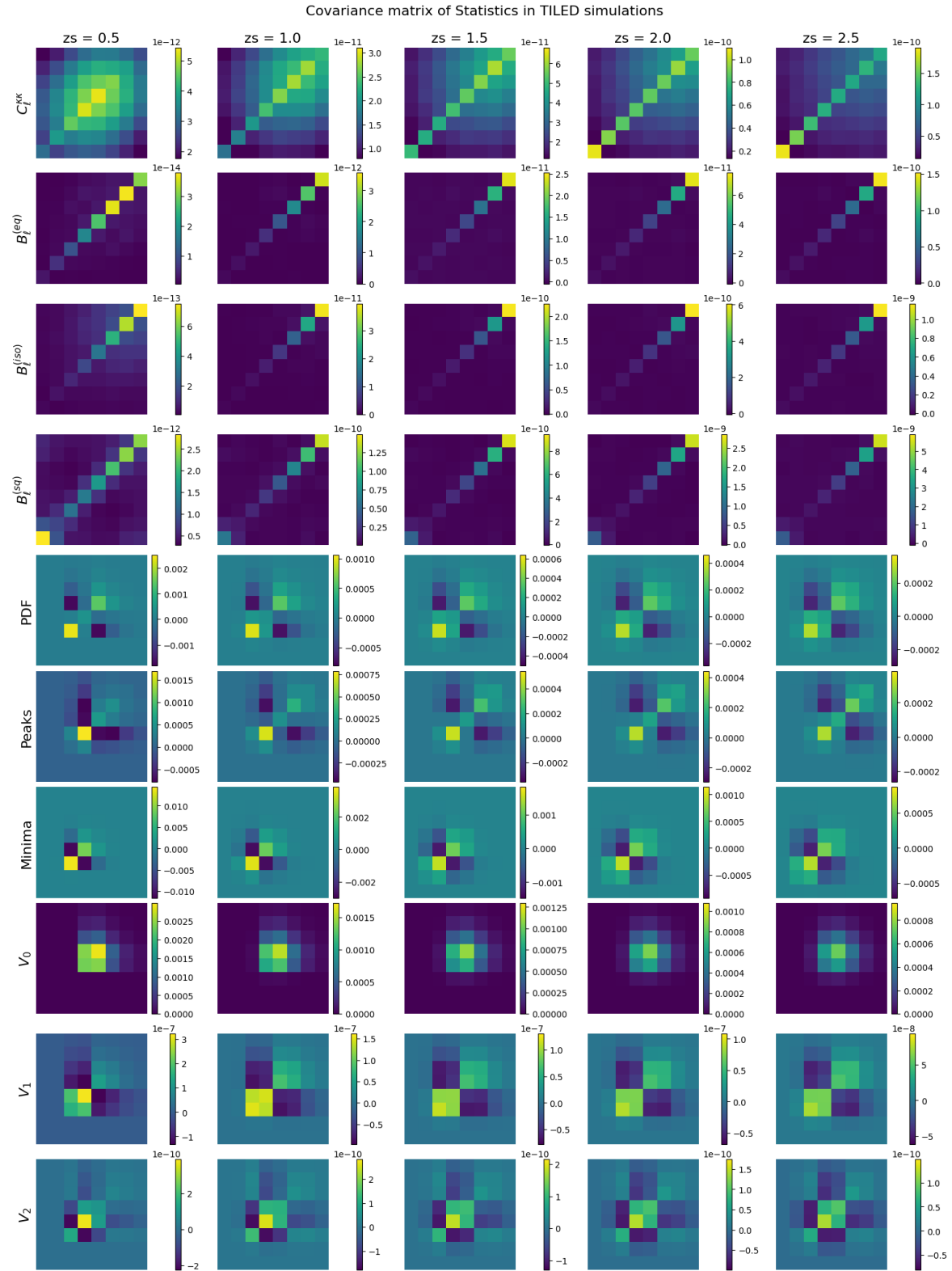


Figure 8.5: Covariance matrices of statistical measures in the TILED simulations across multiple source redshifts, using a color scale consistent with Figure 8.4.

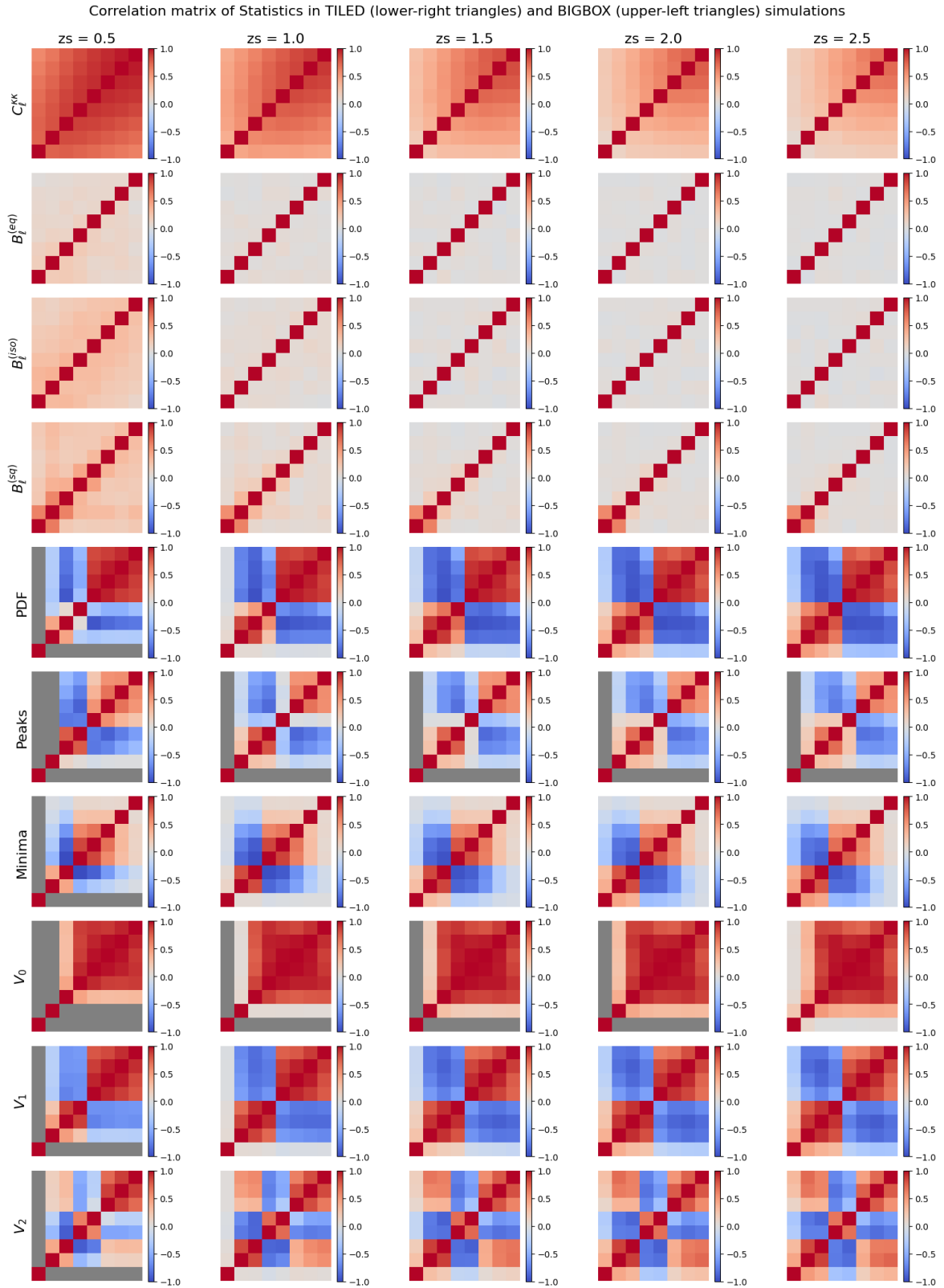


Figure 8.6: Correlation matrices of statistical measures in the BIGBOX and TILED simulations across multiple source redshifts. The upper-left triangle contains correlation coefficients from BIGBOX simulations, and the lower-right triangle displays values from TILED simulations.

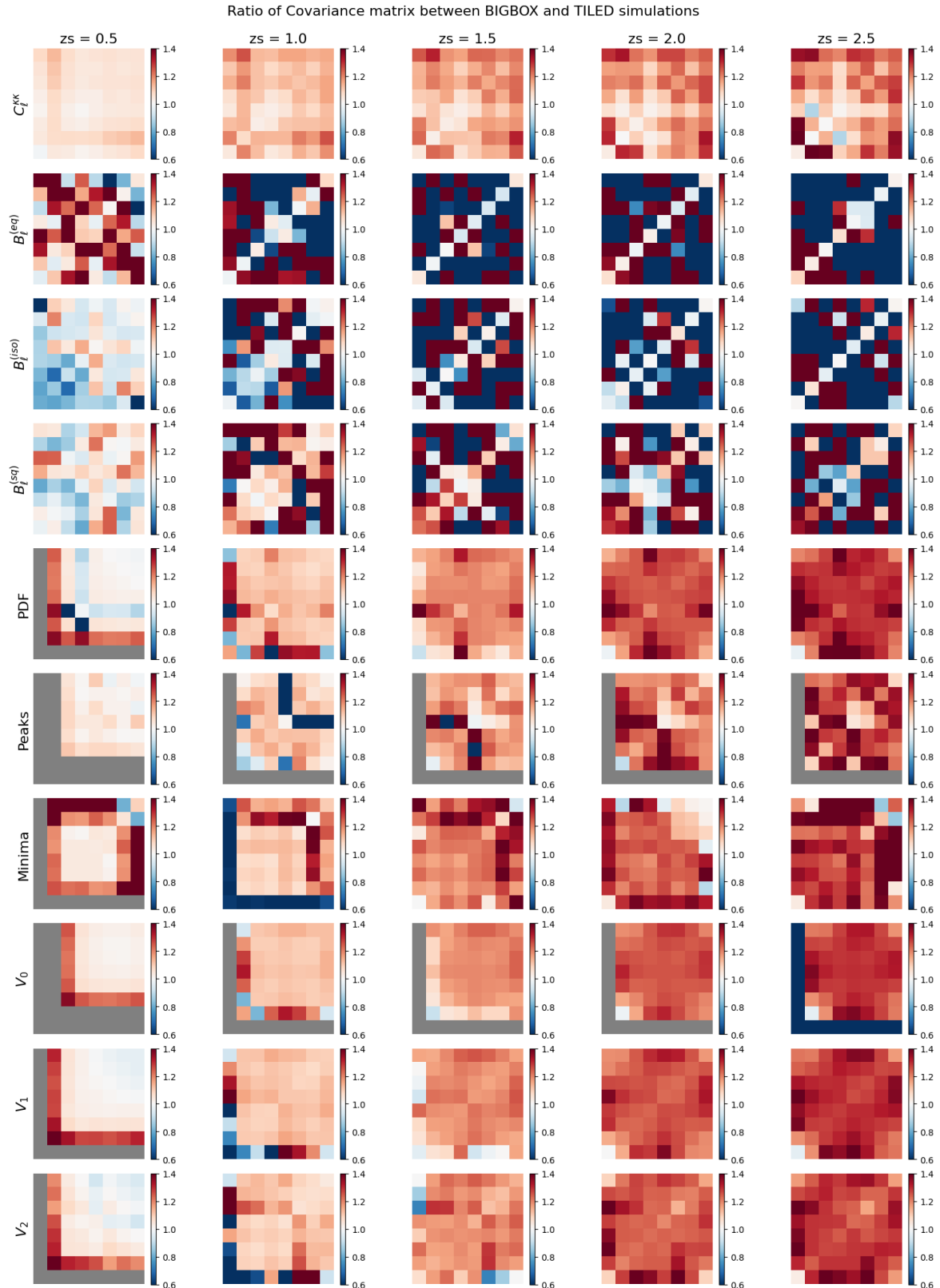


Figure 8.7: Ratios of covariance matrices between the BIGBOX and TILED simulations across multiple source redshifts. The ratios are consistently 10% to 30% higher than unity for most measured statistics, indicating the significant impact of super-sample covariance on the covariance structure.

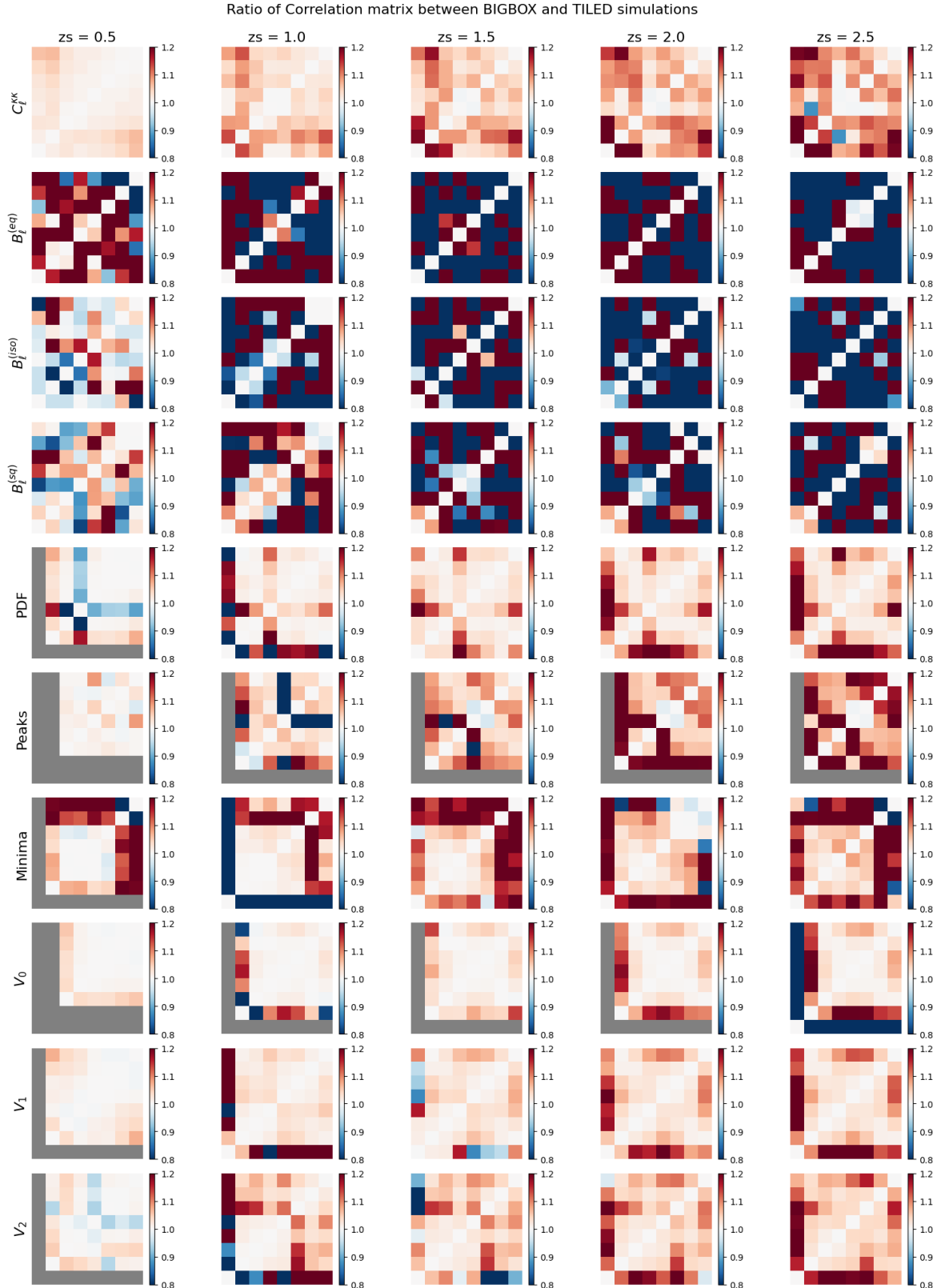


Figure 8.8: Ratios of correlation matrices between the BIGBOX and TILED simulations across multiple source redshifts. The ratios are generally $< 5\%$, indicating that the super-sample effect influences both diagonal and off-diagonal terms, elevating the entire covariance structure.

8.3 Effects of Noise on Statistical Measures

The presence of shape noise in convergence maps can significantly affect the covariance and correlation structures of weak lensing statistical measures. To evaluate the interaction between shape noise and super-sample effects, we analyzed multiple noise levels corresponding to those expected in current and future surveys (see Table 1.1). This analysis aims to quantify the extent to which the super-sample effect dominates over the contribution from shape noise. Since the bispectrums exhibit no clear trends in the noiseless case (as shown in Figures 8.7 and 8.8), we focus our analysis on the angular power spectrum and select higher-order statistics.

Figures 8.9 and 8.10 present the covariance matrix ratios and their averages across statistical measures for the BIGBOX and TILED simulations at various noise levels. While the angular power spectrum and peak/minima counts exhibit greater sensitivity to noise, particularly at high noise levels (e.g., DES and HSC surveys), the covariance ratios consistently exhibit an increasing trend across most statistics. This observation suggests that, in future surveys, the super-sample effect is expected to dominate over the noise contribution.

In contrast, Figures 8.11 and 8.12 display the correlation matrix ratios and their averages across statistical measures at different noise levels. These ratios generally remain below 10% for most statistics, indicating that noise has a minimal impact on the overall covariance structure. Higher values in the correlation ratios are concentrated near the boundaries of each statistical measure. These elevated ratios arise from regions where data points are sparse, rendering the measurements more susceptible to noise amplification.

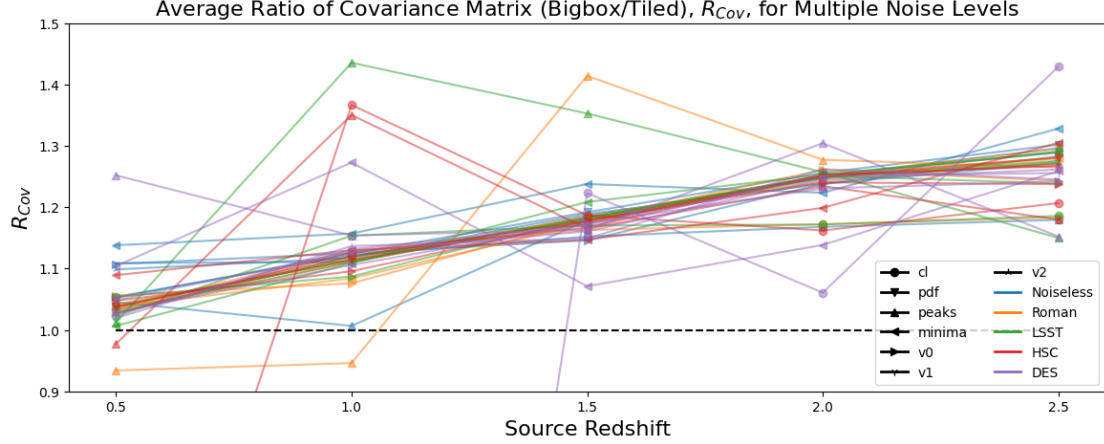


Figure 8.9: Average ratio of covariance matrices for statistical measures between the BIGBOX and TILED simulations at different shape noise levels (see Table 1.1). While the angular power spectrum and peak/minima counts are more sensitive to noise, particularly at high levels corresponding to surveys like DES and HSC, the increasing trend in covariance ratios remains consistent across most statistical measures.

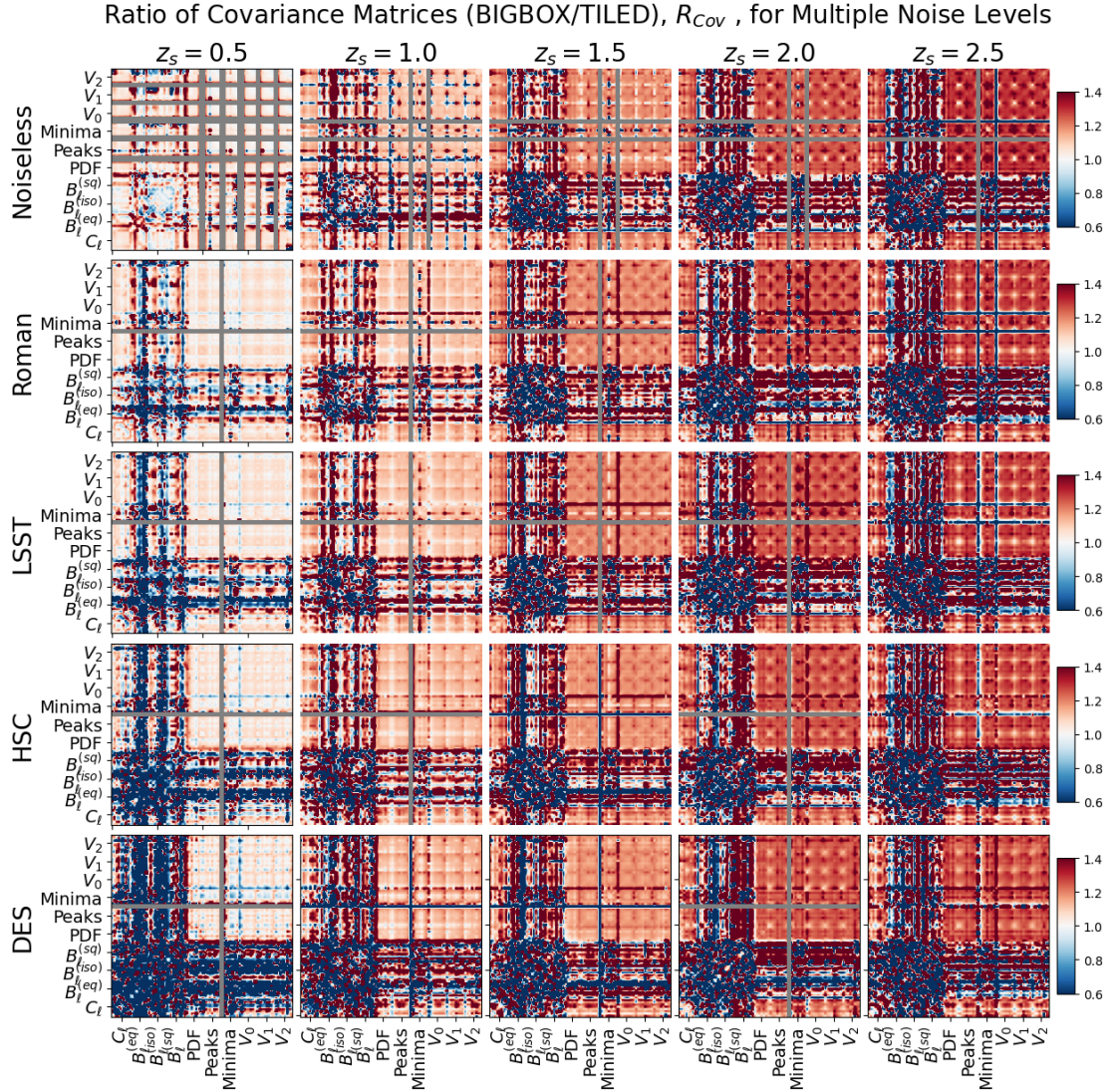


Figure 8.10: Ratio of covariance matrices for statistical measures between the BIGBOX and TILED simulations at varying shape noise levels. The covariance ratios exhibit a consistent increasing trend, highlighting the persistent influence of super-sample covariance across varying noise conditions.

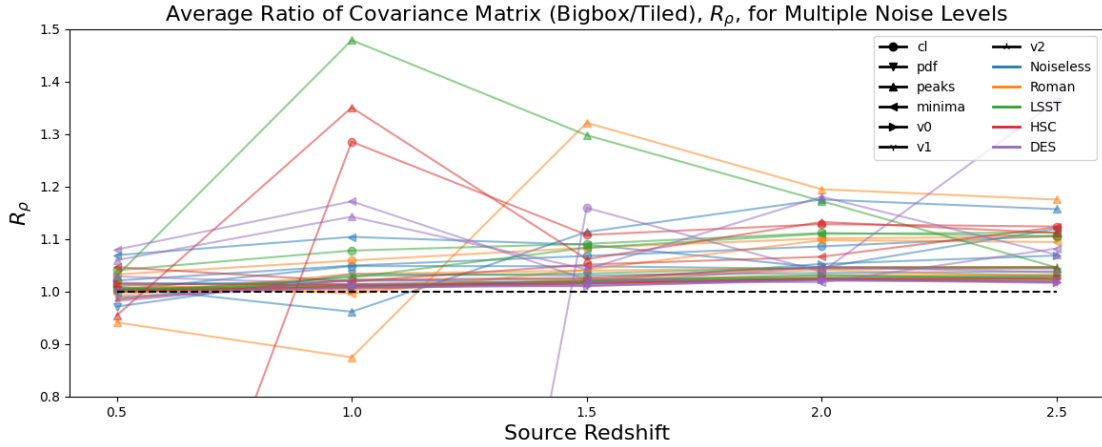


Figure 8.11: Average ratio of correlation matrices for statistical measures between the BIGBOX and TILED simulations at varying shape noise levels (see Table 1.1). While the angular power spectrum, peak counts, and minima counts exhibit greater sensitivity to noise, the correlation ratios remain below 10% for most statistical measures.

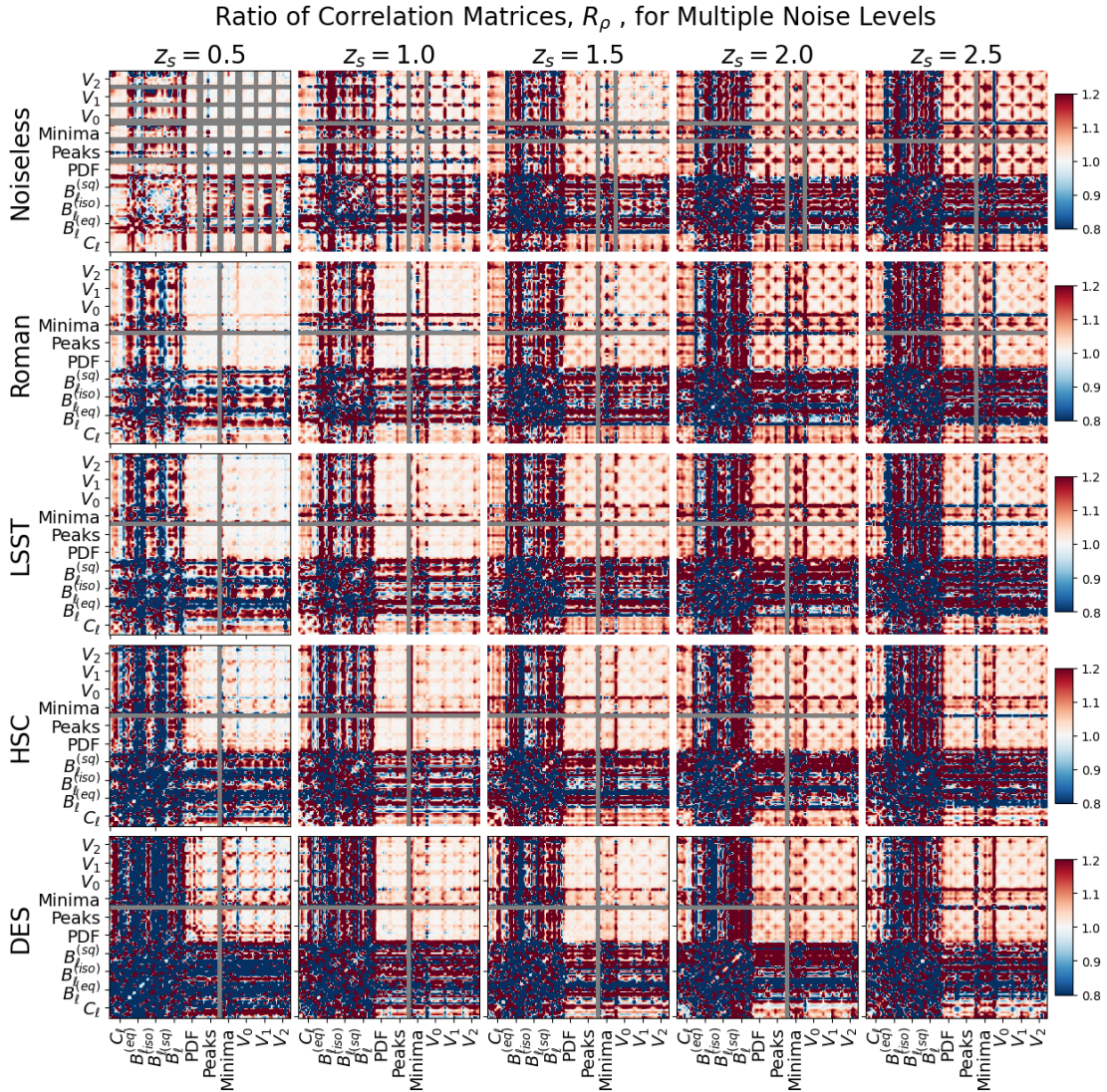


Figure 8.12: Ratio of correlation matrices for statistical measures between the BIGBOX and TILED simulations at different shape noise levels. High correlation ratios are primarily concentrated near the boundaries of statistical measures, due to sparse data points and amplified noise effects.

8.4 Influence of Smoothing Scale

We analyze the impact of varying Gaussian smoothing scales on higher-order statistical measures derived from convergence maps, with a focus on how smoothing alters their underlying structures. Increasing the smoothing scale progressively suppresses small-scale features, redistributing signal intensities across scales. Notably, smoothed convergence maps were not utilized for the calculation of the angular power spectrum and bispectrum; thus, the results are presented exclusively for other higher-order statistics.

Figures 8.13 and 8.14 illustrate the changes in covariance matrix ratios and their averages as a function of the Gaussian smoothing scale. Across all smoothing scales, the average covariance ratios between the BIGBOX and TILED simulations exhibit a consistent upward trend for most statistical measures. However, notable variations occur in the peak and minima counts, particularly at larger smoothing scales. These variations are attributed to the averaging methodology, where contributions from the edges of ν bins and peak bins become increasingly significant at higher smoothing levels.

Figures 8.15 and 8.16 present the ratios of correlation matrices and their averages across different Gaussian smoothing scales. The correlation ratios generally remain below 5% for most statistical measures, indicating that the overall structure of the covariance matrix is robust to variations in smoothing scale. However, similar to the covariance trends, peak and minima counts exhibit elevated correlation ratios, particularly at larger smoothing scales.

In summary, these findings suggest that while Gaussian smoothing scales can influence individual statistical measures, the overall structural integrity of the covariance and correlation matrices remains largely unaffected by changes in smoothing scale.

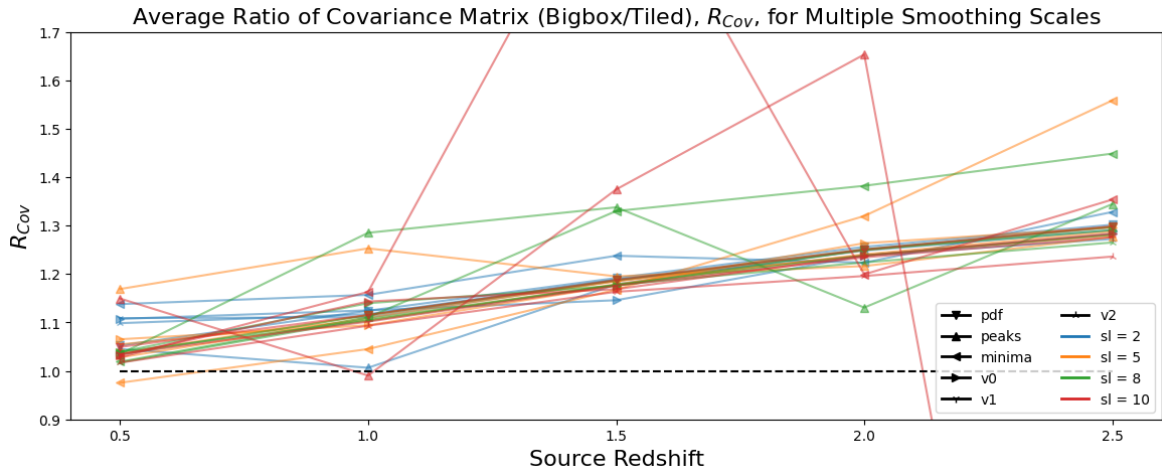


Figure 8.13: Average ratio of covariance matrices for various statistical measures between the BIG-BOX and TILED simulations at differing Gaussian smoothing scales, illustrating the effect of smoothing on covariance ratios. The overall increasing trend persists across all smoothing scales, with pronounced variations in peak and minima counts becoming more evident at larger smoothing scales, due to the increased significance of edge contributions in ν bins.

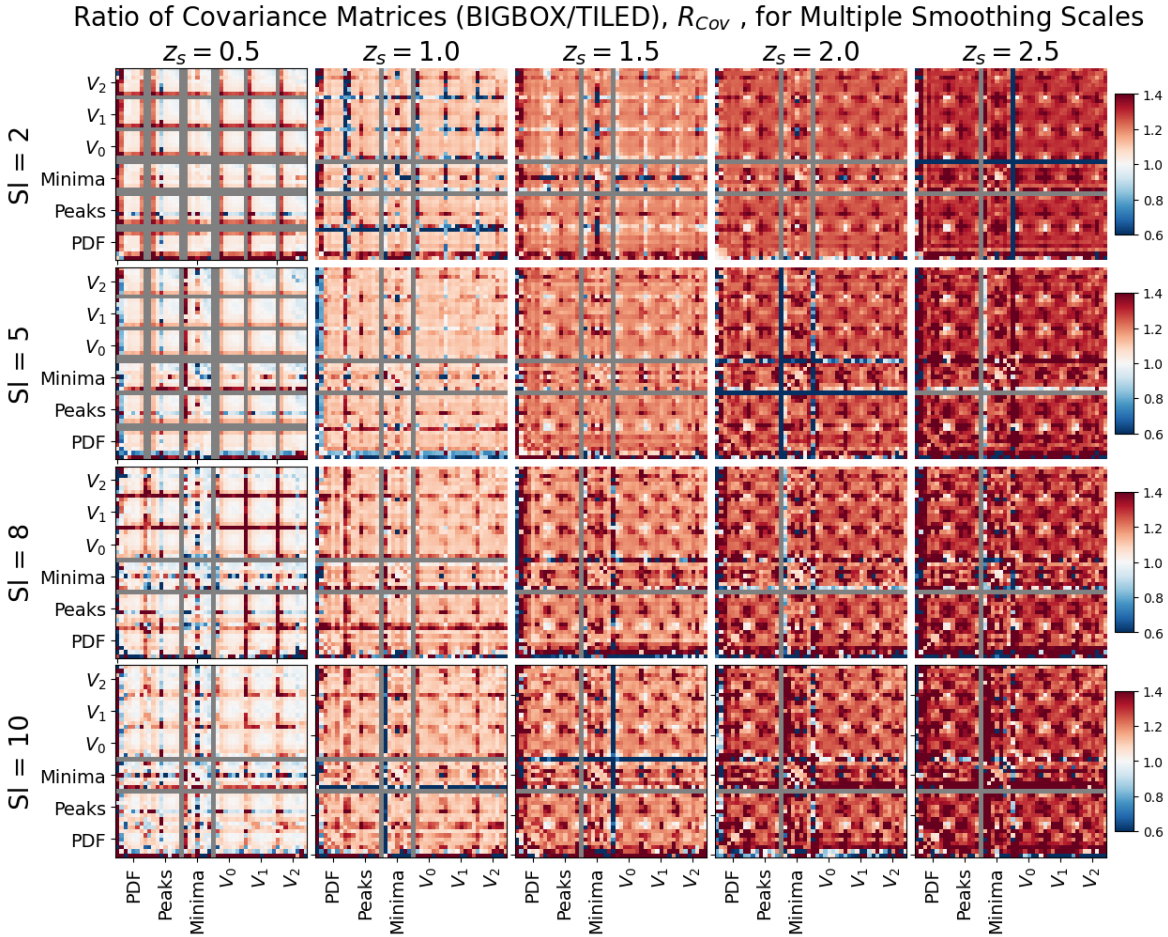


Figure 8.14: Ratio of covariance matrices for various statistical measures between the BIGBOX and TILED simulations across different Gaussian smoothing scales, highlighting the consistent trends in covariance ratios regardless of the applied smoothing scale.

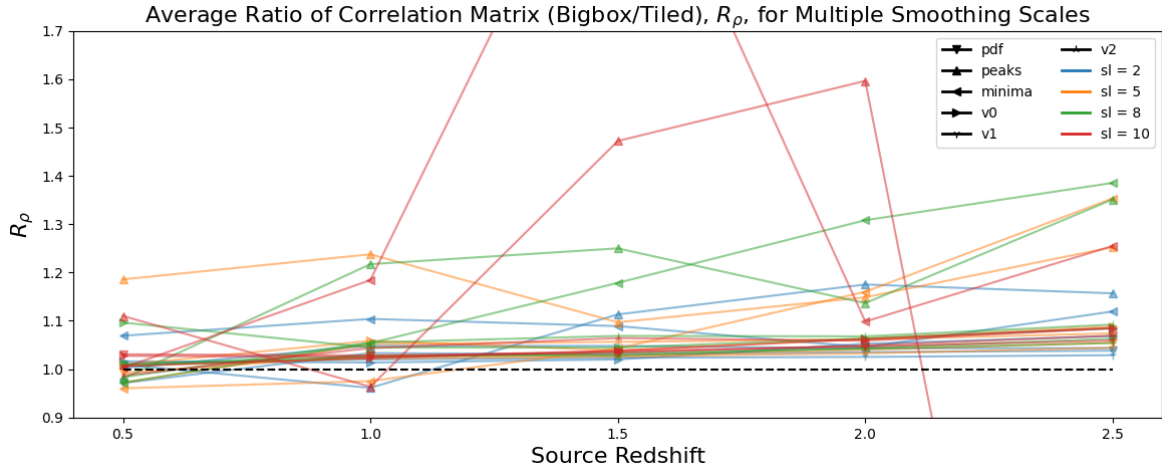


Figure 8.15: Average ratio of correlation matrices for various statistical measures between the BIG-BOX and TILED simulations at different Gaussian smoothing scales. Correlation ratios predominantly remain below 5% for most statistical measures, highlighting the limited influence of smoothing on the overall correlation structure. Peak and minima counts, however, exhibit larger variations at higher smoothing scales, driven by edge effects in ν bins.

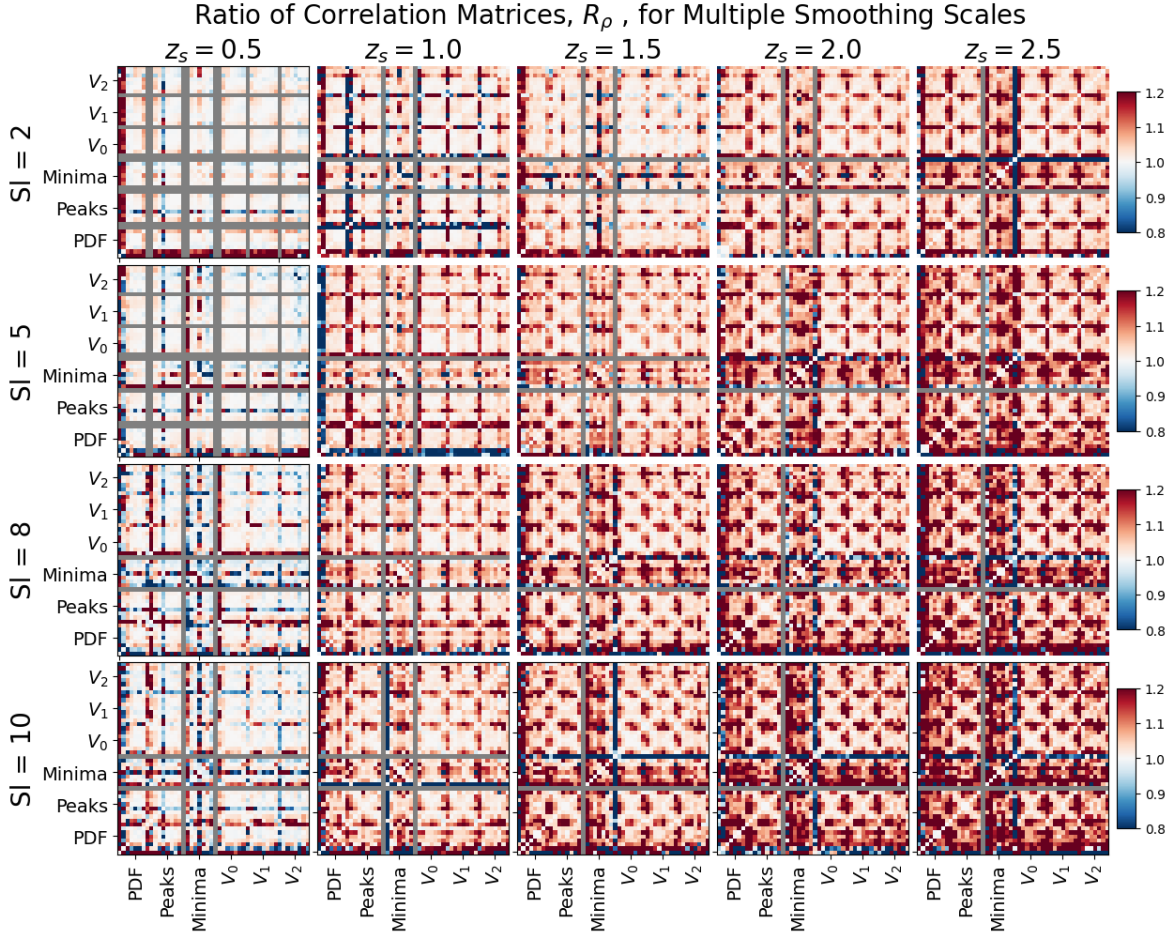


Figure 8.16: Ratio of correlation matrices for various statistical measures between the BIGBOX and TILED simulations across different Gaussian smoothing scales. Apart from near the boundaries of ν bins, the correlation ratios remain consistently modest across all smoothing scales.

8.5 Systematic Effects: Box Replication Artifact

In weak lensing simulations, extending the simulated volume often requires replicating finite simulation boxes to create a larger effective volume. This box replication process can inadvertently introduce artificial correlations in the data, particularly near the boundaries or along preferred replication directions. These artifacts can potentially compromise the reliability of higher-order statistical measures. To systematically investigate this issue, we categorize simulation regions into two groups: regions where artifacts are significant, termed **Replication-Influenced Patches (RIP)**, and regions minimally affected by artifacts, termed **Replication-Minimal Patches (RMP)**. The criteria for categorizing patches are as follows:

- Replication-Influenced Patches (RIP):
 - Patches near the equator: $|\theta_i - \frac{\pi}{2}| \leq R_{\text{patch}}$
 - Patches near the edges of octants: $|\phi_i - \frac{k\pi}{2}| \leq R_{\text{patch}}$ for $k = 0, 1, 2, 3$
- Replication-Minimal Patches (RMP):
 - All other patches not meeting the above criteria.

where (θ_i, ϕ_i) denote the center of patch i , and $R_{\text{patch}} = 5\sqrt{2} \text{ deg}$ is the half-diagonal of the patch.

Our analysis indicates that patches containing the point $(\theta_i, \phi_i) = (\pi/2, 0)$ exhibit significant deviations in both the mean and variance of statistical measures compared to other RIPs. To prevent these outliers from skewing our results, we exclude this specific point from subsequent analyses.

After these adjustments, we obtained 70 RMP per realization, and 1400 RMP for the TILED simulations and 770 RMP for the BIGBOX simulations across all realizations.

Figure 8.17 illustrates the ratios of mean and variance for various statistical measures between RIPs and RMPs. The analysis reveals that the mean angular power spectra in RIPs are systematically underestimated by approximately 0.5%. Additionally, the ν -binned statistics exhibit elevated mean values in low ν bins and reduced values in high ν bins. This pattern suggests that box replication accentuates both overdense and underdense regions, leading to more extreme convergence values. In the TILED simulations, the limited resolution in underdense regions shifts the ν -binned statistics toward lower ν bins. Conversely, the variance ratios approach unity, indicating that the box replication effect amplifies variance to levels comparable to those observed in the BIGBOX simulations. Notably, the dependence on source redshift is effectively nullified in RIPs, implying that box replication conceals the super-sample variance.

Figures 8.20 and 8.21 display the ratios of covariance and correlation matrices between TILED and BIGBOX simulations for RIPs. Additionally, Figures 8.18 and 8.19 present the average ratios for both RIPs and RMPs. The main observations are that RIPs consistently exhibit lower covariance

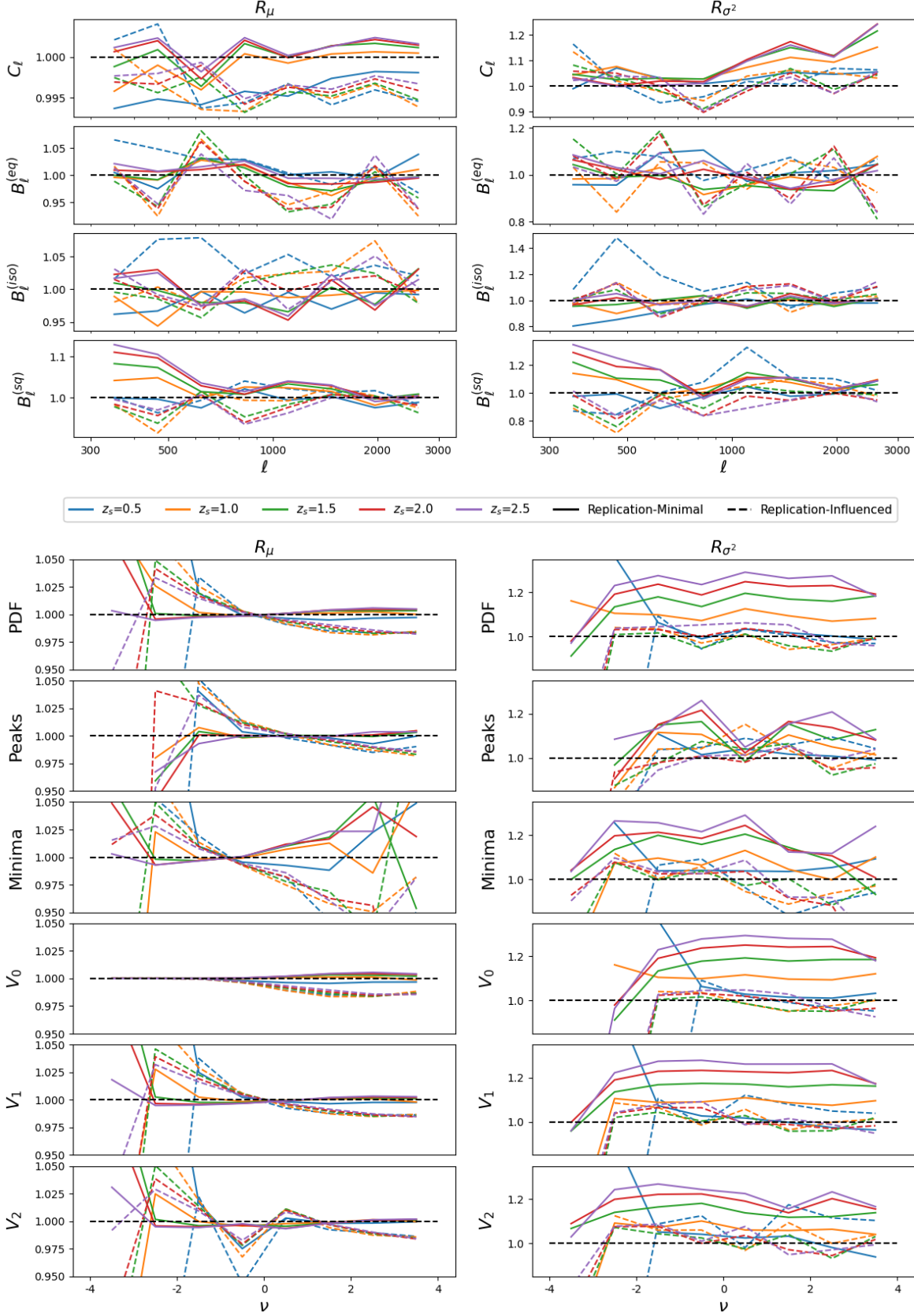


Figure 8.17: Ratios of the mean and variance of statistical measures between Replication-Influenced Patches (RIP) and Replication-Minimal Patches (RMP). The ν -binned statistics exhibit elevated mean values in low ν bins and reduced mean values in high ν bins. Variance ratios are generally close to unity, indicating that box replication amplifies variance to levels comparable to those in BIGBOX simulations.

ratios compared to RMPs. Similarly, the correlation ratios for RIPs are generally lower than those for RMPs, except at $z_s = 0.5$, where the super-sample effect is present in both TILED and BIGBOX simulations. Furthermore, distinct covariance structures, such as those for C_ℓ and V_0 , emerge due to box replication artifacts. Structural transitions observed in previous analyses occur at higher redshifts ($z_s = 2.0 \sim 2.5$) in RIPs, aligning with RMPs as higher redshift regions become dominated by RMPs.

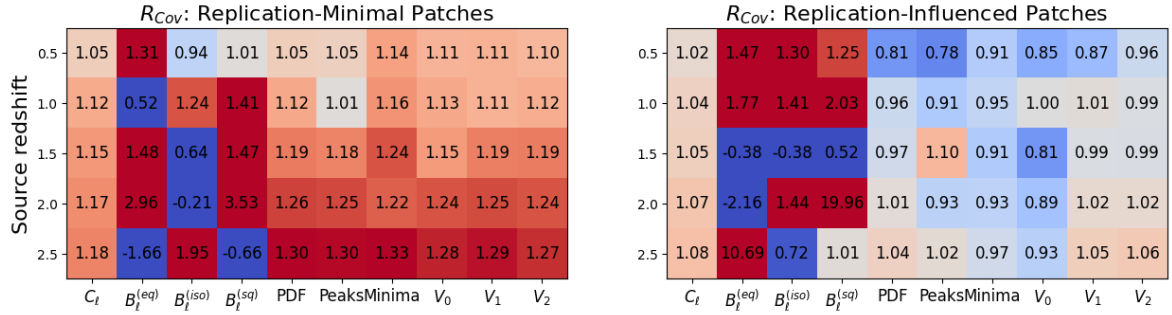


Figure 8.18: Average BIGBOX/TILED ratios of covariance matrices for Replication-Influenced Patches (RIP) and Replication-Minimal Patches (RMP). The ratios for RIPs (right panel) are consistently lower than those for RMPs (left panel), indicating that box replication artifacts reduce covariance ratios in replication-influenced regions.

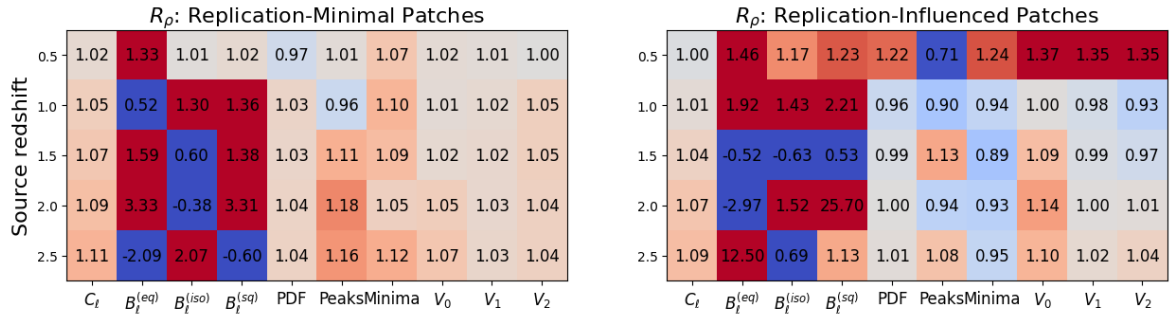


Figure 8.19: Average BIGBOX/TILED ratios of correlation matrices for Replication-Influenced Patches (RIP) and Replication-Minimal Patches (RMP). The ratios for RIPs (right panel) are consistently lower than those for RMPs (left panel), except at $z_s = 0.5$, where super-sample effects impact both TILED and BIGBOX simulations similarly.

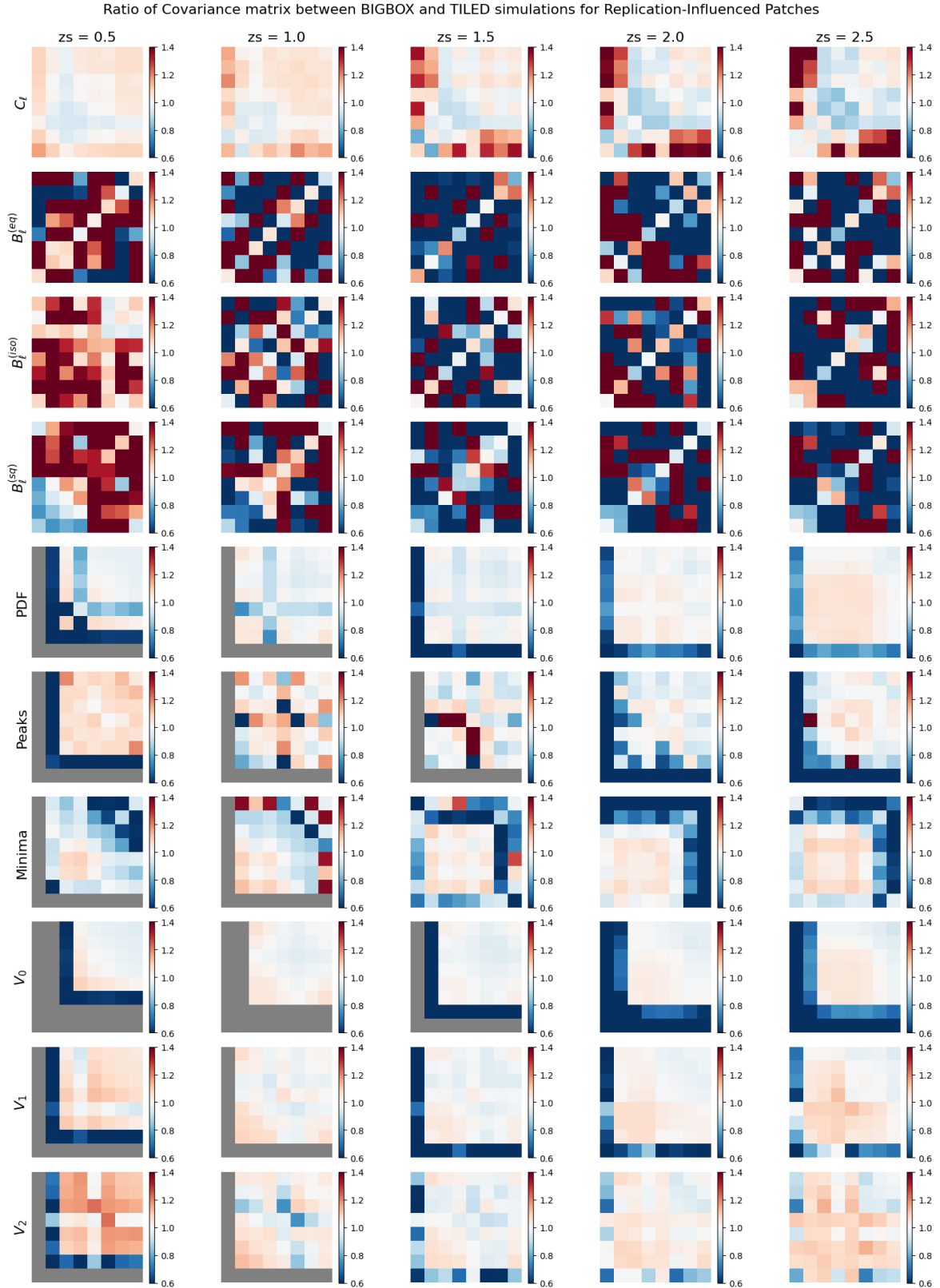


Figure 8.20: BIGBOX/TILED ratios of covariance matrices specifically for Replication-Influenced Patches (RIP). Compared to Figure 8.8, RIP ratios are consistently lower than those for RMPs. Covariance structures unique to RIPs, such as C_ℓ and V_0 , indicate that box replication artifacts can generate distinct covariance structures.

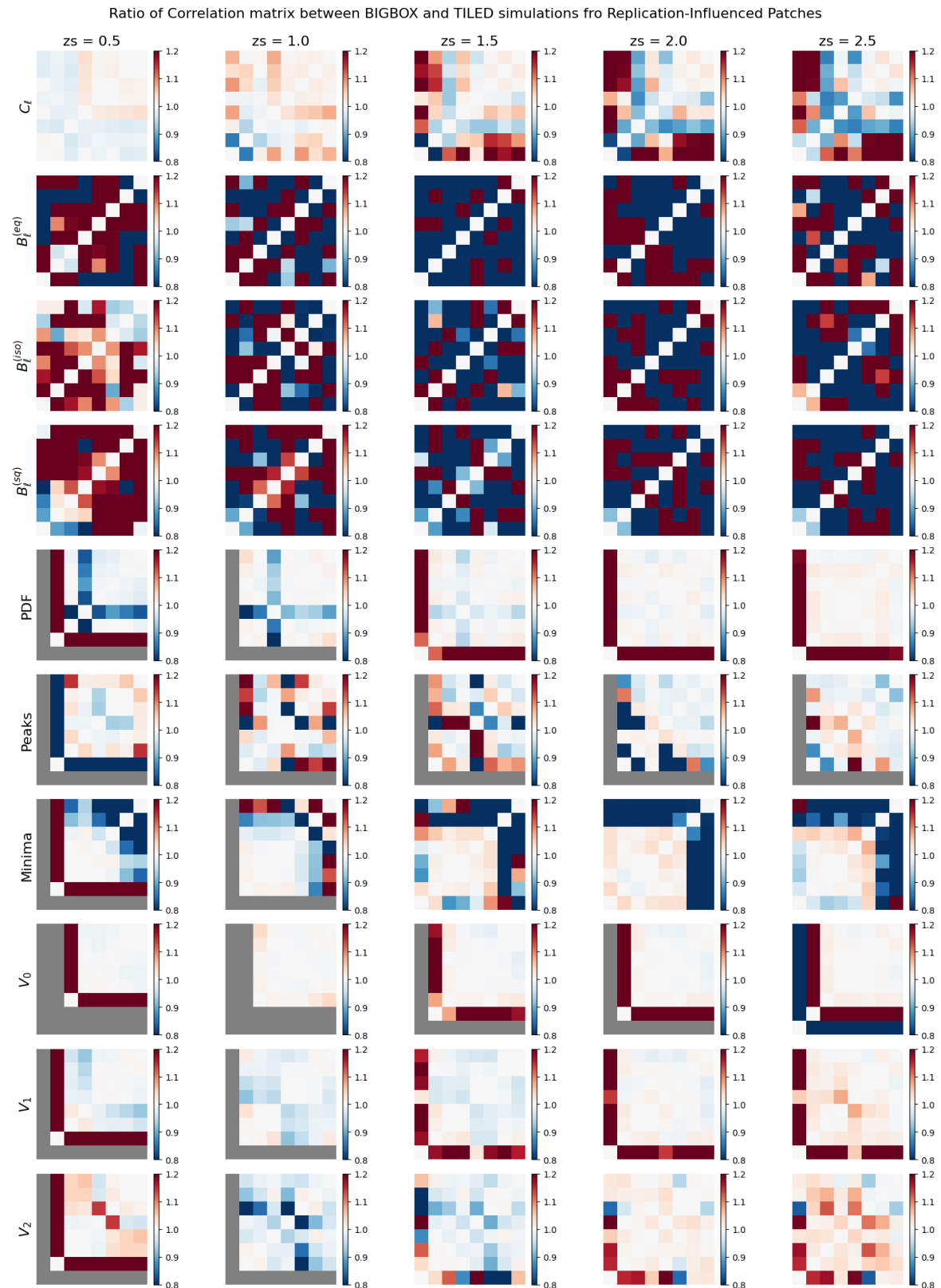


Figure 8.21: BIGBOX/TILED ratios of correlation matrices specifically for Replication-Influenced Patches (RIP). Similar to covariance ratios, RIP correlation ratios are consistently lower than those for RMPs. Off-diagonal structures differ from those in Figure 8.8 at lower redshifts but are likely to become more similar at higher redshifts.

Chapter 9

Conclusions

In this study, we performed a comprehensive analysis of weak lensing statistical measures using two simulation sets, BIGBOX and TILED, to investigate the impacts of super-sample covariance, shape noise, smoothing scales, and box replication artifacts. Our findings provide critical insights into the robustness and limitations of these simulations for modeling higher-order statistics in weak gravitational lensing.

We utilized the BIGBOX and TILED simulations to capture different aspects of super-sample covariance. By extracting $10^\circ \times 10^\circ$ patches from full-sky convergence maps via a Fibonacci grid, we achieved uniform coverage with minimal overlap. Incorporating realistic shape noise, modeled with Gaussian random fields and reduced through Gaussian smoothing, enhanced the relevance of our analysis for current and upcoming weak lensing surveys.

A suite of higher-order statistics, including the angular power spectrum, bispectrum, probability distribution function (PDF), peak and minima counts, and Minkowski functionals, was employed to probe the non-Gaussian features of the convergence field. These measures were meticulously computed using established tools and custom implementations, ensuring alignment with theoretical models like `Halofit`, `BiHalofit`, and `hmpdf`. By analyzing a broad range of scales, from ℓ -binned statistics ($\ell \in [300, 3000]$) to ν -binned statistics ($-4 \leq \kappa/\sigma_\kappa \leq 4$), we provided a detailed characterization of the scale-dependent behavior of super-sample covariance.

Comparing covariance and correlation matrices from BIGBOX and TILED revealed that super-sample covariance significantly affects the variance of statistical measures, especially at high multipoles and redshifts. While mean values between the simulations were consistent within 1%, variance ratios showed notable differences due to the presence of large-scale modes in BIGBOX that are absent in TILED. This underscores the necessity of accounting for super-sample covariance in high-precision cosmological analyses.

Shape noise was found to amplify sensitivities in statistical measures, particularly in the angular power spectrum and peak/minima counts, with deviations increasing at higher noise levels (e.g., DES and HSC). Nevertheless, super-sample covariance remained the dominant effect, maintaining its in-

fluence over noise contributions. Correlation matrices exhibited minimal structural changes ($< 5\%$), demonstrating the robustness of the covariance framework against noise.

Varying Gaussian smoothing scales primarily altered small-scale features in convergence maps without significantly impacting the covariance and correlation matrices. The angular power spectrum and bispectrum remained unaffected by smoothing, while higher-order statistics showed only modest changes. These results support the use of smoothing in weak lensing analyses to suppress small-scale noise without compromising the overall covariance structure.

Box replication artifacts posed a systematic challenge, leading to the underestimation of mean angular power spectra and distortion of ν -binned statistics in Replication-Influenced Patches (RIP). Covariance and correlation ratios in RIPs were consistently lower than in Replication-Minimal Patches (RMPs), indicating unique covariance structures introduced by replication artifacts. Additionally, box replication obscured redshift dependence, masking super-sample variance effects. These findings highlight the importance of addressing box replication artifacts to avoid biases in simulation-based analyses.

Our results have significant implications for weak lensing studies in surveys such as DES, HSC, LSST, Euclid, and Roman. The prominence of super-sample covariance necessitates the inclusion of large-scale modes in simulations to ensure accurate variance modeling. The demonstrated robustness of covariance structures to shape noise and smoothing scales enhances confidence in their applicability across various observational conditions. However, mitigating systematic effects like box replication artifacts remains crucial to prevent biases in higher-order statistics interpretation.

Future research should focus on:

- Developing methods to mitigate box replication artifacts, especially in simulations utilizing replicated volumes.
- Extending the analysis to incorporate additional cosmological models and baryonic effects to enhance simulation realism.
- Integrating these insights into survey design and data analysis pipelines to improve the precision of cosmological parameter inference.

By advancing simulation techniques and observational strategies, weak lensing continues to be a powerful tool for probing the Universe's fundamental properties and constraining cosmological models with unprecedented accuracy.

Bibliography

- Abbott B. P., et al., 2016, [Phys. Rev. Lett.](#), **116**, 061102
- Abbott T. M. C., et al., 2018, [ApJS](#), **239**, 18
- Abbott T. M. C., et al., 2021, [ApJS](#), **255**, 20
- Abbott T. M. C., et al., 2022, [Phys. Rev. D](#), **105**, 023520
- Aihara H., et al., 2018, [PASJ](#), **70**, S4
- Albrecht A., et al., 2006, [arXiv e-prints](#), pp astro-ph/0609591
- Alpher R. A., Herman R., 1948, [Nature](#), **162**, 774
- Amon A., et al., 2022, [Phys. Rev. D](#), **105**, 023514
- Armijo J., Marques G. A., Novaes C. P., Thiele L., Cowell J. A., Grandón D., Shirasaki M., Liu J., 2024, [arXiv e-prints](#), p. arXiv:2410.00401
- Asgari M., et al., 2021, [A&A](#), **645**, A104
- Bardeen J. M., Bond J. R., Kaiser N., Szalay A. S., 1986, [ApJ](#), **304**, 15
- Barnes J., Hut P., 1986, [Nature](#), **324**, 446
- Barreira A., Schmidt F., 2017, [J. Cosmology Astropart. Phys.](#), **2017**, 051
- Barreira A., Krause E., Schmidt F., 2018, [J. Cosmology Astropart. Phys.](#), **2018**, 015
- Bartelmann M., 2010, [Classical and Quantum Gravity](#), **27**, 233001
- Bartelmann M., Schneider P., 2001, [Phys. Rep.](#), **340**, 291
- Bayer A. E., Liu J., Terasawa R., Barreira A., Zhong Y., Feng Y., 2023, [Phys. Rev. D](#), **108**, 043521
- Bayer A. E., Zhong Y., Li Z., DeRose J., Feng Y., Liu J., 2024, [arXiv e-prints](#), p. arXiv:2407.17462
- Bennett C. L., et al., 2003, [ApJS](#), **148**, 97

- Berger M. J., Colella P., 1989, [Journal of Computational Physics](#), **82**, 64
- Bernardeau F., Colombi S., Gaztañaga E., Scoccimarro R., 2002, [Phys. Rep.](#), **367**, 1
- Bernstein G. M., 2010, [MNRAS](#), **406**, 2793
- Blas D., Lesgourgues J., Tram T., 2011, [J. Cosmology Astropart. Phys.](#), **2011**, 034
- Bond J. R., Efstathiou G., 1987, [MNRAS](#), **226**, 655
- Born M., 1926, [Zeitschrift fur Physik](#), **38**, 803
- Boyle A., Uhlemann C., Friedrich O., Barthelemy A., Codis S., Bernardeau F., Giocoli C., Baldi M., 2021, [MNRAS](#), **505**, 2886
- Carroll S. M., Press W. H., Turner E. L., 1992, [ARA&A](#), **30**, 499
- Chan K. C., Moradinezhad Dizgah A., Noreña J., 2018, [Phys. Rev. D](#), **97**, 043532
- Chen Z., Yu Y., 2024, [MNRAS](#), **534**, 1205
- Chisari N. E., et al., 2018, [MNRAS](#), **480**, 3962
- Cooley J. W., Tukey J. W., 1965, [Mathematics of Computation](#), **19**, 297
- Cooray A., Hu W., 2002, [ApJ](#), **574**, 19
- Couchman H. M. P., 1991, [ApJ](#), **368**, L23
- Couchman H. M. P., Thomas P. A., Pearce F. R., 1995, [ApJ](#), **452**, 797
- Crain R. A., et al., 2015, [MNRAS](#), **450**, 1937
- Crocce M., Castander F. J., Gaztañaga E., Fosalba P., Carretero J., 2015, [MNRAS](#), **453**, 1513
- DESI Collaboration et al., 2016, [arXiv e-prints](#), p. arXiv:1611.00036
- Dalal R., et al., 2023, [Phys. Rev. D](#), **108**, 123519
- Das S., Bode P., 2008, [ApJ](#), **682**, 1
- Dawson K. S., et al., 2013, [AJ](#), **145**, 10
- DeRose J., et al., 2019, [ApJ](#), **875**, 69
- Di Valentino E., et al., 2021, [Classical and Quantum Gravity](#), **38**, 153001
- Dietrich J. P., Hartlap J., 2010, [MNRAS](#), **402**, 1049
- Dodelson S., 2003, [Modern Cosmology](#)

- Dodelson S., Zhang P., 2005, [Phys. Rev. D](#), **72**, 083001
- Dodelson S., Kolb E. W., Matarrese S., Riotto A., Zhang P., 2005, [Phys. Rev. D](#), **72**, 103004
- Doux C., et al., 2022, [MNRAS](#), **515**, 1942
- Dubinski J., 1996, [New Astronomy](#), **1**, 133
- Efstathiou G., Davis M., White S. D. M., Frenk C. S., 1985, [ApJS](#), **57**, 241
- Einasto J., 1965, Trudy Astrofizicheskogo Instituta Alma-Ata, **5**, 87
- Einstein A., 1915, Sitzungsberichte der Königlich Preussischen Akademie der Wissenschaften, pp 844–847
- Eisenstein D. J., et al., 2005, [ApJ](#), **633**, 560
- Euclid Collaboration et al., 2019, [A&A](#), **627**, A59
- Euclid Collaboration et al., 2023, [A&A](#), **675**, A120
- Euclid Collaboration et al., 2024, [arXiv e-prints](#), p. arXiv:2405.13495
- Fabbian G., Lewis A., Beck D., 2019, [J. Cosmology Astropart. Phys.](#), **2019**, 057
- Falco E. E., Gorenstein M. V., Shapiro I. I., 1985, [ApJ](#), **289**, L1
- Feldman H. A., Kaiser N., Peacock J. A., 1994, [ApJ](#), **426**, 23
- Feng Y., Chu M.-Y., Seljak U., McDonald P., 2016, [MNRAS](#), **463**, 2273
- Ferlito F., et al., 2023, [MNRAS](#), **524**, 5591
- Flaugher B., et al., 2015, [AJ](#), **150**, 150
- Fluri J., Kacprzak T., Sgier R., Refregier A., Amara A., 2018, [J. Cosmology Astropart. Phys.](#), **2018**, 051
- Fluri J., Kacprzak T., Lucchi A., Refregier A., Amara A., Hofmann T., Schneider A., 2019, [Phys. Rev. D](#), **100**, 063514
- Fluri J., Kacprzak T., Lucchi A., Schneider A., Refregier A., Hofmann T., 2022, [Phys. Rev. D](#), **105**, 083518
- Fosalba P., Gaztañaga E., Castander F. J., Manera M., 2008, [MNRAS](#), **391**, 435
- Fosalba P., Gaztañaga E., Castander F. J., Crocce M., 2015a, [MNRAS](#), **447**, 1319

- Fosalba P., Crocce M., Gaztañaga E., Castander F. J., 2015b, [MNRAS](#), **448**, 2987
- Freedman W. L., et al., 2001, [ApJ](#), **553**, 47
- Friedmann A., 1922, [Zeitschrift fur Physik](#), **10**, 377
- Fu L., et al., 2014, [MNRAS](#), **441**, 2725
- Gamow G., 1948, [Nature](#), **162**, 680
- García-García C., Ruiz-Zapatero J., Alonso D., Bellini E., Ferreira P. G., Mueller E.-M., Nicola A., Ruiz-Lapuente P., 2021, [J. Cosmology Astropart. Phys.](#), **2021**, 030
- Gatti M., et al., 2020, [MNRAS](#), **498**, 4060
- Grewal N., Zuntz J., Tröster T., Amon A., 2022, [The Open Journal of Astrophysics](#), **5**, 13
- Gunn J. E., Gott J. Richard I., 1972, [ApJ](#), **176**, 1
- Guth A. H., 1981, [Phys. Rev. D](#), **23**, 347
- Górski K. M., Hivon E., Banday A. J., Wandelt B. D., Hansen F. K., Reinecke M., Bartelmann M., 2005, [The Astrophysical Journal](#), **622**, 759
- Hernquist L., Katz N., 1989, [ApJS](#), **70**, 419
- Hikage C., et al., 2019, [PASJ](#), **71**, 43
- Hilbert S., Hartlap J., White S. D. M., Schneider P., 2009, [A&A](#), **499**, 31
- Hockney R. W., Eastwood J. W., 1981, Computer Simulation Using Particles. CRC Press
- Hogg D. W., 1999, [arXiv e-prints](#), pp astro-ph/9905116
- Hubble E. P., 1925, [The Observatory](#), **48**, 139
- Hubble E. P., 1929, [ApJ](#), **69**, 103
- Ivezić Ž., et al., 2019, [ApJ](#), **873**, 111
- Jain B., Van Waerbeke L., 2000, [ApJ](#), **530**, L1
- Jeans J. H., 1902, [Philosophical Transactions of the Royal Society of London Series A](#), **199**, 1
- Joachimi B., et al., 2015, [Space Sci. Rev.](#), **193**, 1
- Kacprzak T., et al., 2016, [MNRAS](#), **463**, 3653
- Kaiser N., 2000, [ApJ](#), **537**, 555

- Kaiser N., Squires G., 1993, *ApJ*, **404**, 441
- Kiessling A., et al., 2015, *Space Sci. Rev.*, **193**, 67
- Kilbinger M., 2015, *Reports on Progress in Physics*, **78**, 086901
- Kilbinger M., Schneider P., 2005, *A&A*, **442**, 69
- Kirk D., et al., 2015, *Space Sci. Rev.*, **193**, 139
- Kollmeier J., et al., 2019, in *Bulletin of the American Astronomical Society*. p. 274
- Kratochvil J. M., Lim E. A., Wang S., Haiman Z., May M., Huffenberger K., 2012, *Phys. Rev. D*, **85**, 103513
- LSST Dark Energy Science Collaboration 2012, *arXiv e-prints*, p. arXiv:1211.0310
- LSST Science Collaboration et al., 2009, *arXiv e-prints*, p. arXiv:0912.0201
- Lacasa F., Grain J., 2019, *A&A*, **624**, A61
- Lacasa F., Rosenfeld R., 2016, *J. Cosmology Astropart. Phys.*, **2016**, 005
- Lacasa F., Lima M., Aguena M., 2018, *A&A*, **611**, A83
- Leclercq F., 2020, Evolution of cosmological simulations over the last 50 years, <http://florent-leclercq.eu/blog.php?page=2>
- Lemaître G., 1931, *MNRAS*, **91**, 483
- Lewis A., Challinor A., Lasenby A., 2000, *ApJ*, **538**, 473
- Li Y., Hu W., Takada M., 2014, *Phys. Rev. D*, **89**, 083519
- Li X., et al., 2023, *Phys. Rev. D*, **108**, 123518
- Limber D. N., 1954, *ApJ*, **119**, 655
- Linde A. D., 1982, *Physics Letters B*, **108**, 389
- Linke L., Heydenreich S., Burger P. A., Schneider P., 2023, *A&A*, **672**, A185
- Liu J., Bird S., Zorrilla Matilla J. M., Hill J. C., Haiman Z., Madhavacheril M. S., Petri A., Spergel D. N., 2018, *J. Cosmology Astropart. Phys.*, **2018**, 049
- Loureiro A., et al., 2022, *A&A*, **665**, A56
- Mandelbaum R., 2018, *ARA&A*, **56**, 393

- Mandelbaum R., Slosar A., Baldauf T., Seljak U., Hirata C. M., Nakajima R., Reyes R., Smith R. E., 2013, [MNRAS](#), **432**, 1544
- Mandelbaum R., et al., 2018a, [PASJ](#), **70**, S25
- Mandelbaum R., et al., 2018b, [MNRAS](#), **481**, 3170
- Marques G. A., Liu J., Zorrilla Matilla J. M., Haiman Z., Bernui A., Novaes C. P., 2019, [J. Cosmology Astropart. Phys.](#), **2019**, 019
- Marques G. A., et al., 2024, [MNRAS](#), **528**, 4513
- Martinet N., et al., 2018, [MNRAS](#), **474**, 712
- Matsubara T., 2010, [Phys. Rev. D](#), **81**, 083505
- Maturi M., Angrick C., Pace F., Bartelmann M., 2010, [A&A](#), **519**, A23
- Mead A. J., Heymans C., Lombriser L., Peacock J. A., Steele O. I., Winther H. A., 2016, [MNRAS](#), **459**, 1468
- Mecke K. R., Buchert T., Wagner H., 1994, [A&A](#), **288**, 697
- Miyazaki S., et al., 2018, [PASJ](#), **70**, S1
- Mo H. J., White S. D. M., 1996, [MNRAS](#), **282**, 347
- Navarro J. F., Frenk C. S., White S. D. M., 1996, [ApJ](#), **462**, 563
- Navarro J. F., Frenk C. S., White S. D. M., 1997, [ApJ](#), **490**, 493
- Nelson D., et al., 2019, [Computational Astrophysics and Cosmology](#), **6**, 2
- Oguri M., Hamana T., 2011, [MNRAS](#), **414**, 1851
- Omori Y., 2024, [MNRAS](#), **530**, 5030
- Panamarev T., Just A., Spurzem R., Berczik P., Wang L., Arca Sedda M., 2019, [MNRAS](#), **484**, 3279
- Peebles P. J. E., 1968, [ApJ](#), **153**, 1
- Peebles P. J. E., Yu J. T., 1970, [ApJ](#), **162**, 815
- Penzias A. A., Wilson R. W., 1965, [ApJ](#), **142**, 419
- Perlmutter S., et al., 1999, [ApJ](#), **517**, 565
- Petri A., 2016, [Astronomy and Computing](#), **17**, 73

- Petri A., Liu J., Haiman Z., May M., Hui L., Kratochvil J. M., 2015, [Phys. Rev. D](#), **91**, 103511
- Petri A., Haiman Z., May M., 2016, [Phys. Rev. D](#), **93**, 063524
- Petri A., Haiman Z., May M., 2017, [Phys. Rev. D](#), **95**, 123503
- Planck Collaboration et al., 2014, [A&A](#), **571**, A15
- Planck Collaboration et al., 2016, [A&A](#), **594**, A13
- Planck Collaboration et al., 2020, [A&A](#), **641**, A6
- Powell J., Caudill L., Young O., 2023, [American Journal of Physics](#), **91**, 478
- Press W. H., Schechter P., 1974, [ApJ](#), **187**, 425
- Rao C. R., 1952, Advanced Statistical Methods in Biometric Research. John Wiley & Sons, Inc., New York, N.Y.
- Refregier A., Amara A., Kitching T. D., Rassat A., Scaramella R., Weller J., 2010, [arXiv e-prints](#), p. [arXiv:1001.0061](#)
- Refregier A., Kacprzak T., Amara A., Bridle S., Rowe B., 2012, [MNRAS](#), **425**, 1951
- Riess A. G., et al., 1998, [AJ](#), **116**, 1009
- Riess A. G., Casertano S., Yuan W., Macri L. M., Scolnic D., 2019, [ApJ](#), **876**, 85
- Riess A. G., et al., 2022, [ApJ](#), **934**, L7
- Rubin V. C., Ford W. Kent J., 1970, [ApJ](#), **159**, 379
- Rubin V. C., Ford W. K. J., Thonnard N., 1980, [ApJ](#), **238**, 471
- Schaye J., et al., 2015, [MNRAS](#), **446**, 521
- Schmalzing J., Buchert T., 1997, [ApJ](#), **482**, L1
- Schmalzing J., Kerscher M., Buchert T., 1996, in Bonometto S., Primack J. R., Provenzale A., eds, Dark Matter in the Universe. p. 281 ([arXiv:astro-ph/9508154](#)), doi:[10.48550/arXiv.astro-ph/9508154](#)
- Schneider P., 2006, in Meylan G., Jetzer P., North P., Schneider P., Kochanek C. S., Wambsganss J., eds, Saas-Fee Advanced Course 33: Gravitational Lensing: Strong, Weak and Micro. pp 269–451
- Schneider P., Seitz C., 1995, [A&A](#), **294**, 411
- Schneider P., Ehlers J., Falco E. E., 1992, Gravitational Lenses, doi:[10.1007/978-3-662-03758-4](#).

- Scoccimarro R., Couchman H. M. P., Frieman J. A., 1999, [ApJ](#), **517**, 531
- Secco L. F., et al., 2022, [Phys. Rev. D](#), **105**, 023515
- Sehgal N., Bode P., Das S., Hernandez-Monteagudo C., Huffenberger K., Lin Y.-T., Ostriker J. P., Trac H., 2010, [ApJ](#), **709**, 920
- Seljak U. c. v., 2009, [Phys. Rev. Lett.](#), **102**, 021302
- Sheldon E. S., Becker M. R., MacCrann N., Jarvis M., 2020, [ApJ](#), **902**, 138
- Sheth R. K., Tormen G., 1999, [MNRAS](#), **308**, 119
- Sheth R. K., Mo H. J., Tormen G., 2001, [MNRAS](#), **323**, 1
- Shirasaki M., Hamana T., Yoshida N., 2015, [MNRAS](#), **453**, 3043
- Shirasaki M., Hamana T., Takada M., Takahashi R., Miyatake H., 2019, [MNRAS](#), **486**, 52
- Smith R. E., et al., 2003, [MNRAS](#), **341**, 1311
- Smoot G. F., et al., 1992, [ApJ](#), **396**, L1
- Spergel D., et al., 2015, [arXiv e-prints](#), p. arXiv:1503.03757
- Springel V., 2005, [MNRAS](#), **364**, 1105
- Springel V., et al., 2005, [Nature](#), **435**, 629
- Springel V., et al., 2018, [MNRAS](#), **475**, 676
- Stein G., Alvarez M. A., Bond J. R., van Engelen A., Battaglia N., 2020, [J. Cosmology Astropart. Phys.](#), **2020**, 012
- Sunyaev R. A., Zeldovich Y. B., 1970, [Ap&SS](#), **7**, 3
- Swinbank R., James Purser R., 2006, [Quarterly Journal of the Royal Meteorological Society](#), **132**, 1769
- Takada M., Hu W., 2013, [Phys. Rev. D](#), **87**, 123504
- Takada M., Jain B., 2004, [MNRAS](#), **348**, 897
- Takahashi R., Sato M., Nishimichi T., Taruya A., Oguri M., 2012, [ApJ](#), **761**, 152
- Takahashi R., Hamana T., Shirasaki M., Namikawa T., Nishimichi T., Osato K., Shiroyama K., 2017, [ApJ](#), **850**, 24

Takahashi R., Nishimichi T., Namikawa T., Taruya A., Kayo I., Osato K., Kobayashi Y., Shirasaki M., 2020, [ApJ, 895, 113](#)

Tamura N., et al., 2016, in Evans C. J., Simard L., Takami H., eds, Society of Photo-Optical Instrumentation Engineers (SPIE) Conference Series Vol. 9908, Ground-based and Airborne Instrumentation for Astronomy VI. p. 99081M ([arXiv:1608.01075](#)), doi:10.1117/12.2232103

Tegmark M., 1997, [Phys. Rev. Lett., 79, 3806](#)

Teyssier R., 2002, [A&A, 385, 337](#)

Teyssier R., et al., 2009, [A&A, 497, 335](#)

The Dark Energy Survey Collaboration 2005, [arXiv e-prints, pp astro-ph/0510346](#)

The EAGLE team 2017, [arXiv e-prints, p. arXiv:1706.09899](#)

Thiele L., Hill J. C., Smith K. M., 2020, [Phys. Rev. D, 102, 123545](#)

Thiele L., Marques G. A., Liu J., Shirasaki M., 2023, [arXiv e-prints, p. arXiv:2304.05928](#)

Trebitsch M., et al., 2021, [A&A, 653, A154](#)

Uhlemann C., Friedrich O., Boyle A., Gough A., Barthelemy A., Bernardeau F., Codis S., 2023, [The Open Journal of Astrophysics, 6, 1](#)

Valageas P., Nishimichi T., 2011, [A&A, 532, A4](#)

Vogelsberger M., et al., 2014, [MNRAS, 444, 1518](#)

Wang L., Spurzem R., Aarseth S., Nitadori K., Berczik P., Kouwenhoven M. B. N., Naab T., 2015, [MNRAS, 450, 4070](#)

Weinberg S., 1972, Gravitation and Cosmology: Principles and Applications of the General Theory of Relativity

Weinberg S., 2008, Cosmology

Wick G. C., 1950, [Phys. Rev., 80, 268](#)

Wu H.-Y., Weinberg D. H., Salcedo A. N., Wibking B. D., Zu Y., 2019, [MNRAS, 490, 2606](#)

Zel'dovich Y. B., 1970, [A&A, 5, 84](#)

Zeldovich Y. B., Sunyaev R. A., 1969, [Ap&SS, 4, 301](#)

Zhang T., Rau M. M., Mandelbaum R., Li X., Moews B., 2023a, [MNRAS, 518, 709](#)

Zhang T., et al., 2023b, [MNRAS](#), **525**, 2441

Zonca A., Singer L., Lenz D., Reinecke M., Rosset C., Hivon E., Gorski K., 2019, [Journal of Open Source Software](#), **4**, 1298

Zürcher D., Fluri J., Sgier R., Kacprzak T., Refregier A., 2021, [J. Cosmology Astropart. Phys.](#), **2021**, 028

de Jong J. T. A., et al., 2013, [The Messenger](#), **154**, 44